2010

Characterization of the effects of the human head on communication with implanted antennas

Michael A. Pecoraro

CHARACTERIZATION OF THE EFFECTS OF THE HUMAN HEAD ON COMMUNICATION WITH IMPLANTED ANTENNAS

by

Michael A. Pecoraro

A Thesis Submitted in Partial Fulfillment of the

Requirements for the Degree of

MASTER OF SCIENCE

in

Electrical Engineering

Approved by:

Professor_____
(Dr. Jayanti Venkataraman – Advisor)

Professor_____
(Dr. Sohail Dianat – Advisor)

Professor_____
(Dr. Gill Tsouri – Advisor)

Professor_____
(Dr. Lynn Fuller – Committee Member)

Professor_____
(Dr. Sohail Dianat – Department Head)

DEPARTMENT OF ELECTRICAL AND MICROELECTRONIC ENGINEERING
KATE GLEASON COLLEGE OF ENGINEERING
ROCHESTER INSTITUTE OF TECHNOLOGY
ROCHESTER, NEW YORK

FEBRUARY 2010

Acknowledgement

This work could never have been completed without the help of others...
That being said, I would like to dedicate this to…

Dr. Venkataraman –
who has guided me through my entire career here at RIT
and whose only fault seems to be that she prefers
Roger Federer over Andy Roddick… which I can forgive

Dr. Dianat and Dr. Tsouri –
who are always ready to answer questions,
help me and tell me, honestly, what they think

Jim Stefano, Ken Synder, Patti Vicari, Florence Layton and the E&μE Department –
who helped me with everything from scheduling things, getting Post-it notes, printing, scanning,
fixing license problems, scheduling more things, booking rooms… on and on, ad infinitum

My Family – Mom, Dad, Megan, Joe and Steve –
who support me in everything I do,
and love me as much as I love them

My Friends – Zachary, Ben, Toni and Chad –
who kept me sane, listened to me rant,
made me laugh and so much more

To all of you,
Thank You

Thesis Release Permission

DEPARTMENT OF ELECTRICAL AND MICROELECTRONIC ENGINEERING

COLLEGE OF ENGINEERING

ROCHESTER INSTITUTE OF TECHNOLOGY

ROCHESTER, NEW YORK

FEBRURARY 2010

Title of Thesis:

CHARACTERIZATION OF THE EFFECTS OF THE HUMAN HEAD ON COMMUNICATION WITH IMPLANTED ANTENNAS

Signature _____ **Date**_____

ABSTRACT

Cranially implanted sensors and electrodes have been used in practice for several years; their applications range from the recording of neural signals for use in Brain-Computer Interfaces to help the disabled, to the treatment of diseases and conditions ranging from Parkinson's disease, multiple sclerosis, depression, etc. Current communication methods with implants, however, are lacking; they run the gamut from physical, percutaneous connections that increase the risk of infection, to wireless links that are slow and uncomfortable for patients.

The present work focuses on the characterization of the effects of the human head on communication with cranially implanted antennas for its eventual use in improving current communication methods. A realistic human head model with frequency dependent tissue characteristics is used to obtain a transfer function that describes the magnitude and phase of an electromagnetic wave as it propagates through the human head over both frequency and depth into the skull; this data is obtained for multiple energy entry angles. The technique used to obtain transfer function measurements consists of taking the ratio of the electric fields at the receiver and transmitter and is developed through analysis of ultra-wideband transmit/receive antenna systems; verification for this technique is provided.

After the transfer function data described above is obtained, we posit a communication model to approximate the transfer function magnitude. This approximation takes the form of a modified log-distance, log-frequency path loss model and fits the data quite well. The final approximation describes the path loss of an electromagnetic wave over both frequency and distance for all simulated orientations.

Lastly, simulations are presented for communication from a cranially implanted dipole antenna. The received power of an external antenna – whose position is varied in both distance

(from the head), as well as location (around the head) – is captured and plotted. We finally show that the transfer function that was obtained for all perpendicular communication through the head is able to, in most cases, correctly predict the results of these received power simulations.

TABLE OF CONTENTS

LIST OF FIGURES

LIST OF TABLES

1. Introduction

1.1 Electromagnetic Wave Propagation and the Human Body

The biological effects of microwave radiation have been of interest for many years. It is necessary, then, to have accurate data concerning the electrical properties of such biological tissue. Since the 1960s much work has been done to compile this data for many different types of tissue, both animal and human, over large frequency ranges [1]–[3], [5], [6], [8]–[12]. This type of data acquisition is known as dielectric spectroscopy.

Historically, several different methods have been used to perform dielectric spectroscopy. One method, used often in the burgeoning years of this research, was the use of sample terminated transmission lines [6] [8]. A rectangular waveguide, or equivalent transmission line, would be terminated with a sample of the tissue-under-test and a short circuit. Measurement of the reflection coefficient could then be used to obtain the permittivity and conductivity of the sample. This first method provides accurate measurements in the 100MHz to 1GHz region, but fails to obtain accurate values at higher frequencies.

A second method, the use of an open-ended coaxial probe, soon became popular because of its ability to make accurate measurements over a wide range of frequencies with little overhead in preparation of the sample [2] [3] [5] [10] [11]. The popularity of this method was helped, in part, by the development of more advanced and accurate network analyzers and impedance analyzers. The technique is based on the fact that an open-ended probe has a fringing capacitance and conductance that can be determined solely based on the geometry of the probe and can be measured by a network/impedance analyzer. It is then possible to obtain the complex permittivity of an unknown sample through comparison of the initial impedance of the coaxial

line itself and the impedance of the line when it is in contact with a sample of unknown electrical characteristics. This method has been used by many researchers to obtain data for biological tissues up to 100GHz. This method, however, is not without its drawbacks. The inherent inhomogeneity of tissue can provide different measured values depending on the placement of the probe on the tissue. Also, problems such as electrode polarization, which is the manifestation of charges that occur at the interface of the sample and the probe, can influence the results that are obtained at the higher ends of the frequency spectrum. There are measurement techniques, however, that can minimize the effect of this type of systematic error [4]. Improvements to this method of dielectric spectroscopy are even now being developed. The necessity for *in vivo* dielectric measurements yielded the design of a new probe in 2005. This probe was a hermetically sealed coaxial probe that was bio-compatible and able to withstand harsh sterilization procedures and is therefore able to be used in hospital environments for both *in vivo* and *ex vivo* measurements.

The best known compilation of complex permittivity data for biological tissues is contained in a three paper series from 1996 by Gabriel et al [1]–[3]. The open-ended coaxial probe technique was utilized to obtain the permittivity and conductivity of seventeen different human tissue types (blood, cortical bone, white matter, heart, liver, skin, etc.) over a frequency range of 10Hz to 100GHz. Gabriel et al., in this series, also summarizes and presents results from other papers for other tissues.

As would be expected of any material over such a wide range of frequency, material properties do not stay constant, but actually vary with the frequency of energy that is applied. This behavior is known as dispersion, and biological tissues actually exhibit multiple dispersion regions. These dispersion regions are well known and are linked with different frequency ranges

and relaxation mechanisms inherent in the cellular and molecular makeup of the tissue [1] [13]. The first region, the alpha dispersion region, occurs at low frequencies and is associated with counterion effects near membrane surfaces. The beta dispersion region, which is in the frequency range of hundreds of kilohertz, is due to the effects of macromolecules within the cellular membranes. The gamma dispersion region, in the gigahertz region, is mainly due to dipolar mechanisms of water, salt and proteins. These regions all work together to, as frequency increases, decrease the permittivity and increase the conductivity of any tissue in an uneven, step-like fashion which has been attempted to be described using two main types of mathematical models; the Debye model and the Cole-Cole model [4]. These models, which will be elaborated on later, use either single or multiple time constants that can be either relaxed or tightened to approximate the unique curves exhibited by each individual tissue. Several different methods have been used to determine the optimum values for the time constants including least squares analysis, approximation using MATLAB functions and even a brute force method, used by Gabriel et al., to obtain a "…good fit to the data rather than a unique solution based on a mathematical argument." [15] [7] [3]

Much of the data that has been collected to this day is being used in the simulation of medical devices that have been implanted in the human body. These simulations are investigating what effects the layers of frequency dependent materials (presented by tissue) have on the propagation of the electromagnetic waves inside and outside of the body. Thus far, research in this area has focused on antennas; either in their design or in their effects on the tissue around them (Specific Absorption Rate). Some efforts have also been applied to developing new techniques that will be able to obtain, *in vivo*, the complex permittivities of tissues that are deeper within the body – effectively characterizing and identifying those tissues.

The area of medical implant antenna design is a relatively new field and has seen an influx of research in the past ten years not only because of the usefulness of such devices, but because of the allocation of specific frequency bands for such devices. The main band of interest is the Medical Device Radiocommunications Service (also known as MedRadio). MedRadio is an ultra-low power, unlicensed, mobile radio service for transmitting data in support of diagnostic or therapeutic functions associated with implanted and body-worn medical devices. This frequency band, previously known as the Medical Implant Communications Service band (MICS), was established in 1999 by the FCC to overcome the limitations of the previous biotelemetry techniques. These techniques were dependent on magnetic coupling for data transfer. This meant that the external monitoring equipment would have to be very close to the patient, often making contact with the skin and the equipment could only provide low data rates. Comparatively, MedRadio allows for high-speed, reliable, short-range (up to 2m), wireless links with implants. These improvements look to improve patient quality of life, reduce the risk of infection, enhance patient comfort and expand freedom of movement for both the patient and medical personnel [16] [17]. The MedRadio band itself is the frequency range of 401-406MHz. Operation in this range has a bandwidth limitation of 300kHz and an effective isotropic radiated power (EIRP) of -16dBm or lower $(25\mu W)$ [17] [19]. The range of 401-406MHz was selected for several reasons, not least of which is that these frequencies have propagation characteristics conducive to the transmission of radio signals within the human body. This will allow for the constraints of power, size and antenna performance to be more easily met. In addition, this range is internationally accepted in such areas as Europe/the UK, Canada, New Zealand, Korea and Japan [18] [20].

Other frequency ranges also have the ability to transmit medical data. The WMTS (Wireless Medical Telemetry) band, established by the FCC in 2000, allows for the remote monitoring of a patient's health in the 608-614MHz, 1395-1400MHz and 1427-1432MHz ranges. Applications here include devices that measure vital signs (pulse, respiration rates), etc [21]. There are Industrial, Scientific and Medical bands that have also been used for medical communication, although these frequency bands are much more crowded with other possible uses. These so-called ISM bands are in the 900MHz and 2400MHz regions [22] [23]. Lastly, the FCC is, as of August 2009, debating whether or not to add more frequency allocations for new Medical Micro-Power networks. MMNs are currently defined as a network of multiple (from 1 to 100) micro-medical implants connected by an external controller that can be used as sensors to provide information or can provide electrical stimulation to ease neurological conditions that cause pain and suffering – polio, multiple sclerosis, stroke or brain injury, for example. The proposed frequency ranges make up 24MHz of bandwidth over the multiple ranges of 413-419MHz, 426-432MHz, 438-444MHz and 451-457MHz [32].

Using the allocated frequency bands as a jumping off point, many researchers began designing antennas for medical implants, the most popular of which seems to be variations on Planar Inverted-F Antennas (PIFAs). Meandering dipole PIFAs have been designed for the use with cardiac pacemakers. These have package sizes of 32x40mm or 36x40mm and use superstrates to shield the antennas from the detuning effects of the body. Simulations have shown these antennas to obtain return losses of 17 to 22dB down, and return losses in a fluid that approximates the characteristics of human tissue, 5 to 8dB down. Both the far field radiation patterns of these antennas and their Specific Absorption Rates were examined as well [24].

Further work was done to modify the widths of the striplines to show improved radiation performance and reduced maximum SAR values [25].

More PIFA antennas were designed in both spiral and serpentine configurations. These antennas were also designed specifically for use with pacemakers and were simulated as such in simplified and detailed human body models. These antennas had many variables tuned including superstrate permittivity, substrate permittivity, stripline lengths, feed locations, ground point locations, superstrate heights, superstrate geometries, etc. Simulated results show good matches in the 400MHz range [26].

More antenna design has been done regarding stacking circular PIFA antennas to decrease antenna size, enhance bandwidth and reduce detuning effects of the body. Simulations show that return losses of greater than 30dB down can be achieved [27]. SAR studies, radiation patterns and efficiency have also been explored for this antenna type. Other antenna designs have been attempted as well. Simple wire antennas for use in pacemakers, encapsulated planar loop antennas at the 900MHz ISM band and also patch antennas [28]–[31]. Some patch antenna designs have used genetic algorithms to miniaturize the patches and obtain matches of anywhere from 18 to 35 dB down, and some patch antennas have been designed at higher frequencies (31.5GHz) to obtain an attractive form factor.

Other work with antennas has investigated the effects of body shape and body position on the radiation pattern. Gain differences have shown to vary as much as 10dB based on the age, sex, and arm position of the models [28], [32]–[34].

Further work can, and has been done to analyze the effects of the implanted antennas on the tissue that surrounds it. Specific Absorption Rate (SAR) is the power that is absorbed by surrounding tissue averaged over a certain volume. It has units of W/kg and the FCC has strict

regulations on SAR; for mobile phone certification the limit is 1 W/kg over 1g [28]. Several of the papers that presented antenna designs also evaluated the SAR levels of their respective antennas [24]–[26].

A final note on work that has been done in the area of electromagnetics and the human body is the work done on tissue characterization [14]. The major goal of this work is to use microwaves to detect cancer in the human body. It is known that tumors and healthy tissue have very different electrical properties [12] [37]. Much of this difference arises from the fact that tumors have a much higher water content that healthy tissue and thereby have increased loss. Research has been done in the area of antenna design and near-field image methods to effectively determine permittivity profiles of a possibly cancerous area [35]–[37].

1.2 Communication Issues and the Human Body

Turning to the research contributions in the field of communications and the human body, we find that four different channel models have been defined and work has been done to characterize several of those channels. These channels are defined by different scenarios of possible communication and are given by the IEEE 802.15.6 TG and are summarized below [38]:

Table 1: Possible Channel Types with Respect to Human Body Communication

Scenario	Description	Channel Model
S1	Implant to Implant	CM1
S2	Implant to Body Surface	CM2
S3	Implant to External	
S4	Body Surface to Body Surface (LOS)	CM3
S5	Body Surface to Body Surface (NLOS)	
S6	Body Surface to External (LOS)	CM4
S7	Body Surface to External (NLOS)	

* LOS ≡Line-of-Sight, NLOS ≡Non-Line-of-Sight,

The most well-researched of these channels is CM3, the on-body communication channel. This channel describes how electromagnetic waves attenuate and propagate around the surface of the human body. It has been found that the main mechanism for propagation on-body is through the phenomenon of creeping waves [39]. These are waves that display an exponential decay of power over distance. Papers have been written to characterize this channel over several of the medical frequency bands including the MedRadio band, the 900MHz ISM band, the 2.4GHz ISM band and even an ultra wide band from 3-6GHz [38]–[42]. Both simulated and experimental data have been obtained for this specific channel and the general consensus is that the usual communication models – simple indoor propagation, log-distance and log-frequency models –fit the data quite well [38] [41] [42]. Other models have been fit to the data including dual slope/multiple breakpoint models, doubly exponential loss models and exponential loss models with saturation points, but they all have the general indoor propagation model as their basis [40]. On top of fitting the data to log-distance formulas, some research has already begun on diversity measurements for on-body communication systems and other research has compared different distributions of the amplitude variation statistics of the data [41] [42].

The channel that most pertains to the work in this paper is the in-body channel, represented by CM2. At this time, there are only a few papers on this topic. Some work was done in 2003 to derive a path loss model based on the SAR losses in the near and far fields of the implanted antenna [43]. This model was a simplified model for a single human tissue that was assumed to have no sharp edges or rough surfaces and did not have frequency dependent electrical properties. Validation of this simplified model was done in simulation, using Ansoft HFSS, as well as experimentally, using probes placed in a saturated salt solution. Further research was done in 2006 to characterize the in-body channel [44]. Both simulated and

experimental results were obtained. The simulations used Conformal FDTD (Finite Difference Time Domain) techniques to simulate the power losses through the human torso at 402MHz, 868MHz and 2400MHz while the experimental results were obtained with a human phantom shell filled with animal organs. Results from the two methods were similar and the path loss model was fit to a normal indoor propagation model – a log-distance model. The most recent work, in 2007, generated experimental results from two insulated wire antennas placed inside a live pig that was placed under anesthesia and on a ventilator [45]. Again, the type of path loss model that was used to fit the data was a variation of the log-distance, log-frequency model.

1.3 Characterizing Communication with Implanted Antennas

Lastly, some research has been done to look at power levels created outside a simplified human head model [24]. The model of the head was composed of six concentric spheres, each representing a different biological tissue or material; namely, brain, cerebro spinal fluid, dura, bone, fat and skin. The communication link between two 402MHz matched half-wavelength dipoles – one inside the head and another outside the head – was then characterized by observing the power levels received by the external dipole after excitation of the inner dipole. These simulations were done at distances of 1-5m between the center of the head and the external dipole. The internal dipole was simulated at two locations, the center of the head and moved towards the external dipole 4.5cm. The power level results were given in dBm and were modified to assume that the transmitting antenna used only 1.84mW (such that the maximum EIRP requirement of $25\mu W$, as set by the FCC for medical implants, was met). With this simplified model it was found that receiver sensitivities of -55dBm would be necessary at maximum communication distances of 5m. It was interesting to note, as well, that moving the internal dipole away from the center of the head (4.5cm closer to the external antenna) actually

decreased the power that was received by the external dipole by approximately 3dB across all distances from 1 to 5 meters. This result, however, was not explained.

1.4 Major Contributions of Present Work

The work detailed in this paper includes the development and verification of an E-Field ratio technique to obtain transfer function measurements. The use of E-Field ratios and traditional power loss measurements are then used to obtain the transfer function data presented by the human head over a wide band. This data, which will be dependent on both distance and frequency, is recorded for multiple energy entry angles. We then present a new, more generalized version of the well known log-distance, log-frequency path loss models. Following this, there is the application of this generalized Indoor Propagation path loss model to the wideband transfer function data to describe the human head's magnitude transfer function characteristics. Next we look at narrowband receiver power level measurements obtained through simulation of dipole antennas that are placed inside and outside of a detailed human head model; it is such that the implant is used as the transmitter and is placed at multiple locations within the head. Again, measurements at each implant location are recorded for multiple external antenna angles. We then show that the estimated transfer function can be used to correctly predict the results of power level simulations.

From this work we define our major contributions as the following:

1) A realistic human head model with frequency dependent tissue characteristics is used to obtain a transfer function that describes the magnitude and phase of an electromagnetic wave as it propagates through the human head. This transfer function varies over both frequency, and depth into the skull.

2) The obtained transfer function data, captured over a wide frequency range, is then approximated through the use of a modified log-distance, log-frequency communication model for path loss.
3) The estimated transfer function is then used to successfully predict received power from simulations of cranially implanted antennas.

1.5 Organization of Present Work

This first chapter serves the purpose of informing the reader of the work that has been done up to this point in the areas of electromagnetics and communications with regard to the human body, as well as presenting the major contributions to this field as provided by this paper. Chapter 2 will provide further background information on topics and materials that were heavily used in this research. This includes more in-depth discussions of frequency dependent media, their properties and the models that describe them as well as descriptions of the human body model and software that was used to simulate these complex geometries/environments.

Chapter 3 will present the derivation and verification of a new E-Field ratio technique that is used to obtain the transfer function of a channel. This model is used to, for a single distance, obtain the transfer function magnitude and phase over all frequency. Theory will be presented as well as simulation descriptions and results for simple, known models.

Chapter 4 will present the application of the E-Field ratio technique on a detailed model of the human head. Simulations, as well as the necessary post-processing, will be described and the results obtained for all angles will be presented and discussed. As further verification of the E-field ratio model, and as confirmation that the simulations are correctly being implemented, results will also be shown for the more well-known method of obtaining the transfer function magnitude through the use of the Poynting vector. The use of Poynting vector method, however,

is not a replacement for the E-field method because it does not allow for the capture of phase data and is only able to provide results over all distance for a single frequency; the E-field method provides results over all frequency for a single distance.

Chapter 5 will then use the data obtained in Chapter 4 and fit communication type path loss models to it. Using minimum mean square error estimation techniques, a strategy is laid out to show the best possible fit is a variation on a known path loss model. This new model is also shown to be a generalization of the well known indoor propagation model.

Chapter 6 will present verification of previous work in the area of generating power profiles around simplified versions of a human head. That work will then be extended to use the human body model's detailed head. Further, the human body model's head will be used to investigate the angular dependence of the received power. Chatper 7, as a test of the reciprocity of the estimated transfer function model, the final equation that is obtained in Chapter 5 is used to predict the results of the power level simulations.

Finally, Chapter 8 will conclude this work by summing up the work done, reiterating the major contributions, describing further applications of this work and positing possible future work.

2. Background

2.1 Frequency Dependent Media

2.1.1 Electromagnetic Theory

All human tissues, by virtue of their water content, have non-zero conductivity, $\sigma \neq 0$. Furthermore, this tissue conductivity is not constant, i.e. it varies with frequency. As with any non-zero conductivity, this implies that the electrical permittivity of human tissue is inherently complex. This is shown in Equation 1, which shows the most general definition of the complex permittivity of a material.

$$\hat{\varepsilon}(f) = \varepsilon'(f) + j\varepsilon''(f) = \varepsilon(f) - j\frac{\sigma(f)}{\omega} \quad (1)$$

If we were to examine this further, we could consider an example of an x-polarized plane wave traveling in the +z-direction. In this situation, the following equations describe the E- and H-fields:

$$E_x = E_0 e^{-j\hat{k}(f)z} \quad (2)$$

$$H_y = H_0 e^{-j\hat{k}(f)z} \quad (3)$$

$$E_y = E_z = H_x = H_z = 0 \quad (4)$$

where

$$\hat{k} = \sqrt{\omega^2\mu\varepsilon(f) - j\omega\mu\sigma(f)} = \beta(f) - j\alpha(f) \quad (5)$$

Therefore we see that the total E- and H- fields can be rewritten as:

$$E_x = E_0 e^{-\alpha(f)z} e^{-j\beta(f)z} \quad (6)$$

$$H_y = H_0 e^{-\alpha(f)z} e^{-j\beta(f)z} \quad (7)$$

where $\alpha(f)$ and $\beta(f)$ are defined as

$$\alpha(f) = \frac{\omega\sqrt{\mu\varepsilon(f)}}{\sqrt{2}}\sqrt{\sqrt{1+\left(\frac{\sigma(f)}{\omega\varepsilon(f)}\right)^2}-1} \quad (8)$$

$$\beta(f) = \frac{\omega\sqrt{\mu\varepsilon(f)}}{\sqrt{2}}\sqrt{\sqrt{1+\left(\frac{\sigma(f)}{\omega\varepsilon(f)}\right)^2}+1} \quad (9)$$

In Equations 6 and 7, we see that the values of $\alpha(f)$ and $\beta(f)$ affect the fields differently. Any non-zero, positive value for $\alpha(f)$ will result in exponential decay of the E-field amplitude as distance increases. We also see that larger values of $\alpha(f)$ will correspond to faster attenuation. We can see now see why $\alpha(f)$, which is measured in units of nepers per meter, is known as the attenuation constant. $\beta(f)$, on the other hand, is contained in a *complex* exponential. The *j* term causes the exponential to engage in oscillatory behavior and, therefore, this exponential term can be seen to describe the phase progression of the wave as it moves in the +z-direction. $\beta(f)$ is therefore known as the propagation constant and is measured in radians per meter.

Further investigating the conditions for which attenuation occur, we set Equation 8 to be greater than zero. Solving this condition we see that any non-zero conductivity will cause exponential attenuation. Therefore, coupling this information with the fact that tissue has frequency dependent conductivity and epsilon values, we can safely say that any E- and H-fields travelling through the human body will experience complex and varied attenuations at different frequencies as it travels through each different type of tissue.

2.1.2 Complex Permittivity of Human Tissue

The next logical step is to answer the question: what does the complex permittivity profile of a specific type of tissue look like? As was described in the literature survey, this question has been addressed by many researchers over the past fifty years. The most comprehensive collection of data was contained presented/collected by Gabriel et. al. in a three paper series [1]–[3]. Several examples of permittivity profiles for tissues that are pertinent to this research are taken from Gabriel et. al. and replotted below.

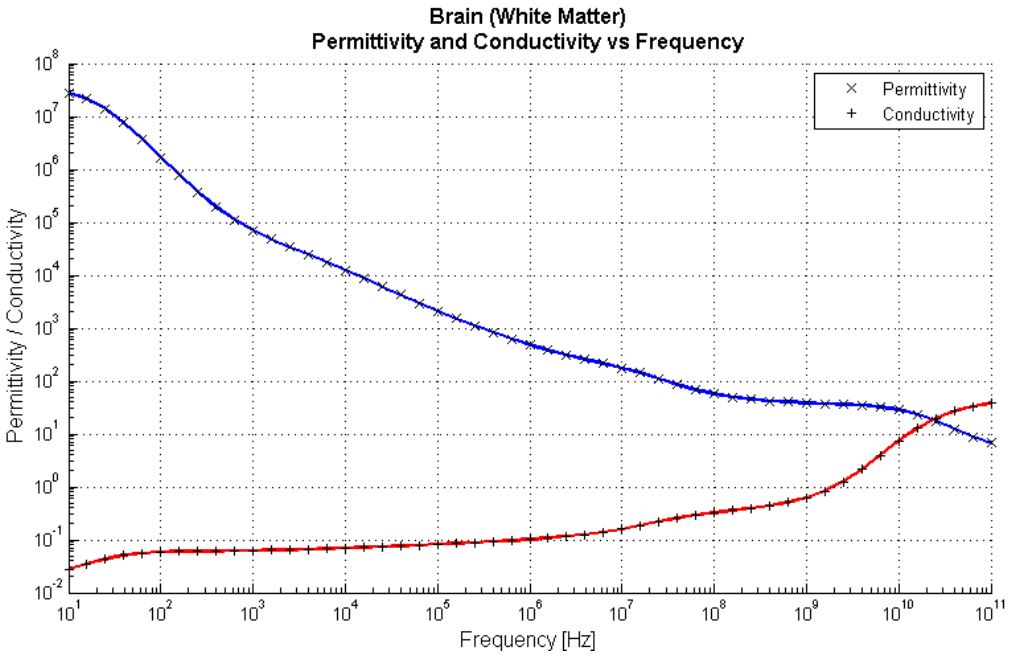

Figure 1: Permittivity and Conductivity of Brain (White Matter) vs. Frequency

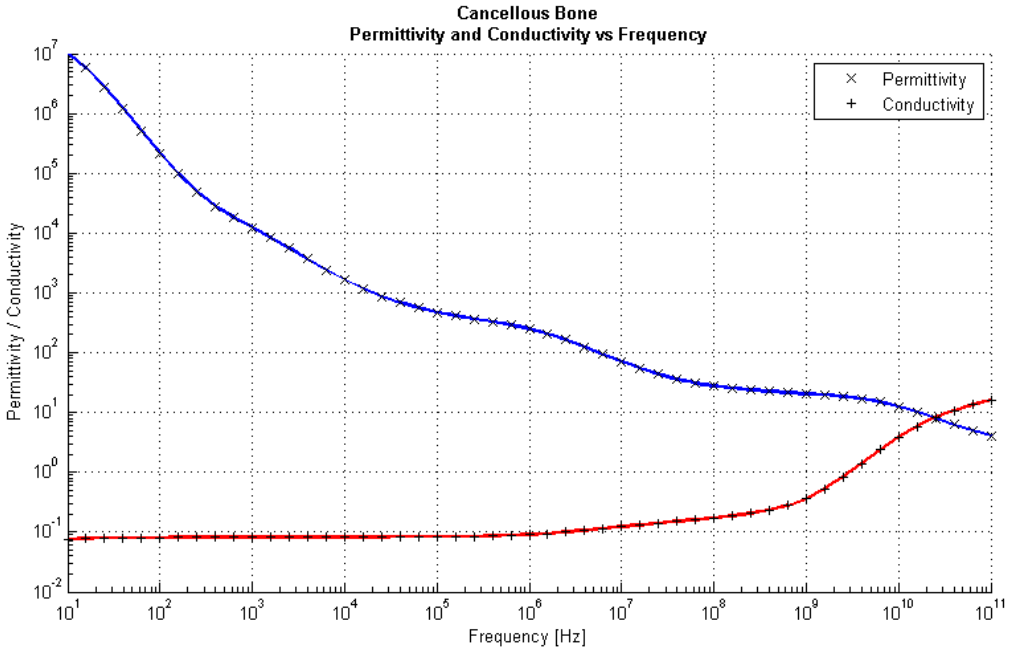

Figure 2: Permittivity and Conductivity of Bone (Cancellous) vs. Frequency

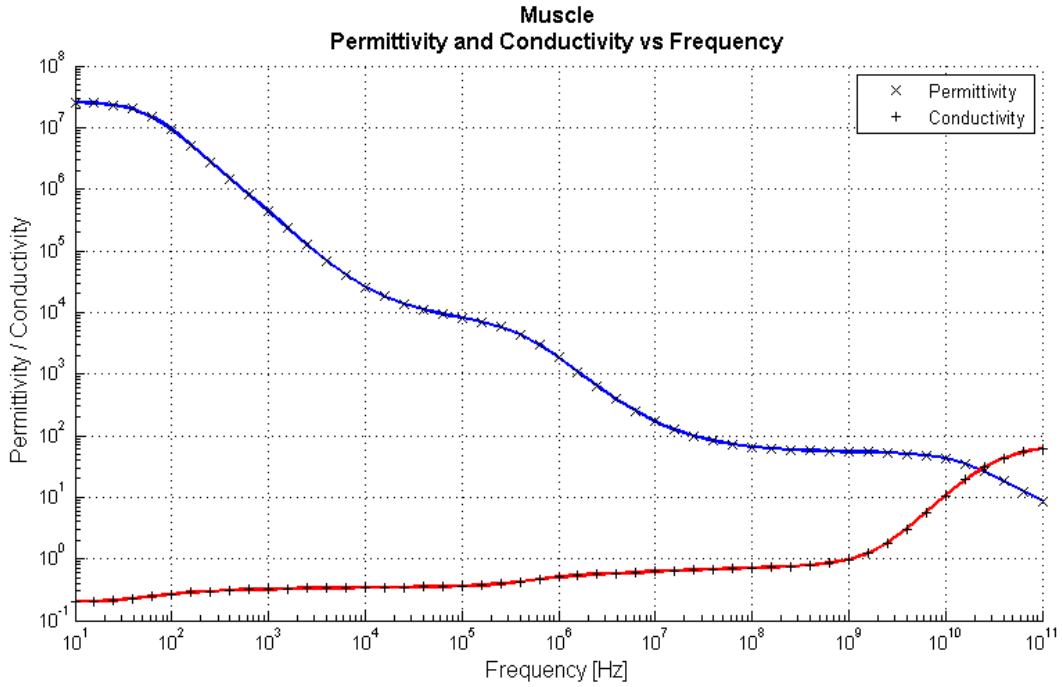

Figure 3: Permittivity and Conductivity of Muscle vs. Frequency

As one can see from *Figure 1*, *Figure 2* and *Figure 3*, the permittivity and conductivity varies greatly, not only as frequency changes, but as the tissues changes as well. In general, though, as frequency is increased there is a decrease in permittivity and an increase in conductivity. Clearly, operating at higher frequencies in the body will cause much higher losses as compared to using lower frequencies.

2.1.3 Debye and Cole-Cole Models for Complex Permittivity

The next step, now that the complex permittivity profiles have been obtained for different tissues, is to mathematically approximate them. There are two well known mathematical models that are used to describe these profiles, namely the Debye model and the Cole-Cole model. As was described in the literature survey, tissue is characterized by several different dispersion regions, each of which are linked to the expression of one or another polarization mechanism that is intrinsic to the chemical makeup of the tissue. In terms of the plots of complex permittivity, these polarization mechanisms are what cause the plateau/slope/plateau-type characteristics. This plot type is able to be characterized, in a first order approximation, through the use of a relaxation constant. This is seen in the Debye equation shown below:

$$\hat{\varepsilon}(\omega) = \varepsilon_{\infty} + \frac{\Delta\varepsilon}{1 + j\omega\tau} \qquad 10$$

where

$$\Delta\varepsilon = \varepsilon_s - \varepsilon_{\infty} \qquad 11$$

and describes the magnitude of the change in the permittivity. Further, ε_{∞} is defined as the permittivity at very high frequency, ε_s is defined as the 'static,' low frequency permittivity, and τ is the relaxation time constant [3] [46] [47]. This general form can be extended to form an nth-order approximation by using the multi-term Debye equation, seen below:

$$\hat{\varepsilon}(\omega) = \varepsilon_{\infty} + \sum_{n} \frac{\Delta\varepsilon_n}{1 + j\omega\tau_n} + \frac{\sigma_i}{j\omega\varepsilon_0} \qquad 12$$

This equation allows for multiple time constants and takes into account a constant σ_i term, which is the static ionic conductivity of the material.

The Debye model, however, has been slightly modified and improved through the use of a broadening factor α in the Cole-Cole model, seen below:

$$\hat{\varepsilon}(\omega) = \varepsilon_{\infty} + \frac{\Delta\varepsilon}{1 + (j\omega\tau)^{(1-\alpha)}} \qquad 13$$

By raising the time constant to the factor of $1 - \alpha$, the time constant becomes more malleable because its effect can be spread out over more or less of a frequency range. Similarly to the Debye model, multi-term Cole-Cole models can be utilized to better fit the models [3]. The mathematical model for a multi-term Cole-Cole approximation is shown below:

$$\hat{\varepsilon}(\omega) = \varepsilon_{\infty} + \sum_{n} \frac{\Delta\varepsilon_n}{1 + (j\omega\tau_n)^{(1-\alpha_n)}} + \frac{\sigma_i}{j\omega\varepsilon_0} \qquad 14$$

A fourth order Cole-Cole dispersion model was manually fit to each tissue for which Gabriel et. al. generated a permittivity profile. The data for all tissues fitted by Gabriel et. al. are available for free, online from the Italian National Research Council [48].

2.2 Human Body Model

All simulations performed for this research included the use of a highly accurate human body model. This model was provided by the Ansoft Corporation and has a resolution of 1mm. The body model, which was created for Ansoft by Aarkid, contains over three hundred objects including bones, muscles, organs, blood vessels, nerves, etc. Such a high accuracy, however, translates to longer simulation times. To avoid this problem, the model was cut as to only contain the head, neck and, in some cases, part of the shoulders. To decrease simulation time further, the

generated meshes were only at an accuracy of 2-4mm. The model itself is one of an adult male lying supine; a position that is often encountered during Magnetic Resonance Imaging (MRI). Some images of the model are shown below to get a sense of the detail of the model:

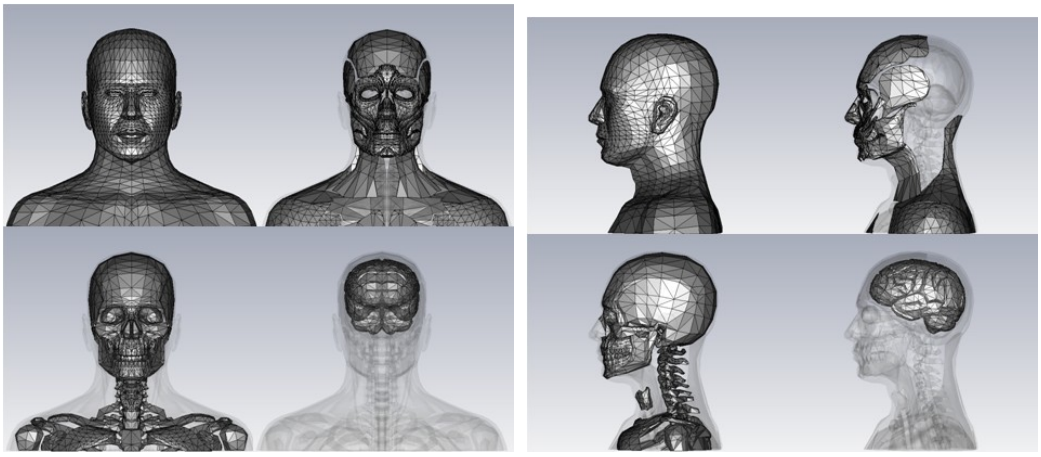

Figure 4: Images of the Human Body Model, Front and Side Views

There are two sets of four images; each set shows a different body orientation. Proceeding clockwise from the top left, the images highlight the body exterior, muscle, brain and cerebellum, and bone (cortical and cancellous).

All objects are assigned frequency dependent electrical parameters. The actual values for the parameters are provided by Gabriel et al. and others through the use of the Italian National Research Counsil's online database [48].

It should be noted that this model does not contain any explicit objects for fat or skin and, any part of the body that is not occupied by an organ, a muscle or a bone is assumed to have electrical properties in a range between water and fat. It is for this reason that the model assigns these objects/spaces with a permittivity value of 50 and a dielectric loss tangent value of 0.5.

It is also important to note that the electrical characteristics that are applied to the brain in this model is a combination of both white and grey matter. The body model denotes this tissue as human_brain_avg. Although both white and grey matter exist independently in the physical human brain, they are intermingled. Because no distinction is made in the body model provided by the Ansoft Corporation, the whole brain is characterized as having the properties of the average of white and grey matter.

2.3 Electromagnetic Software

All simulations for this research were done using CST Microwave Studio. CST MWS is an industry standard, three-dimensional, finite-difference time-domain tool that is specifically designed for the simulation of electromagnetic situations at high frequency. The use of the FDTD solver allows for quick simulation of wide frequency ranges as well as direct computation of the E- and H-fields, which makes it especially well suited for bio-medical simulations. Further descriptions of the software and of simulations will be presented as needed.

3. Development of E-Field Technique for Transfer Function

The end goal of this section is to develop some way to obtain data that describes the changes in magnitude and phase that occur to an electromagnetic wave as it propagates through the human head at any frequency between 300MHz and 3GHz. This data, once obtained, is useful for several reasons. First, it will be the first real glimpse at what type of a communication system is presented by layers of frequency dependant biological tissue - knowledge of a channel allows for optimization of communication through that channel, so this data will be essential to enhancing the performance of future data transfer through this channel. Also, this data can be used by other researchers as a design reference; specifically with respect to estimating the possible losses that their system may incur if it is to be used at a specific frequency and at a specific depth.

With that being said, one important point must be made explicit: to make use of either of these benefits, the transfer function data that is obtained *must not* include any assumptions about the type of antennas being used. This point, although seemingly obvious, is not trivial. Because this type of research is still in its infancy, there is no clear choice of antenna to use as an implant. If you were to create any sort of simulation that assumed a specific type of antenna, the effects of that antenna would have to be removed from the simulation results – otherwise the results are only valid for that specific antenna combination. Therefore any assumptions about the type of antenna used would render the results too specific. Even still, the goal is to obtain *wideband* transfer function data and the use of a physical antenna is intrinsically narrowband – a different antenna would then have to be designed and simulated for each frequency.

Problems actually arise from this quickly. Namely, how to obtain these results? Thus far, no method has been presented that makes clear exactly how to easily obtain wideband transfer

function data (both magnitude and phase) that does not include any sort of antenna effect. A summary of the current work is given below.

3.1 Previous Transfer Function Techniques

Some simulation work has been done using physical dipole antennas. These simulations use an implanted transmitter and an external receiver and then subsequent power levels are obtained at the varying receiver locations by manipulating the data obtained from calculating the three-dimensional Poynting vector field [24]. Clearly this data is, because it assumes the use of dipole antennas, only valid for a narrow frequency range – but one can further examine the technique used to obtain the data. When this is done we see that the results will not give us exactly what we are looking for. First, use of the Poynting vector field only allows the capture of magnitude data – phase data is lost. Another shortcoming is that the Poynting vector field is calculated over all space for a single frequency – this is the exact opposite of what we are looking for. We want all frequency at discrete distances. This method, however, can be used to double check the magnitude that is obtained by any other method that we eventually use to calculate the transfer function. This check is performed later in this very paper to show that our soon-to-be-developed E-field transfer function theory is correct and is correctly being evaluated.

The only other attempt to obtain transfer function data is found in a paper that acquired experimental results with a live pig [45]. In this paper a live pig was placed under anesthesia and was on a mechanical ventilator and S-parameter measurements were made using physical dipole antennas that were placed inside of the pig at a total of 48 different locations. An attempt was made, then, to use the measured S-parameters to get rid of the effect of the antennas and obtain the transfer function of the channel. This was done using the following equation:

$$H(f,d) = \frac{S_{21}}{(1-S_{11})(1-S_{22})} \qquad 15$$

Unfortunately, no derivation or reference is given for this equation – it is just used. Attempts at proving this equation theoretically have failed, as have attempts to contact the authors, and it does not correctly obtain the free space transfer function when two dipoles are simulated in the far field, in free space. Therefore, we have assumed this equation to be incorrect and we find that the only two attempts at obtaining transfer function data are inadequate for our needs, so a new method must be found. This method is obtained through analysis of well known ultra-wideband transmit-receive antenna systems.

3.2 E-Field Technique

Several papers have been written, recently, that describe the characterization of conventional UWB transmit-receive antenna systems. A model of this system can be seen below in *Figure 5*:

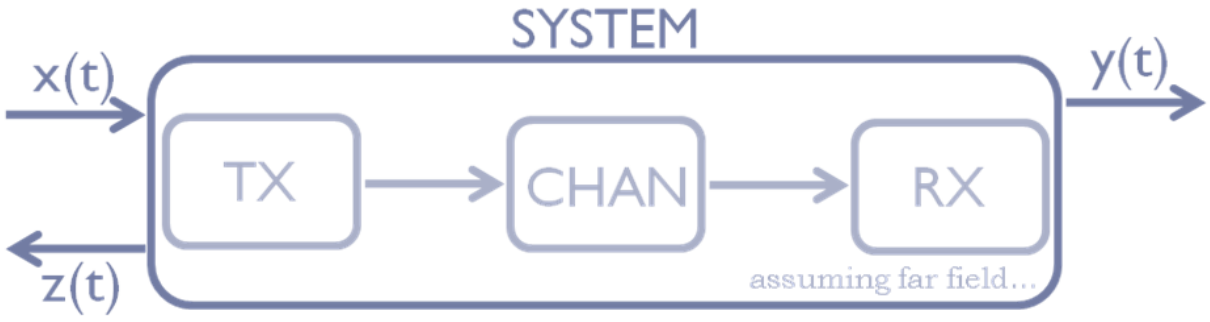

Figure 5: Conventional Ultra-wideband Transmit-Receive Antenna System

This model shows that if we assume that the transmit antennas is in the far field, then the system consists of three cascaded transfer functions; namely the transmit antenna (TX), the channel itself (CHAN), and the receive antenna (RX) [49]–[51]. In *Figure 5* we also see three time domain signals which can be defined as follows:

$x(t) \equiv time\ domain\ input\ voltage\ signal$

$y(t) \equiv time\ domain\ output\ voltage\ signal$

$z(t) \equiv time\ domain\ reflected\ voltage\ signal$

$z(t)$ would be due to not having a perfectly matched system. The frequency domain signals can be obtained by taking the Fourier transform of the time domain signals. These signals are $X(f)$, $Y(f)$ and $Z(f)$, respectively. To describe the transfer function of the total system, then, we have two equivalent statements. The first of these statements is just the cascading of the three transfer functions that make up the system. The second statement is really the definition of a transfer function: output over input. It just so happens that in electromagnetics, this is denoted by the S-parameter S_{21}.

$$H_{SYSTEM}(f) = H_{TX}(f) \cdot H_{CHAN}(f) \cdot H_{RX}(f) \qquad 16$$

$$= \frac{Y(f)}{X(f)} = S_{21}(f)$$

The final goal then, in terms of *Figure 5*, is to obtain just the channel portion of the total system, as seen below in *Figure 6*:

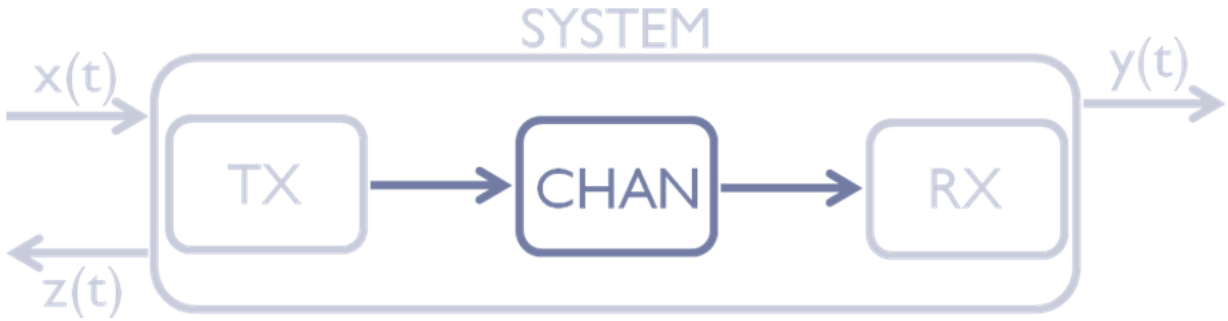

Figure 6: Transfer Function of the Channel, as a part of the Total System Transfer Function

To do this, instead of dealing with entire systems, we find in the literature that UWB systems are often split into two simpler systems. One system contains the transmit antenna and

the channel, while the other system contains the receive antenna [49]–[51]. These sub-systems can be visualized as seen below in *Figure 7* and *Figure 8*:

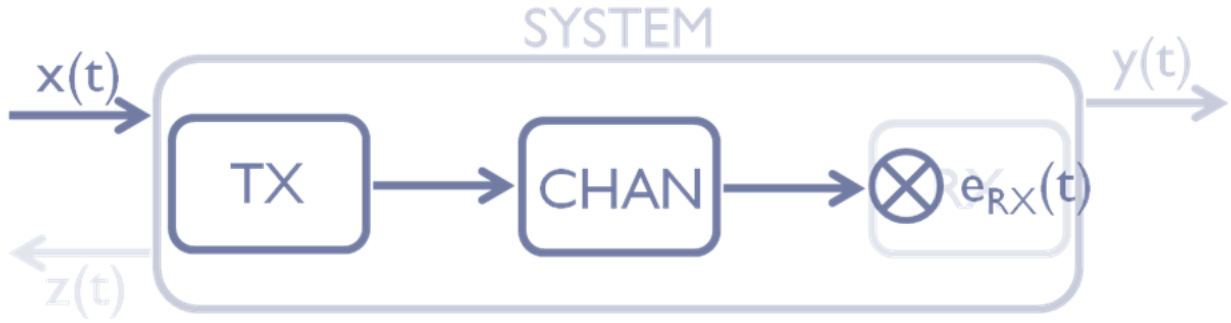

Figure 7: UWB Sub-System 1: Transmit Antenna and Channel

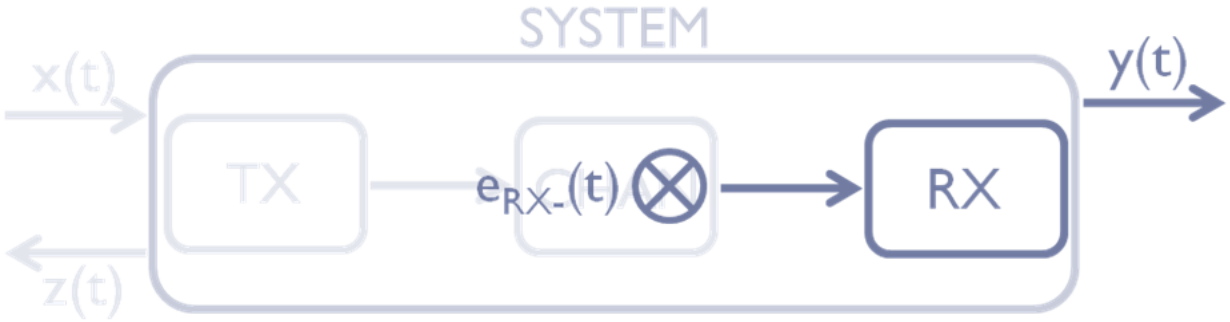

Figure 8: UWB Sub-System 2: Receive Antenna

where $e_{RX}(t)$ represents the time domain electric field at the location of the receive antenna and $e_{RX-}(t)$ represents the time domain electric field at a location just before the receive antenna. Taking the Fourier transform of these signals yield the terms $E_{RX}(f)$ and $E_{RX-}(f)$, respectively. The transfer functions of these two sub-systems can then be calculated similar to the ways that the total system was characterized, namely by placing the frequency domain output over the frequency domain input:

$$H_{TX/CHAN}(f) = H_{TX}(f) \cdot H_{CHAN}(f) \qquad 17$$

$$= \frac{E_{RX}(f)}{X(f)}$$

$$H_{RX}(f) = \frac{Y(f)}{E_{RX-}(f)} \qquad 18$$

We see, then, that we are able to define the transfer functions of both a single antenna *and* a single antenna and the channel. Looking at Equations 17 and 18 we see that we are very close to obtaining the channel. We see that $H_{CHAN}(f) = \frac{H_{TX/CHAN}(f)}{H_{TX}(f)}$, but we do not yet have $H_{TX}(f)$; instead we have $H_{RX}(f)$. All we need to do now, then, is characterize the receive antenna as if it were the transmit antenna:

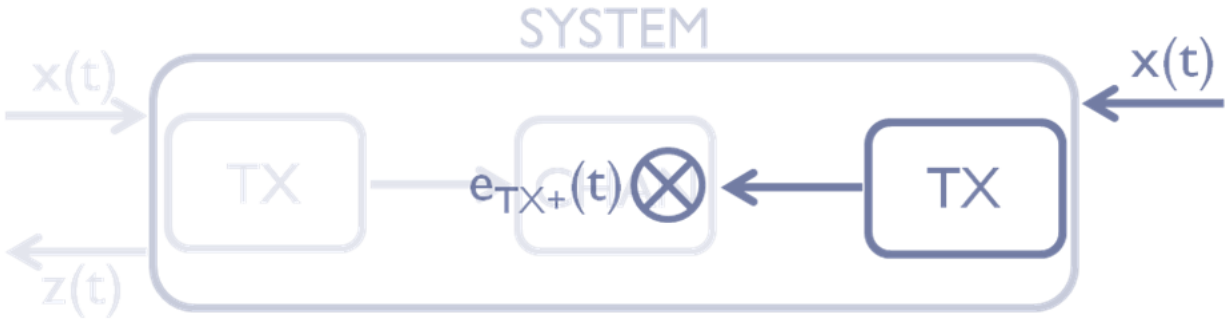

Figure 9: UWB Sub-System 2, Reversed: Transmit Antenna

we find, then:

$$H_{TX}(f) = \frac{E_{TX+}(f)}{X(f)} \qquad 19$$

where $e_{TX+}(t)$ represents the time domain electric field at a location just after the transmit antenna and $E_{TX+}(f)$ is its Fourier transform.

Combining Equations 17 and 19, then, allows for the transfer function of the channel to be seen as the ratio of the electric fields at the two antenna locations.

$$H_{CHAN}(f) = \frac{E_{RX}(f)}{E_{TX}(f)} \qquad 20$$

A figure of the setup can be seen in the figure below:

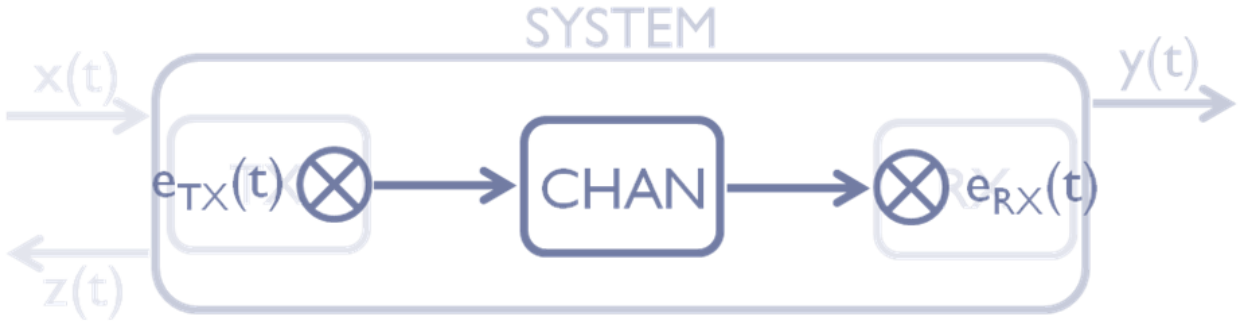

Figure 10: Channel Transfer Function, in terms of E-Fields

3.3 Validation

Equation 20 has been derived from theory, but before it is applied to actual human head models, it must be verified in simulation – to be sure that the behavior of specific theoretical channels can be correctly modeled in CST. It just so happens that these theoretically known channels are for single materials so these simulations are done with a single material only.

Simulations were set up such that an x-polarized plane wave was travelling in the +z-direction and would impinge on a block of some dielectric material. The dielectric block was infinite in the x- and y- directions (a symmetric boundary was used), and the block was semi-infinite in the +z-direction such that no waves would be reflected back and create a multipath-type environment. In the dielectric block, two probes were placed a distance *d* apart and were set to record the time domain electric field strength at their respective points. Once the simulation

was complete, the time domain electric field data was imported into MATLAB, FFTs were used to obtain the frequency content of those signals and then transfer function was computed and compared to the theoretical transfer function. A diagram of the simulation setup is shown below:

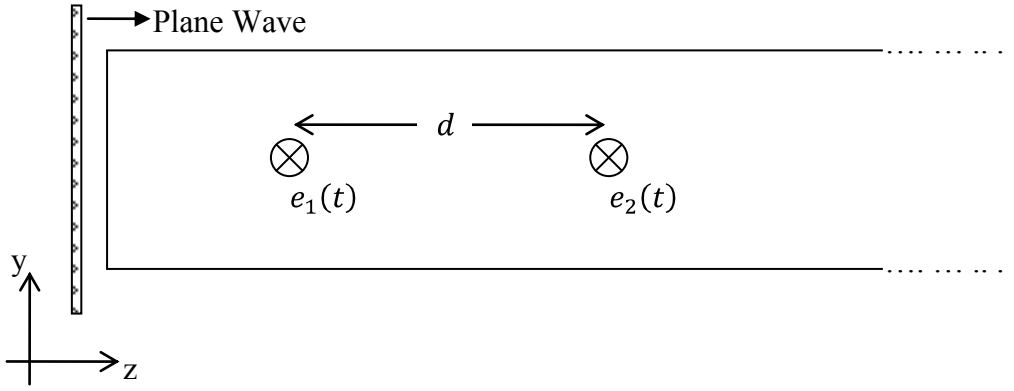

Figure 11: E-Field Verification Simulation Setup

Initially the material of the block was set to free space, to assure that the simplest of channels could correctly be approximated. Free space has a permittivity value of 1 and a conductivity of 0. The channel that one would expect is not exactly the model seen by the Friis transmission equation for the following reason: the Friss transmission equation assumes a spreading of the electromagnetic energy because it comes from an isotropic-like source (an antenna). This, of course, causes power loss as distance increases because as distance increases, the electromagnetic wave front travels spreads out over a larger spherical area and therefore its power per unit area will decrease. This yields a 1/r term that decreases power as distance increases [55]. However, because we are assuming that we are in the far field, we have assumed the wave to be approximately a plane wave. Plane waves do not exhibit any electromagnetic energy spreading, so the channel that one would expect through this medium is to have, over all frequency, a constant magnitude and a linear phase. The following plots show the time domain

electric field signals that were captured by the probes in CST, and the magnitude and phase comparisons from the theoretical transfer function and the calculated transfer function.

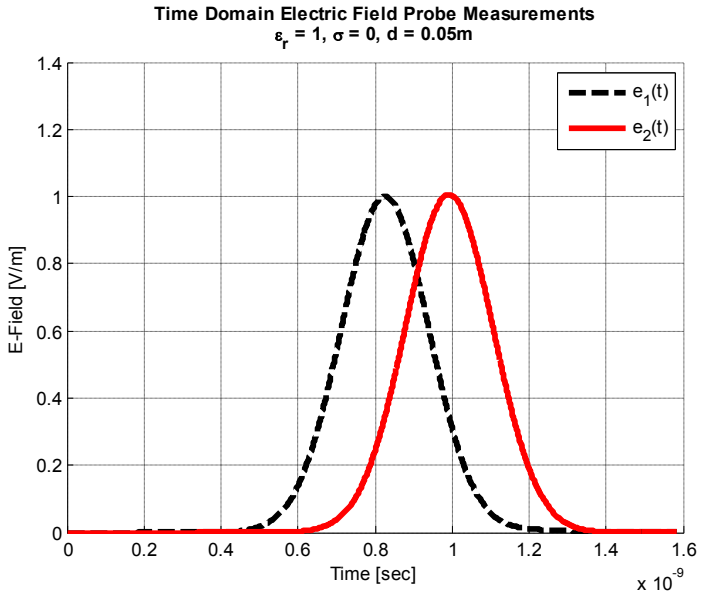

Figure 12: Time Domain Electric Field Probe Measurements, Free Space

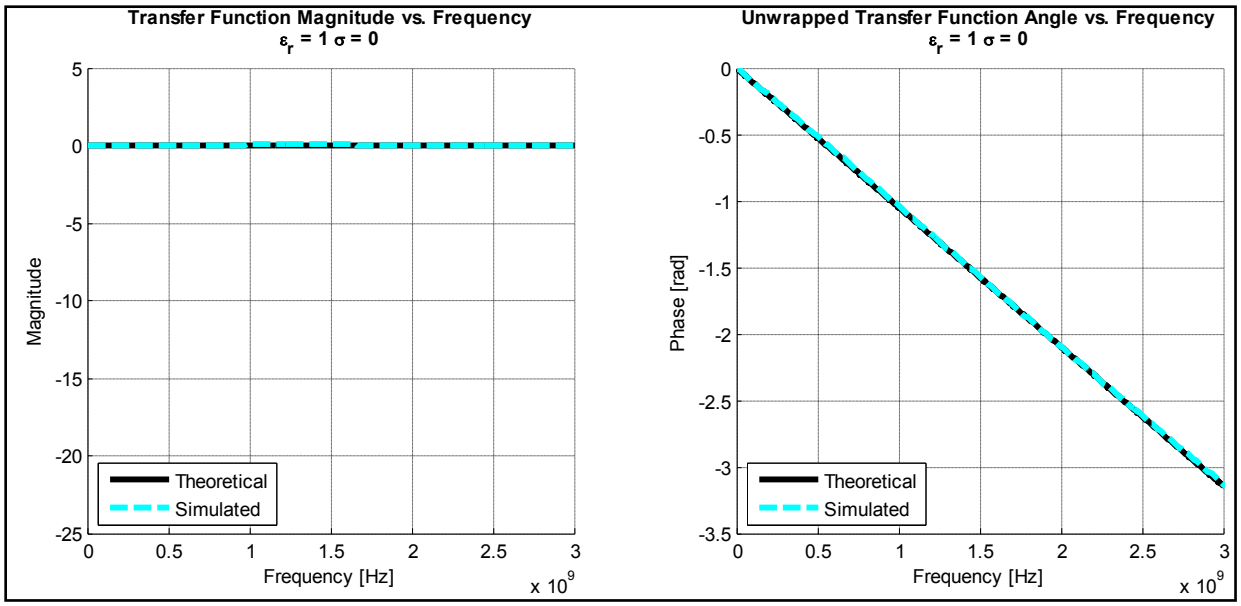

Figure 13: Theoretical/Calculated Transfer Function Comparison, Free Space

Figure 12 shows that the time domain pulses are, when compared to each other, simply shifts in time. *Figure 13* shows that the theoretical and calculated transfer functions are the same. There is a slight difference in magnitude from 1GHz to 1.5GHz, but this may be caused by minimal FFT errors and the accuracy of the solver.

For the second simulation, the permittivity and conductivity of the block were chosen to represent values that may be presented by the tissues in the human head. The permittivity was set as 50 and the conductivity was set to be 3 S/m. This permittivity is an average value for the head, and the conductivity was chosen because values of up to ~2.65 S/m can be obtained in the head – as seen by the values in the head model in CST. The time domain electric field measurements and the transfer function comparisons are shown below:

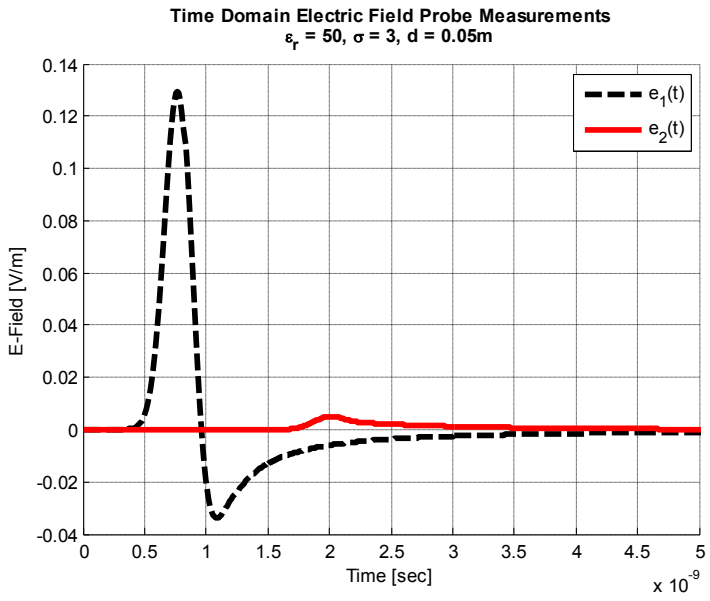

Figure 14: Time Domain Electric Field Probe Measurements, Approximate Head Values

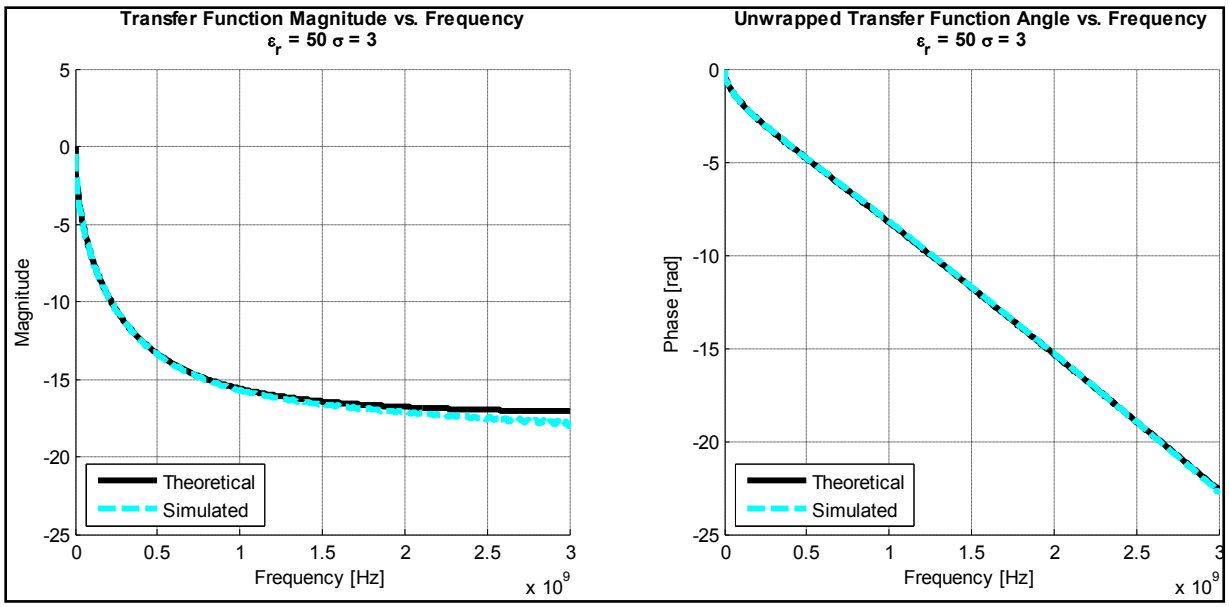

Figure 15: Theoretical/Calculated Transfer Function Comparison, Approximate Head Values

Figure 14 shows the effect of the conductance on the time domain signals. Travelling the same distance as the signals in free space we see that the signals have been attenuated a great deal. Regarding the theoretical and calculated transfer functions, as shown in *Figure 15*, we see that the magnitudes match well at lower frequencies and there can be errors of as much as 1dB at higher frequencies. This is caused by the fact that the E-field signal magnitudes start at such a low magnitude to begin with and the accuracy is achieved before the signals completely die down to exactly zero. The phase, however, matches perfectly with theoretical values. This level of accuracy is acceptable for further simulations.

4. Application of E-Field Technique on Human Body Model

4.1 Simulation Setup with Human Head Model

Now that the E-field ratio technique has been proven theoretically and verified through simulation, it can be applied to a more realistic model for analysis. The goal of the following simulations is to obtain the transfer functions that are presented by the human head. To achieve this, a plane wave will impinge on a human head model at some angle and propagate through it. Probes are placed every half a centimeter from the outside of the body to the center of the skull. All probe points are parallel to the plane wave such that the polarization of the E-field matches that of the probe. This setup can be seen in *Figure 16*. Four specific points are highlighted in the screen capture, each at a different depth into the skull: 0cm, 3cm, 5cm and 7cm. This specific screen capture is for the case that the plane wave hits the left side of the head. Simulations were done for the back, front and top of the head as well.

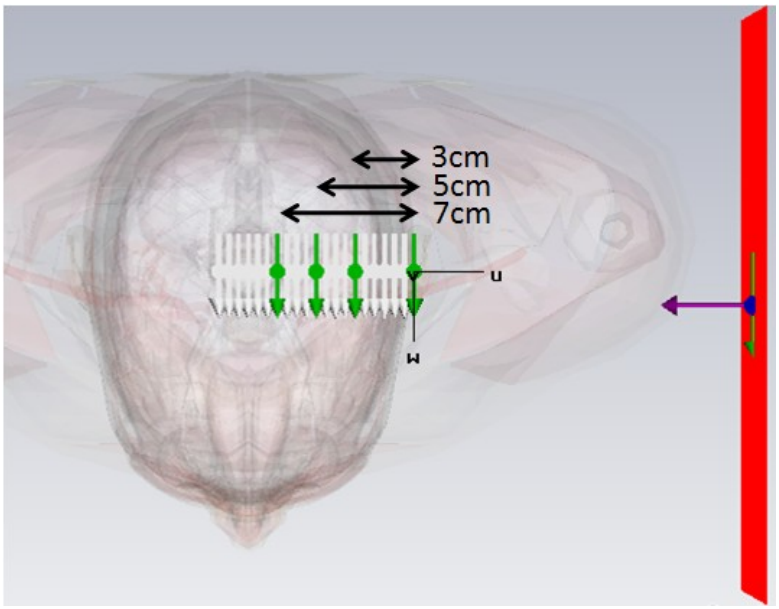

Figure 16: Setup for E-Field Simulations, Probes and Plane Wave

It should be noted that the entire human body was not used for these simulations. The model was cut as seen in *Figure 17*. All geometry below 38cm from the top-most point of the model was deleted; this leaves the full skull, the neck and part way down the shoulder. We also see that the central point of the coordinate system that will be used in the human body lies in the sagittal and coronal planes of the body and is 6.5cm from the top-most point of the model.

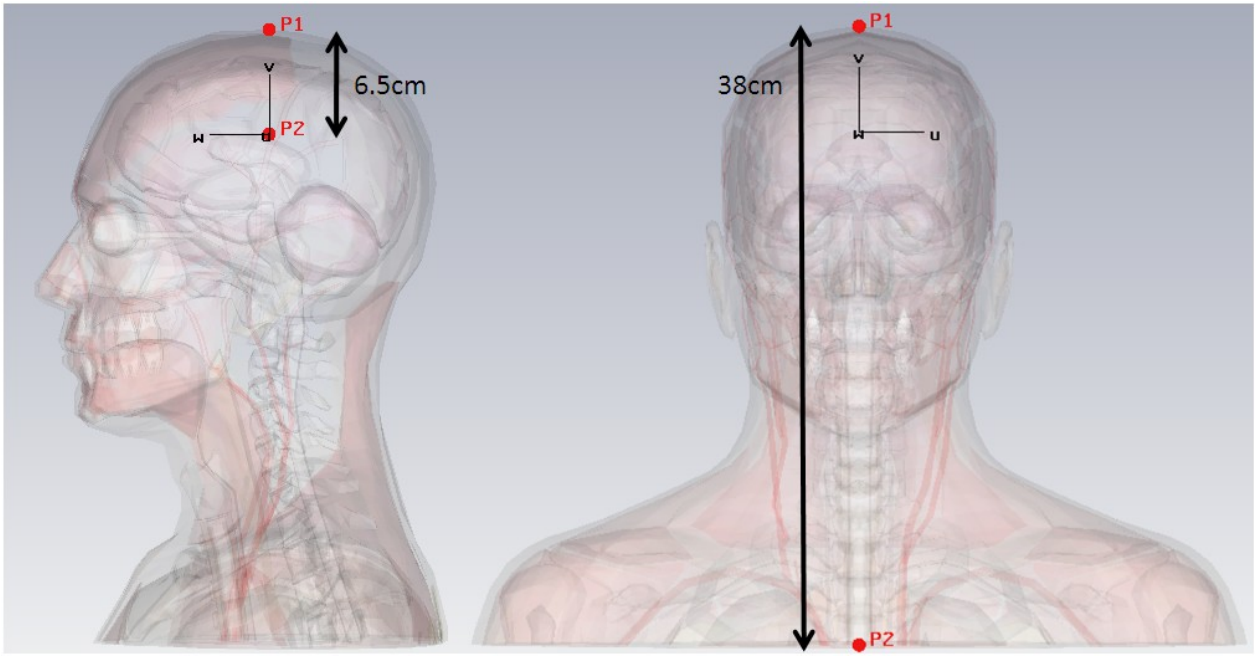

Figure 17: General Dimensions of the Human Body Model for E-Field Simulation

Also, before any results are shown for these simulations, dielectric profiles / cross-sections are necessary to understand exactly what is being simulated. These are shown below:

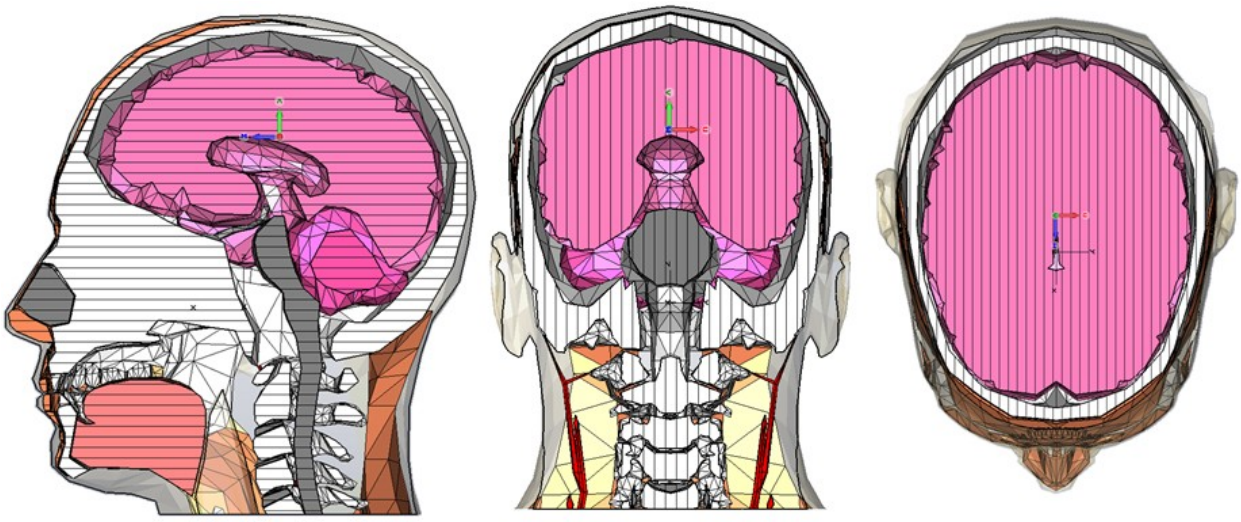

Figure 18: Axial Cross-Sections of the Human Head Model

The cross-sections in *Figure 18* can be further analyzed to describe the exact layers that are present for each specific incidence angle, but at a quick glance, it can be seen that the first material that the plane wave will encounter is the body exterior which has properties of body_average, then perhaps a very small amount of muscle and/or blood, then approximately 1.9 cm of cancellous bone and body_average tissue before entering the brain. It can also be seen that there is an oddly shaped 'empty-area' in the center of the brain that then leads down to the brain stem. This area has the electrical characteristics of body_average.

For reference, although many frequencies are being simulated, *Table 2*, below, shows the electrical characteristics used by the model for the tissues mentioned above at a frequency of $400MHz$.

Table 2: Electrical Characteristics of Several Relevant Body Tissues at 400MHz

Tissue	***Permittivity***	***Conductivity*** $[S/m]$
Brain	49.25	0.7602
Body Average	50.00	0.5563
Cancellous Bone	21.61	0.2361
Muscle	58.50	0.9595
Blood	65.00	1.592

Continuing on with the setup of the actual simulations, the plane wave is set up such that its excitation is that of a Gaussian pulse. Gaussian pulses are used because of their wide frequency content. The input Gaussian pulse and its frequency content are seen in *Figure 19* and *Figure 20*. It is a short pulse in the time domain, less than two nanoseconds, and it contains all frequencies, albeit not equally, from DC to upwards of three gigahertz. The frequency domain content of this signal is also of Gaussian shape and is centered at 0Hz.

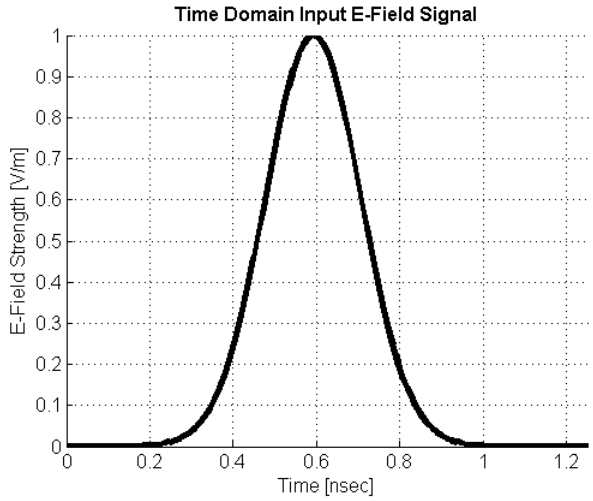

Figure 19: Time Domain Input E-Field Signal, Gaussian Pulse

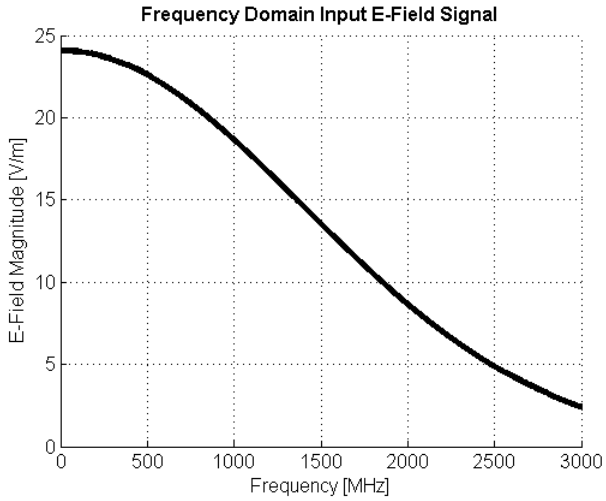

Figure 20: Frequency Domain Input E-Field Signal, FFT of the Gaussian Pulse

With this setup, only one simulation is needed to record the time domain signals seen at all probe locations. The reference signal that was used – meaning the signal that will be used as the input signal to the head – is not the outer Gaussian signal, but rather the signal recorded at just the outside of the head (seen at 0cm in *Figure 16*). For the plane wave that impinges upon the left side of the head, this reference signal is seen in *Figure 21*.

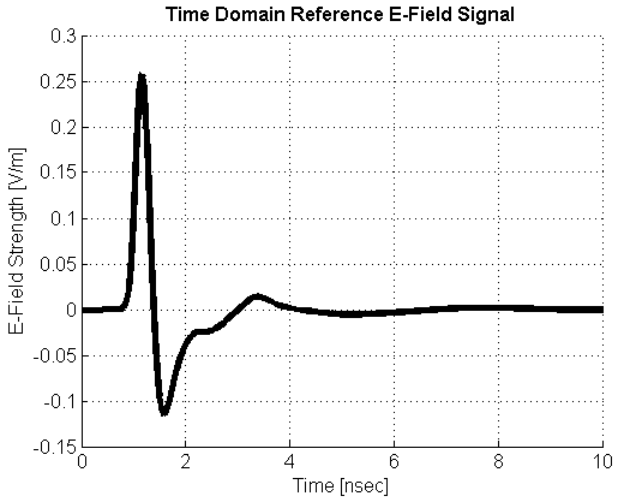

Figure 21: Time Domain Reference E-Field Signal, Left Side of the Head

The deformation of this signal is due to a complex array of reflections and transmissions as the wave propagates through the complex geometry of the head. It is this wave that is seen at the side of the head and it is this wave, therefore, that is used as the reference signal when calculating the transfer functions.

Further, *Figure 22* shows the time domain signals for three other depths into the skull; namely 3cm, 5cm and 7cm. As the signal travels through the head we clearly see attenuation, a smoothing and an elongation of the reference signal. The peak of the signal has attenuated by approximately 75% by the time it has travelled only three centimeters and has been attenuated 96% by the time it gets to seven centimeters. The elongation and smoothness of the time signals could be due to the quick attenuation of higher frequencies that then tends to leave longer wavelengths present and will act as a low-pass filter and rid the signals of any high frequency components.

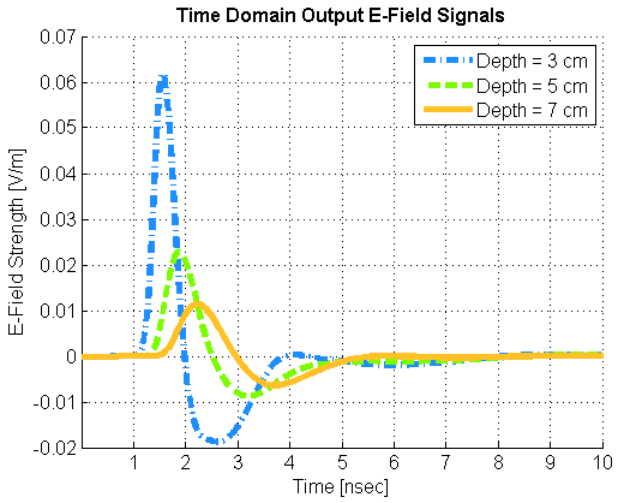

Figure 22: Time Domain E-Field Signals, Depths of 3cm, 5cm, 7cm, Left Side of the Head

Exporting this data directly into MATLAB allows us to easily take the FFT of the data. When this is done, we see the results below in *Figure 23* and *Figure 24*.

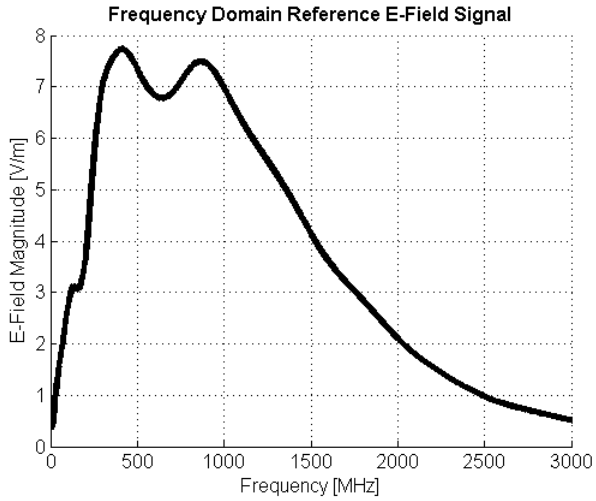

Figure 23: Frequency Domain Reference E-Field Signal, Left Side of the Head

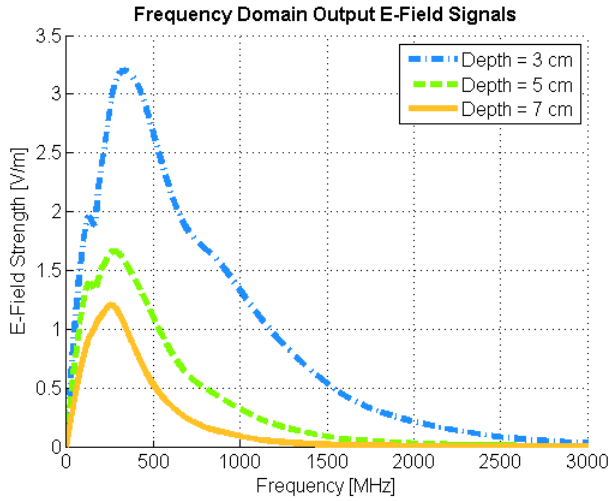

Figure 24: Frequency Domain E-Field Signals, Depths of 3cm, 5cm, 7cm, Left Side of the Head

Figure 23 shows the FFT of the reference signal. We see, all across the frequency range of 300MHz to 3GHz, that the Gaussian pulse has been attenuated and distorted by its initial impact with the head. The most attenuation, however, is seen at frequencies of 300MHz or less. This makes sense because the permittivity of tissue at low frequencies is extraordinarily high.

Looking at the laws of transmission and reflection, it is seen that when an EM wave travels from a material with a low dielectric constant to one that has a high dielectric constant, most of the wave is reflected back. This is exactly the situation that is seen here: the input Gaussian pulse is travelling in free space which has the lowest value of electrical permittivity and it then impacts the human head which, for low frequencies, has extremely high permittivity. This causes the effect that is seen in *Figure 23*, and subsequent figures, where there is a very low value for the frequencies seen at low frequencies up to 300MHz.

Figure 24 shows the frequency domain content of the signals that were captured at 3cm, 5cm and 7cm into the skull. Attenuation is seen across the entire frequency range, but the most obvious evidence of uneven attenuation versus frequency is the difference in the maxima seen at 400MHz and 900MHz. *Figure 23* clearly shows two distinct maxima at these frequencies. After only three centimeters of propagation we see in *Figure 24* we see almost no trace of that local maximum, although the one at 400MHz remains clear. The clear frequency dependent attenuation is shown as well when observing how the values of the maximum moves towards lower frequency as the depth increases. This is caused by the fact that increased attenuation at higher frequencies begin to 'erode' the peak from the high frequency side.

4.2 Transfer Functions

4.2.1 Transfer Function Magnitude

4.2.1.1 E-Field Simulations

From this data, the transfer function are the calculated for each distance using Equation 20. The transfer function is plotted for four separate incidence angles; namely the front, side, back and top of the head.

To the results, for the left side of the head, *Figure 25* shows the calculated transfer functions for depths of 2-8cm in one centimeter intervals. It only shows the magnitude of the channel and is only shown for the frequency range of 300MHz to 3GHz. We begin at a depth of 2cm because the average depth (as averaged from the top, side, front and back of the head) into the human head to get to the surface of the brain (which is the minimum distance to which a sensor would be implanted) is 1.977cm. Therefore, the value of 2cm is used as the starting point for these plots.

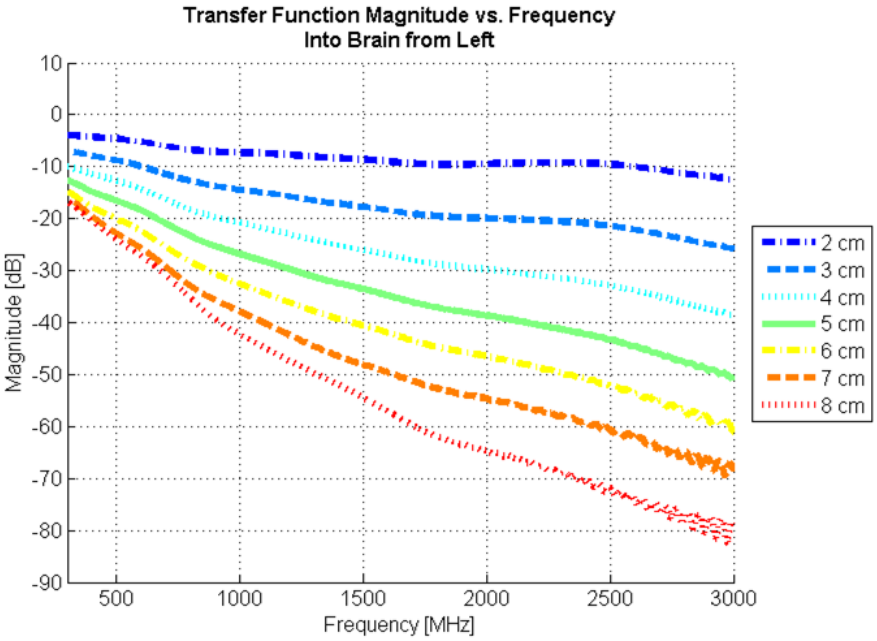

Figure 25: Transfer Function Magnitude, 2:1:8cm, Left Side of the Head

Overall, as expected, *Figure 25* shows that as distance and frequency increase, magnitude decreases. The top-most dotted line shows the magnitude of the transfer function for a depth of 2cm, the next is 3cm, etc. The rates at which the attenuation occurs, however, seems to accelerate as distance increases. This can be seen by observing how the slopes of the respective distance lines become more and more negative as distance increases. The curves do, however,

seem to be more-or-less predictable. Although there is a complex dependence on frequency and distance, we see that it is not difficult to imagine where the curves of other distance values would lie. It is also important to note in this figure the behavior of the curves past 2.5GHz. There is a clear change in the slopes of all the curves. At deeper depths, 2.5GHz is also the approximate point at which noise begins to corrupt the data. Looking back as far as to *Figure 15*, which shows the theoretical and simulated transfer function plots for a simple block of frequency dependent media, 2.5GHz has some error. It is possible that because of the amount of attenuation seen at larger depths and higher frequencies is so much that the accuracy of the solver begins to degrade at approximately this frequency.

Similar simulations were repeated for plane waves approaching the head from different angles of incidence. Results have already been shown for the plane wave propagating towards the left side of the head, further results will be shown for a plane wave propagating towards the front, the back and the top of the head. *Figure 26* shows the coordinate systems that were used for all simulations and their relative offsets from the central coordinate system that is located at the center of the head.

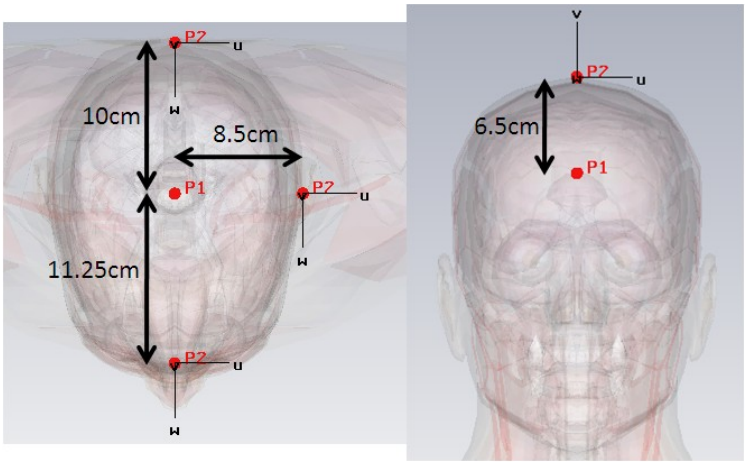

Figure 26: Offset Coordinate System Dimensions for Different Incidence Angles

Figure 27, *Figure 28* and *Figure 29* show the transfer function results for the other orientations.

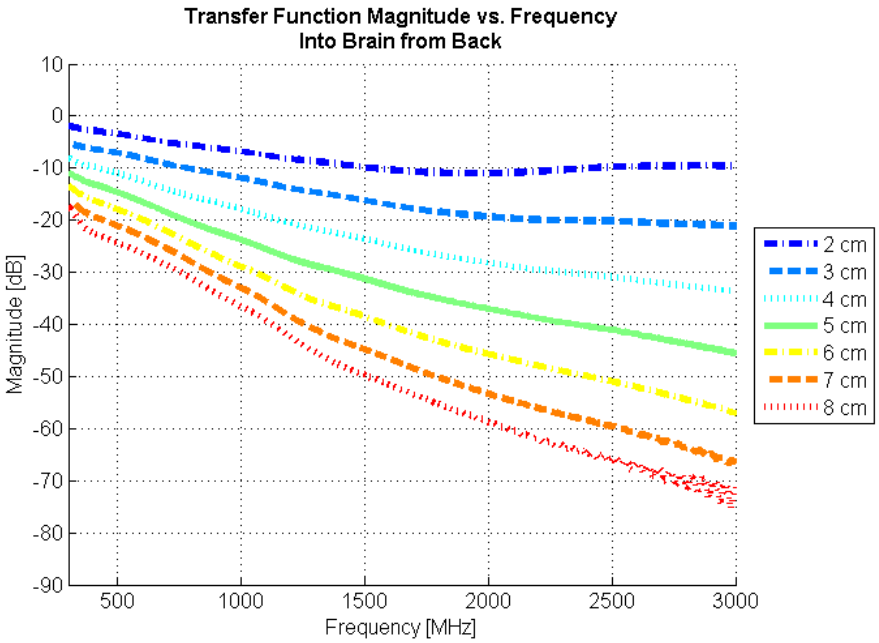

Figure 27: Transfer Function Magnitude, 2:1:8cm, Back of the Head

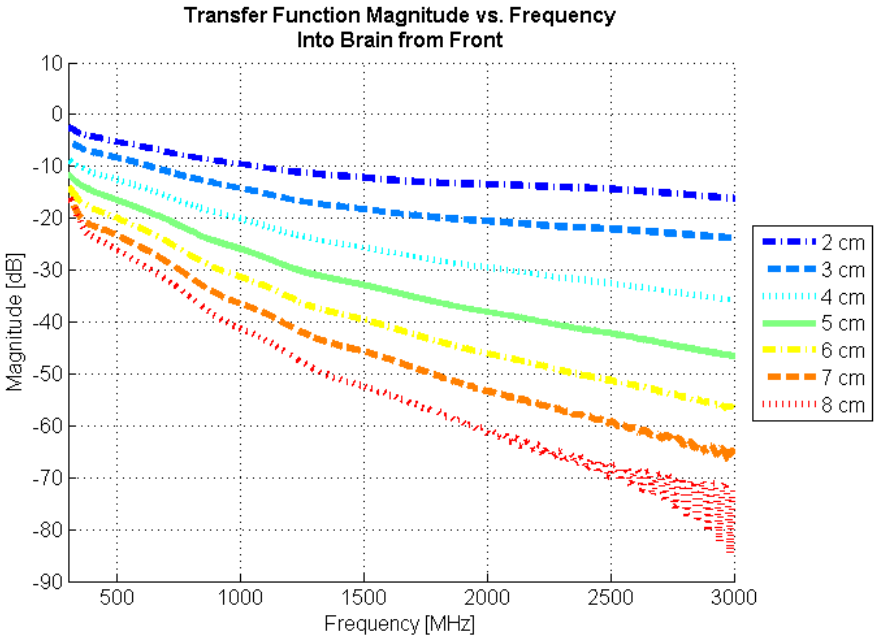

Figure 28: Transfer Function Magnitude, 2:1:8cm, Front of the Head

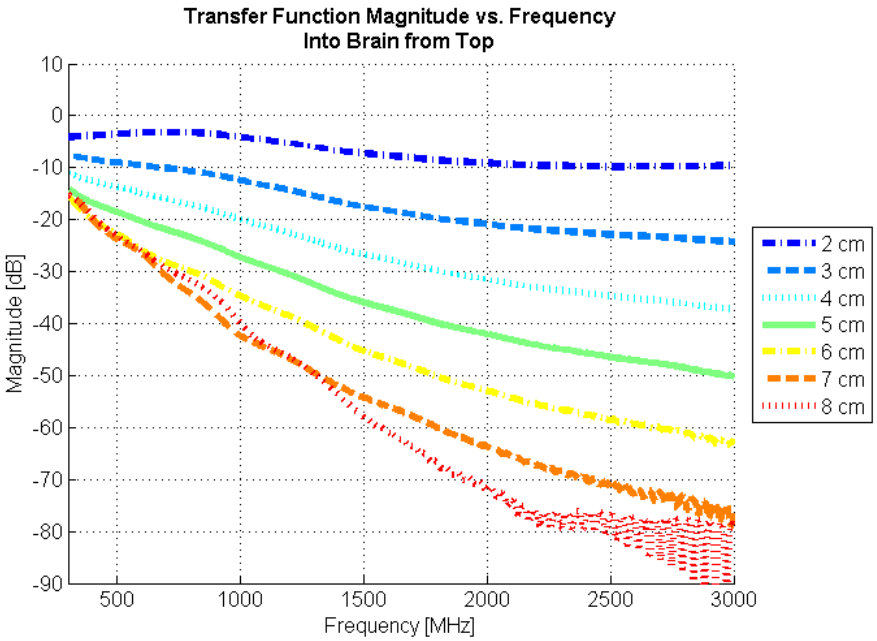

Figure 29: Transfer Function Magnitude, 2:1:8cm, Top of the Head

The most interesting result obtained from the transfer functions that have been generated is how alike they are, despite propagation through different layers of tissue and the different geometries seen by each angle. *Figure 27* shows the transfer function when the plane wave propagates through the back of the head, is extremely similar to *Figure 25* (which shows the left side) and *Figure 28* (which shows the front). For these three plots it is seen that all distance curves, for all frequencies up to 2.0GHz, match each other with a maximum deviation of approximately 4.5dB. From this, it can be seen that communication channel presented by communicating *to* an implant from an antenna that is outside the human head is very similar for the transverse plane that cuts through the middle of the skull.

Figure 29, which shows results for a plane wave that impacts the top of the head, is the most different of the plots. The curves for the smaller distances match well, but the curves for the deeper distances show much more loss. This is most likely caused by a deep patch of 'body exterior' that is found in the center of the human body model's brain. This change in permittivity

value causes more reflections and transmissions to occur and the loss of power that results is shown clearly in this figure.

4.2.1.2 Poynting Vector Simulations

A more well known technique for generating the magnitude response of a complex channel using electromagnetic software is, as was mentioned before, by using the Poynting vector. The Poynting vector, or average power density, is defined over a single period as the following:

$$\mathcal{P}_{av} = \frac{1}{2}\mathrm{Re}[\boldsymbol{E} \times \boldsymbol{H}^*] \qquad 21$$

and has units of $[W/m^2]$ [47].

A single simulation was set up, with the plane wave approaching from the left, such that the electric and magnetic fields were recorded for the entire geometry at three specific frequencies; 400MHz, 900MHz and 2400MHz. These frequencies were chosen because they correspond to the frequencies around the MedRadio and ISM bands that are licensed for use in medical implant communications. From the electric and magnetic fields, Equation 21 was used to generate the three-dimensional Poynting vector field. Once generated, the magnitude was plotted along the line that passed through the center of the head and was perpendicular to the plane wave. The resolution of the Poynting vector plot in three dimensions was generated down to every 0.01mm. The power was then normalized to the value seen at the edge of the head and was then translated to decibels and plotted.

To double check that the E-field ratio technique was working correctly, the E-field ratio results were plotted in three dimensions and the Poynting vector results were laid on top for comparison. This is seen below in *Figure 30*.

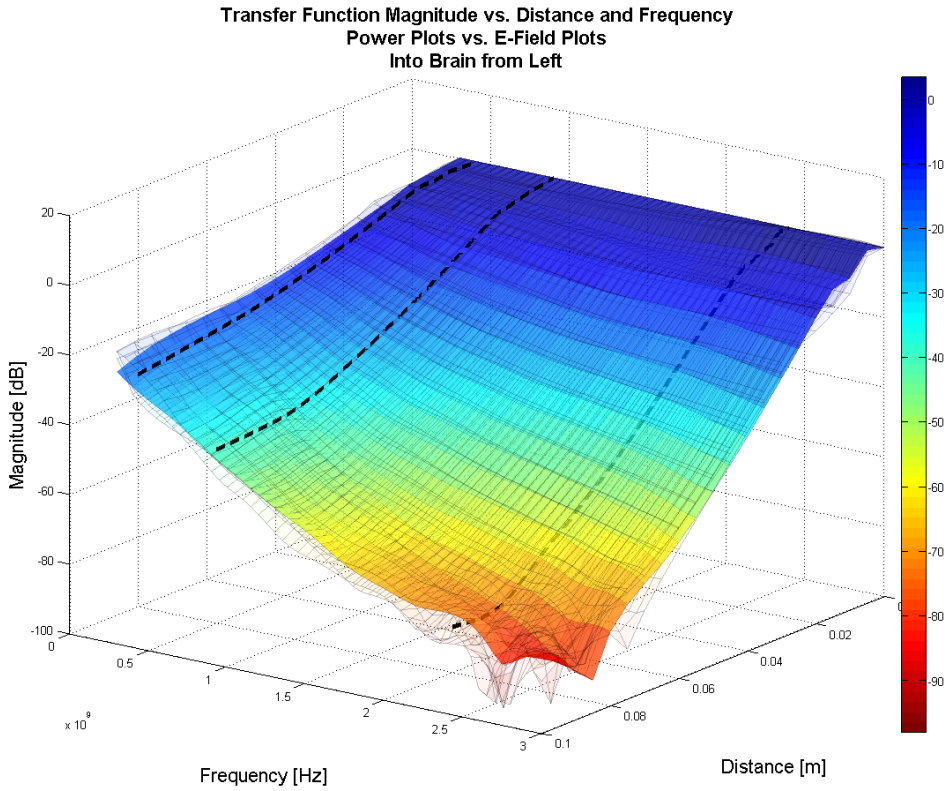

Figure 30: 3D Comparison Between E-Field Ratio and Poynting Vector Techniques

The main colored plane is shows the results obtained for the left side of the head, the three bold dashed lines are the results obtained from the Poynting vector simulation and lightly overlaid are the results for the front, back and top of the head. We see a general similarity in the plots. In two dimensions, however, it is easier to compare the exact frequencies. This is shown below:

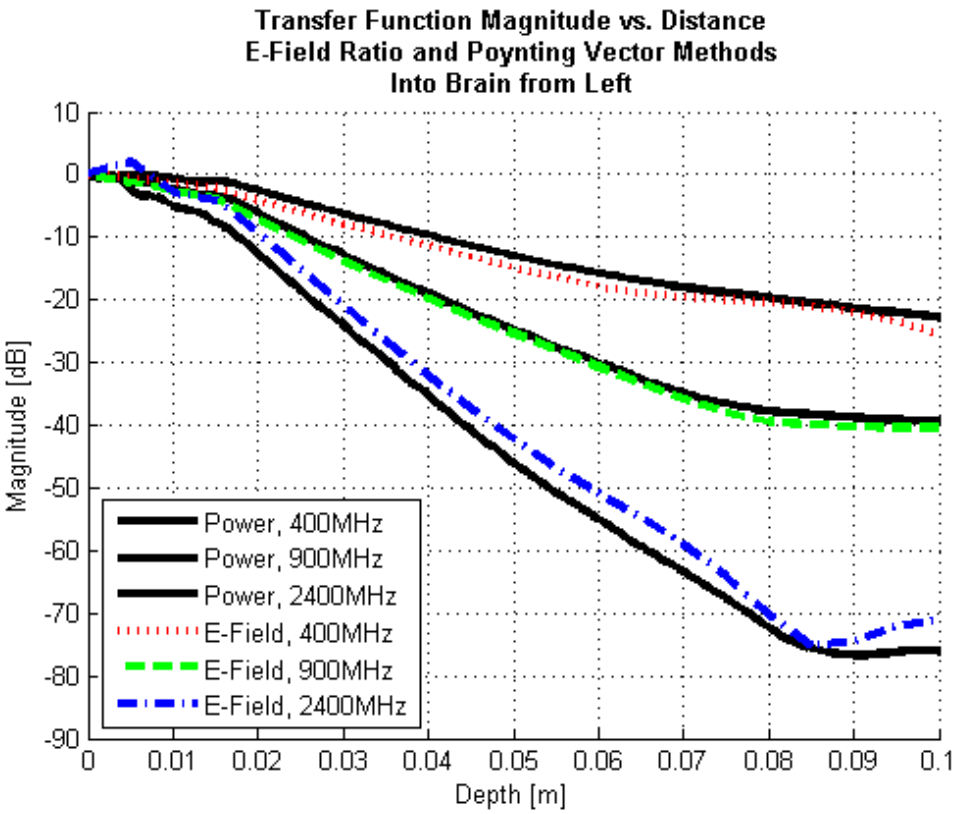

Figure 31: Comparison Between E-Field Ratio and Poynting Vector Techniques

As *Figure 30* and *Figure 31* show, both techniques have generated the same magnitude response over all depths from 0cm to 10cm for the frequencies of 400, 900 and 2400MHz. These results clearly verify that the E-field technique is correctly being implemented and is obtaining correct results in their simulations.

4.2.2 Transfer Function Phase

Equation 20 can be used to calculate the transfer function of the human head using the ratio of the electric fields. Unwrapping the phase of this data can be done and is shown in two

sets of four figures below; the first set of figures plots phase vs. frequency, and the second set of figures plots phase vs. depth into the skull. These are *Figure 32* and *Figure 33*, respectively.

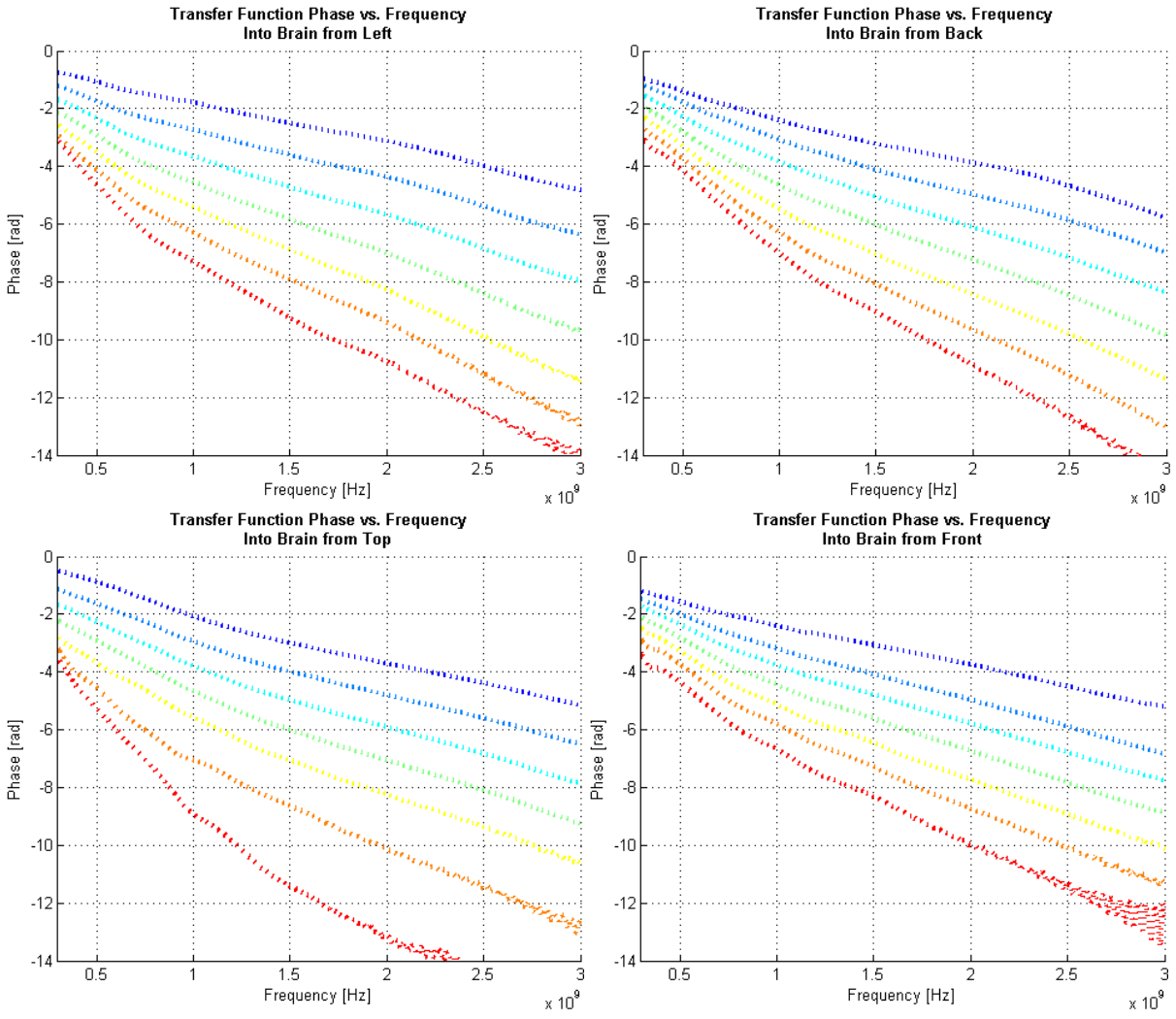

Figure 32: Transfer Function Phase vs. Frequency, From Left, Back, Top and Front, Distances of 2cm:1cm:8cm

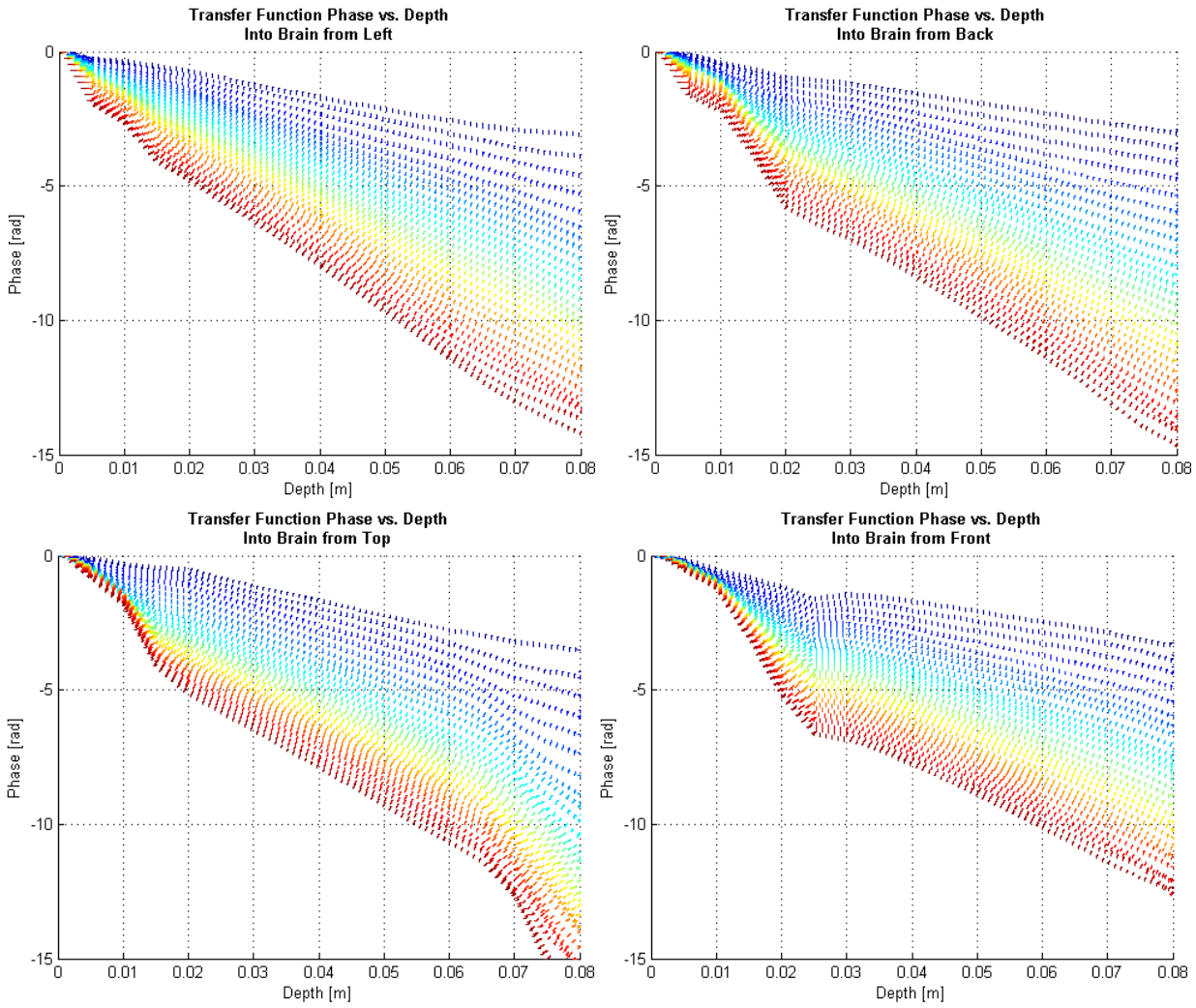

Figure 33: Transfer Function Phase vs. Distance, From Left, Back, Top and Front, Frequencies of 300MHz:100MHz:3000MHz

No analysis is done with the phase information, although possible future work could be done to do so. Use of the E-field technique does allow, as seen above, the plotting of phase data for complex problems. By plotting the phase vs. distance as seen in *Figure 33*, one can attempt to cross reference the phase data with the cross-sectional tissue data and analyze the effect that each tissue seems to have on the phase. A cursory glance shows that in the brain, which is found at greater than 2 cm deep (on average) gives linear, but changing, phase for increasing frequency.

5. Modeling the Human Head as a Communication Channel

5.1 Least Square Approach to Data Fitting

Once the data has been obtained, the goal is to fit a communication type curve model to this data. Doing so will allow us to characterize the overall type of communication system that is present. For simplicity, we begin by trying to fit a linear curve to the data. This curve will be fit using the classical least squares method of curve fitting [52].

The problem of being able to fit curves to data is present in all areas of engineering. A simple example is shown below in *Figure 34*.

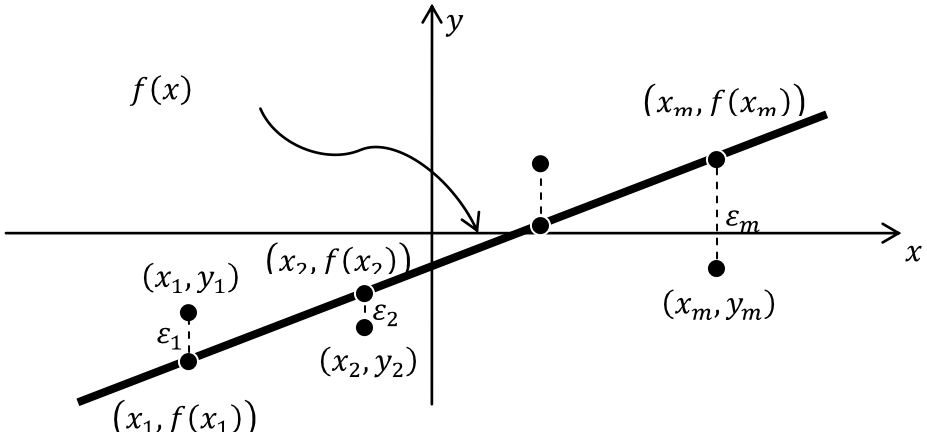

Figure 34: Simple Example of Linear Curve Fitting

The goal is then to obtain the linear equation that will result in the smallest value for the mean squared error (MSE). Note that the absolute error corresponding to the ith data point can be defined as

$$\varepsilon_i = |f(x_i) - y_i| = |\alpha + \beta x_i - y_i| \qquad 22$$

Therefore, we must find values for α and β such that the MSE given by

$$\sum_{i=1}^{m} {\varepsilon_i}^2 = \sum_{i=1}^{m} |\alpha + \beta x_i - y_i|^2 \quad (23)$$

is a minimum. This is done by taking the derivatives with respect to α and β and setting them equal to zero. Rearranging these equations will then yield the following equations:

$$\begin{aligned} \left(\sum_{i=1}^{m} 1\right)\alpha + \left(\sum_{i=1}^{m} x_i\right)\beta &= \sum_{i=1}^{m} y_i \\ \left(\sum_{i=1}^{m} x_i\right)\alpha + \left(\sum_{i=1}^{m} {x_i}^2\right)\beta &= \sum_{i=1}^{m} x_i y_i \end{aligned} \quad (24)$$

Define:

$$\boldsymbol{A} = \begin{pmatrix} 1 & x_1 \\ 1 & x_2 \\ \vdots & \vdots \\ 1 & x_m \end{pmatrix}, \qquad \boldsymbol{b} = \begin{pmatrix} y_1 \\ y_2 \\ \vdots \\ y_m \end{pmatrix}, \qquad \boldsymbol{x} = \begin{pmatrix} \alpha \\ \beta \end{pmatrix}, \quad (25)$$

where $\boldsymbol{x}$ is clearly a column matrix made up of the unknown coefficients, $\boldsymbol{b}$ is a column matrix of the actual observed values and $\boldsymbol{A}$ is a matrix made up the variable values that correspond to the observed values in $\boldsymbol{b}$. These then simplify Equation 24 to the form of $\boldsymbol{Ax} = \boldsymbol{b}$. Therefore the least square estimate of $\boldsymbol{x}$ can be solved for using the following equation:

$$\hat{\boldsymbol{x}} = (\boldsymbol{A}^T\boldsymbol{A})^{-1}\boldsymbol{A}^T\boldsymbol{b} \quad (26)$$

For which the value of the Minimum Mean Squared Error can be found as:

$$MMSE = (\boldsymbol{A}\hat{\boldsymbol{x}} - \boldsymbol{b})^T(\boldsymbol{A}\hat{\boldsymbol{x}} - \boldsymbol{b}) \quad (27)$$

It is known that when one fits a curve using the minimum mean square error technique seen above in Equation 26, the value of the actual function can be defined in terms of the estimate by using the following equation:

$$y = f(x) + \Omega \quad (28)$$

where

$$\Omega = N(0, \sigma_{error}^2) \quad (29)$$

and

$$\sigma_{error} = \sqrt{\frac{MMSE}{m}} \tag{30}$$

for which m is the total number of points that were used to obtain the estimate [53].

This can easily be extended for multiple variable linear regressions as well. As an example, say an experiment had two variables on which it depended; the linear equation would now be of the form: $f(x_1, x_2) = \alpha_0 + \alpha_1 x_1 + \alpha_2 x_2$ and the new format for the $\boldsymbol{A}$, $\boldsymbol{b}$ and $\boldsymbol{x}$ matrices are seen below:

$$\boldsymbol{A} = \begin{pmatrix} 1 & (x_1)_1 & (x_2)_1 \\ 1 & (x_1)_1 & (x_2)_2 \\ \vdots & \vdots & \vdots \\ 1 & (x_1)_1 & (x_2)_m \\ 1 & (x_1)_2 & (x_2)_1 \\ 1 & (x_1)_2 & (x_2)_2 \\ \vdots & \vdots & \vdots \\ 1 & (x_1)_2 & (x_2)_m \\ \vdots & \vdots & \vdots \end{pmatrix}, \quad \boldsymbol{b} = \begin{pmatrix} y_{(x_1)_1,(x_2)_1} \\ y_{(x_1)_1,(x_2)_2} \\ \vdots \\ y_{(x_1)_1,(x_2)_m} \\ y_{(x_1)_2,(x_2)_1} \\ y_{(x_1)_2,(x_2)_2} \\ \vdots \\ y_{(x_1)_2,(x_2)_m} \\ \vdots \end{pmatrix}, \quad \boldsymbol{x} = \begin{pmatrix} \alpha_0 \\ \alpha_1 \\ \alpha_2 \end{pmatrix}, \tag{31}$$

Further, not only can this be extended for multiple linear regressions, but it can be extended for use in polynomial curve fitting. What is shown below, however, is the simplest multivariable linear regression. Although it is trivially simple to modify the MATLAB m-files to obtain better fitting polynomial curves, the final goal is not to fit some arbitrary curve to the data, but to obtain the best fitting (MMSE) for the *communication-type* path loss model through the use of this technique. The best way, then, to show the procedure to do this is to begin with the simple linear model and extend it from there. Results for a second order polynomial fitting, however, can be found in APPENDIX A.

5.1.1 Simple Linear Model

The simplest multivariable format for the $\boldsymbol{A}$, $\boldsymbol{b}$ and $\boldsymbol{x}$ matrices seen in Equation 31 is exactly what is needed for the frequency and distance dependent simulated curves that have been obtained. We then use the following linear equation:

$$\widehat{X}(f,d) = k + n(d) + m\left(\frac{f}{f_0}\right) \qquad 32$$

and define

$$\boldsymbol{x} = \begin{pmatrix} k \\ n \\ m \end{pmatrix} \qquad 33$$

This now allows Equation 32 to be solved in a MMSE-type method using MATLAB. Note that f_0 is an arbitrary frequency value and is assigned the value of 250MHz for all curve fitting. The three constants that define the estimated curves are generated using d as ranging from *2cm : 1cm : 8cm* and f ranging from *300MHz : 1MHz : 3GHz*. For the left side of the skull, results are shown below:

Table 3: MMSE Variables and Ave Error for Simple Linear Model, From Front

k	22.07
n	-695.1
m	-2.966
σ_{error}	$4.567\ dB$

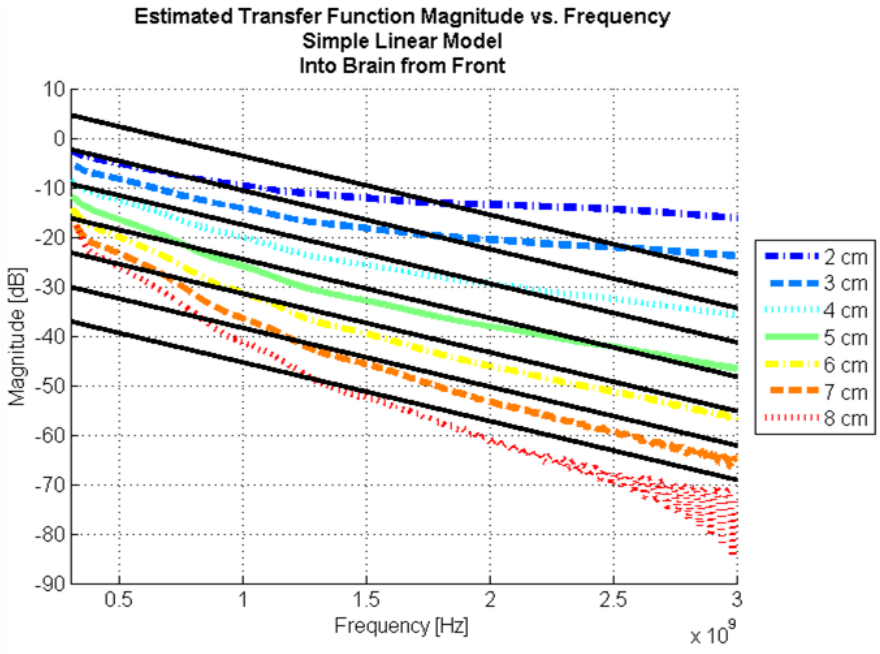

Figure 35: Simulated and Estimated Curves, Simple Linear Fit

This fit, as expected, estimates each individual trace as a separate line. Clearly, though, the largest cause of error stems from the fact that no matter which trace is approximated, all of the curves have the same slope. We see from the dotted lines in *Figure 35* that as distance increases, the slope becomes more negative. This is not taken into account in this simple linear estimate as seen by the solid lines that approximate the loss. This, therefore, leads to an error variance of 4.567dB. Results for all the simple linear fittings are seen below in *Table 4*.

Table 4: MMSE Variables and Ave Error for Simple Linear Model, All Angles

	Front	***Left***	***Back***	***Top***
k	22.0696	25.8041	24.8969	31.7445
n	−695.0829	−762.5451	−706.558	−864.8273
m	−2.9655	−3.0793	−3.0226	−3.5139
$\sigma_{error}\ [dB]$	4.567	5.438	5.091	6.750

The values obtained for k, n, m and the σ_{error} are very similar, especially for the front, left and back of the head.

5.1.2 Modified Linear Model

It is possible to modify Equation 32 to artificially add distance dependent slope over frequency (and frequency dependent slope over distance). This is seen in the following equation:

$$\widehat{X}(f,d) = k\left(\frac{d}{d_0}\right) + n(d)\left(\frac{f}{f_0}\right) + m\left(\frac{f}{f_0}\right)\left(\frac{d}{d_0}\right) \qquad 34$$

where d_0 is an arbitrary distance value and is assigned the value of 2cm for all curve fitting. Modifying the matrices in the MATLAB code to account for this new equation allows us to obtain the following results:

Table 5: MMSE Variables and Ave Error for Modified Linear Model, From Left

k	-5.081
n	-0.024
m	-1.206
σ_{error}	$2.168\ dB$

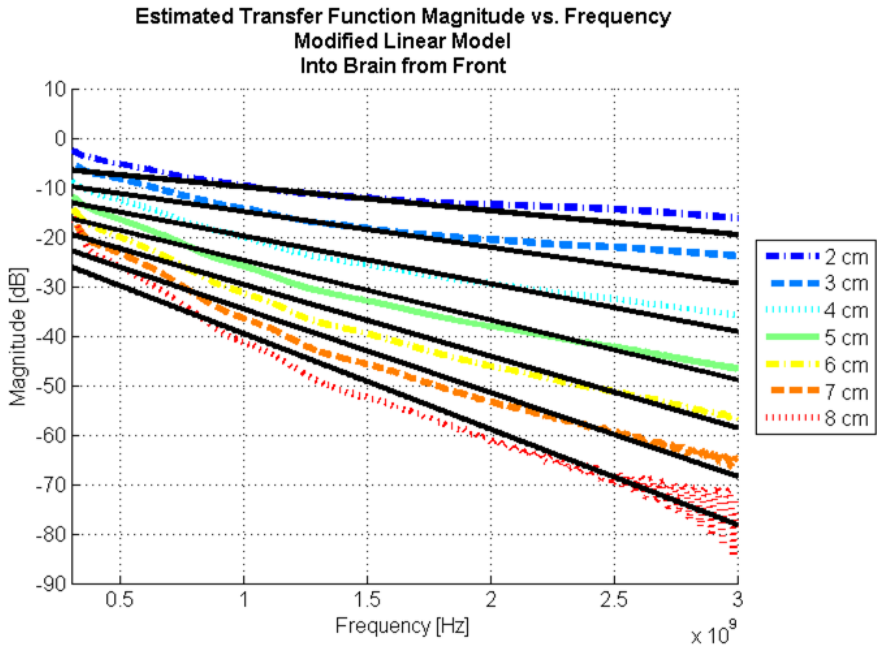

Figure 36: Simulated and Estimated Curves, Modified Linear Fit

It is clear, now, that frequency and distance are not independent variables. Because of this newly forced dependence, we see a distinct change in slope as distance increases and, overall, a better fit. Looking at the variance of the error across the entire frequency range of 300MHz to 3GHz we see a 47.47% decrease from the simple linear fit to only 2.168dB for this modified linear fit. Results for all the modified linear fittings are seen below in *Table 6*.

Table 6: MMSE Variables and Ave Error for Modified Linear Model, All Angles

	Front	***Left***	***Back***	***Top***
k	-5.0814	-4.9005	-4.1845	-4.6023
n	-0.024109	-0.025627	-0.024961	-0.029519
m	-1.2055	-1.2814	-1.2481	-1.4759
$\sigma_{error}\ [dB]$	2.168	3.172	2.868	4.692

5.2 Theory for Communications Models

The previous fits that have been applied to the data are linear fits. Linear fits, however, are not based on any sort of communication model. The real benefit of using such models is in recognizing the technique that was used to fit it. This will become apparent soon.

It has been seen that an indoor propagation model has been used in the past to fit body channels and it should, therefore, be attempted next [38] [40]–[42]. This is a well known model and has been thoroughly studied [53]. A model derivation is found in [54] and is summarized here.

5.2.1 Distance and Frequency Dependent Indoor Propagation Model

We are looking to develop a generic channel model that contains both distance and frequency dependence that is based in some sort of communications theory. To begin then, we will assume simplicity in our model and we assume that frequency and distance are independent. This leads to the following generic path loss equation:

$$PL(f,d)_{LINEAR} = PL(d)_{LINEAR}\, PL(f)_{LINEAR} \quad 35$$

where

$$PL(d)_{LINEAR} = (PL_0)\left(\frac{d}{d_0}\right)^{-n} \quad 36$$

$$PL(f)_{LINEAR} = \left(\frac{f}{f_0}\right)^{-m} \quad 37$$

Equations 36 and 37 are known as power law models. Other models exist, such as breakpoint models, in which there are different exponential attenuation exponents for different distance and frequency ranges, but they will not be considered here as they are beyond the scope of this work. It should also be noted that the subscript $_{LINEAR}$ is denoting that the power loss values are not yet in dB. These two equations can then be combined to yield:

$$PL(f,d)_{LINEAR} = (PL_0)\left(\frac{d}{d_0}\right)^{-n}\left(\frac{f}{f_0}\right)^{-m} \quad 38$$

But $PL(f,d)$ is a ratio of W/W and our data is V/V. We must be careful, then, when substituting in our data. This can be corrected as seen in [45] by taking the square root of the equation:

$$\widehat{X}(f,d)_{LINEAR} = \sqrt{(PL_0)\left(\frac{d}{d_0}\right)^{-n}\left(\frac{f}{f_0}\right)^{-m}} \quad 39$$

We can now convert to dB:

$$20\log_{10}\left[\widehat{X}(f,d)_{LINEAR} = \sqrt{(PL_0)\left(\frac{d}{d_0}\right)^{-n}\left(\frac{f}{f_0}\right)^{-m}}\right] \rightarrow$$

$$\widehat{X}(f,d)_{dB} = k - n\left[10\log_{10}\left(\frac{d}{d_0}\right)\right] - m\left[10\log_{10}\left(\frac{f}{f_0}\right)\right] \quad 40$$

where

$$k = 10\log_{10}(PL_0) \quad 41$$

and is a constant.

5.2.2 Extended Indoor Propagation Model

The first half of Equation 40 is known as the indoor propagation model. This model is only dependant on distance and is very well known. Through theory and an assumption of independence, we have extended the indoor propagation model to include another separate term that is dependent on frequency. Because Equation 40 is now in dB, we see that, essentially, it is now another linear equation. We can see how similar Equations 32 and 40 are to each other, and therefore we can solve these equations the same way. Using Equation 40 as our model, we obtain the following results:

Table 7: MMSE Variables and Ave Error for Simple Indoor Propagation Model, From Left

k	20.07
n	6.899
m	3.666
σ_{error}	5.039 dB

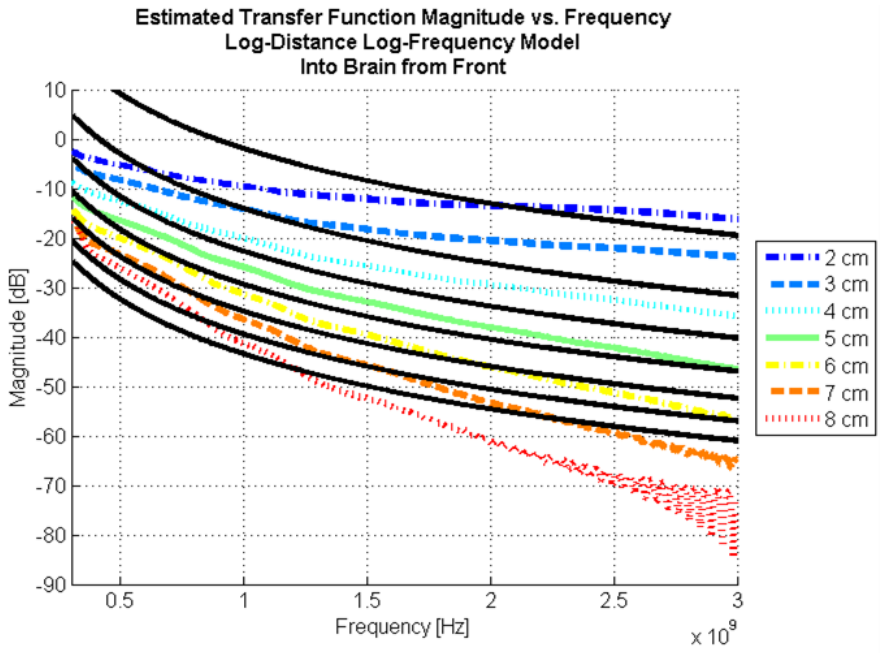

Figure 37: Simulated and Estimated Curves, Indoor Propagation Model

We see, now, that we have curves as opposed to lines. Similar to the simple linear analysis, though, the family of curves is nothing more than shifted versions of itself – there is no distance dependent slope (or frequency dependent slope). This causes a large variance in the error – even larger than that seen by the simplest linear estimator. Results for all the indoor propagation model fittings are seen below in

Table 8: MMSE Variables and Ave Error for Simple Indoor Propagation Model, All Angles

	Front	***Left***	***Back***	***Top***
k	20.0746	23.2829	22.9539	28.9787
n	6.8989	7.6353	7.0706	8.6917
m	3.6656	3.7938	3.7171	4.3187
$\sigma_{error}\ [dB]$	5.039	5.650	5.322	6.853

5.2.3 Modified Indoor Propagation Model

Here we try to slightly modify the indoor propagation model such that we generalize it over frequency and distance without assuming the independence of those variables. This modification is done in a similar manner to that of the modified linear model. We suggest the following equation:

$$\hat{X}(f,d)_{dB} = k\left(\frac{d}{d_0}\right) - n\left[10\left(\frac{f}{f_0}\right)\log_{10}\left(\frac{d}{d_0}\right)\right] - m\left[10\left(\frac{d}{d_0}\right)\log_{10}\left(\frac{f}{f_0}\right)\right] \qquad 42$$

To compare this equation to the indoor propagation model we must get rid of its frequency dependence. This is done if one sets $f = f_0$ in Equation 42. Doing this, we see that it simplifies to the following equation:

$$\hat{X}(f,d)_{dB} = k\left(\frac{d}{d_0}\right) - n\left[10\log_{10}\left(\frac{d}{d_0}\right)\right] \qquad 43$$

Equation 43 is not exactly the indoor propagation model because the initial constant k now depends on the distance, but it is very similar in nature. If one now uses this equation to fit the simulated transfer function data, the following results are obtained:

Table 9: MMSE Variables and Ave Error for Modified Indoor Propagation Model, From Left

k	-2.614
n	0.235
m	1.072
σ_{error}	1.030 dB

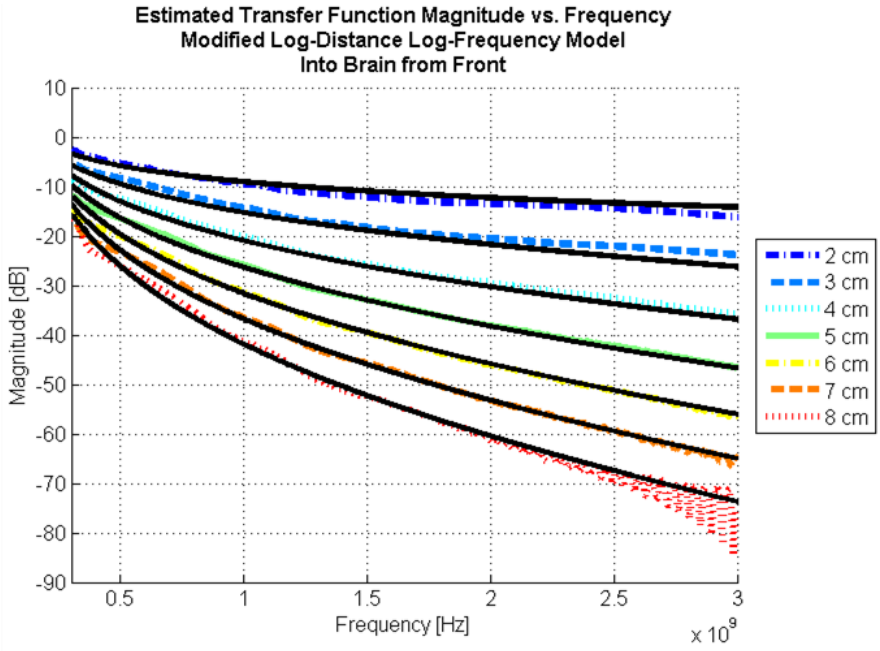

Figure 38: Simulated and Estimated Curves, Modified Indoor Propagation Model

This fit is, clearly, the best of the four fits thus far. It has the lowest error variance and follows the curves well for all values of distance and frequency. Results for the variable values for all the modified indoor propagation model fittings are seen below in *Table 10*. *Figure 39* plots all of the actual transfer functions against the estimated transfer functions.

Table 10: MMSE Variables and Ave Error for Modified Indoor Propagation Model, All Angles

	Front	***Left***	***Back***	***Top***
k	-2.6139	-2.9434	-2.3794	-2.7227
n	0.23515	0.44346	0.43827	0.6164
m	1.0716	0.7979	0.75551	0.73135
$\sigma_{error}\ [dB]$	1.030	1.318	1.294	2.734

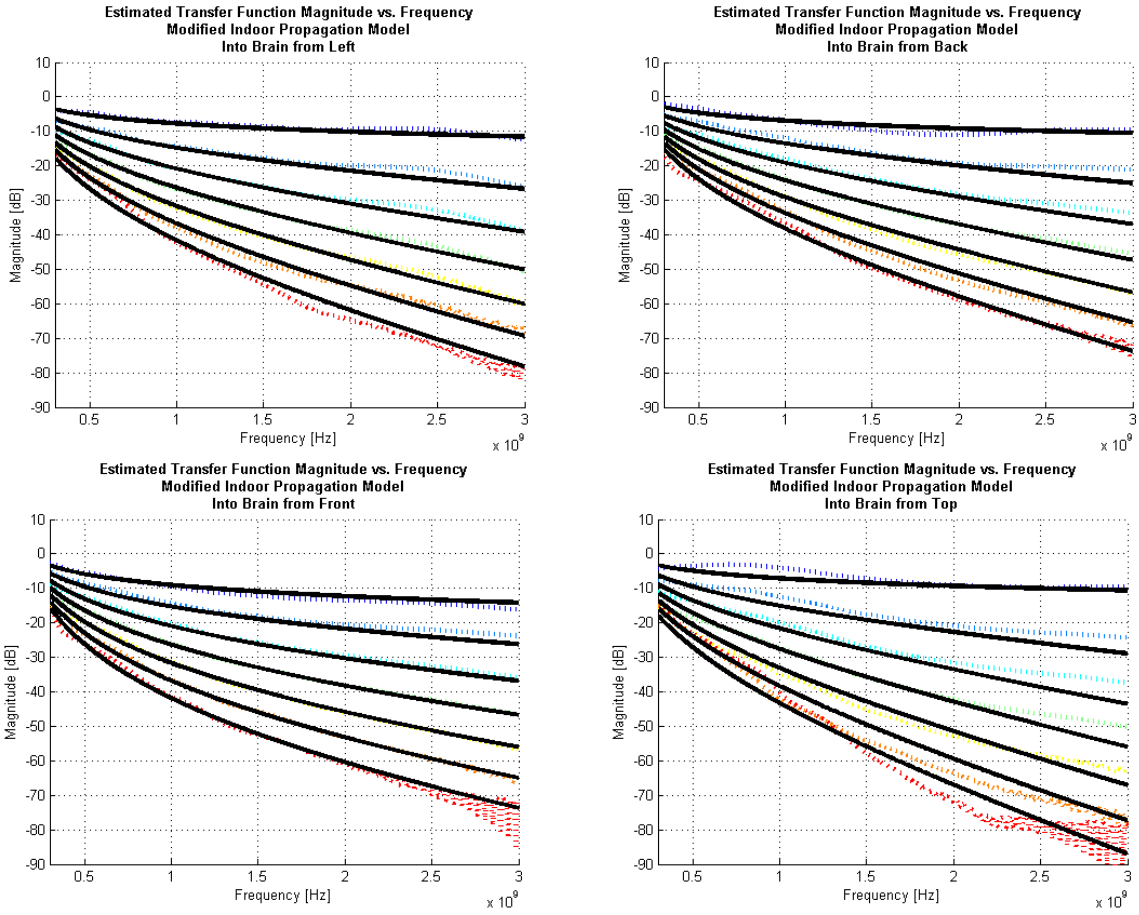

Figure 39: Simulated and Estimated Curves for Modified Indoor Propagation Model, All Angles

5.3 Fitting Multiple Simulations, Final Transfer Function

To finally obtain a complete transfer function for the human head, the minimum mean square estimation was performed on all available data. Equation 42, the modified indoor

propagation model, was used. The final variable values are shown in *Table 11* and the final fit is shown on top of all previous curves.

Table 11: MMSE Variables and Ave Error for Total Modified Indoor Propagation Model

k	-2.6649
n	0.43332
m	0.8391
σ_{error}	2.802 dB

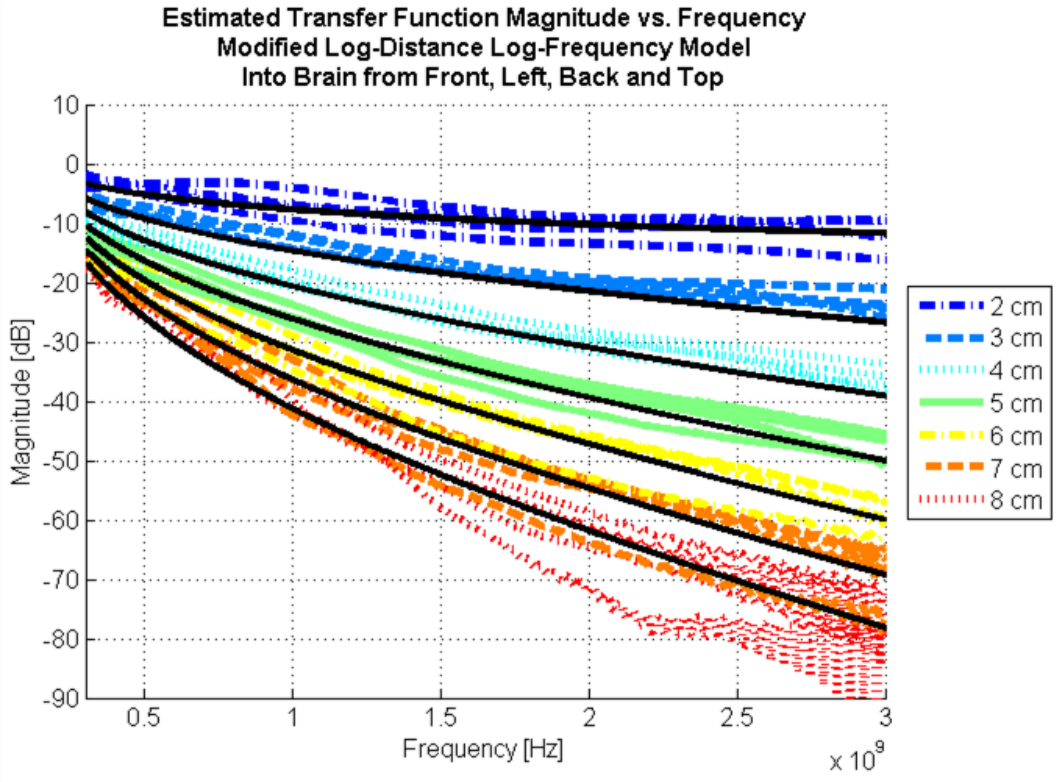

Figure 40: Simulated and Estimated Curves for Total Modified Indoor Propagation Model

Therefore, the final, general equation to describe the transfer function of the human head can be described here:

$$\widehat{X}(f,d)_{dB} = -2.66\left(\frac{d}{d_0}\right) - 0.43\left[10\left(\frac{f}{f_0}\right)\log_{10}\left(\frac{d}{d_0}\right)\right] - 0.84\left[10\left(\frac{d}{d_0}\right)\log_{10}\left(\frac{f}{f_0}\right)\right] \quad (44)$$

for f_0 is 250MHz and d_0 is 2cm.

As seen in *Figure 40*, the model fits the curves well with most of the error being caused by the curves simulated from the top of the head. Even with this source of error – it is, seemingly, only at the extremes of high frequency and deep distance that these curves are substantially off. From our value of σ_{error} we find our two-sigma spread is approximately 5.6dB. This means that approximately 95% of the simulated points are within 5.6dB of our estimate. Overall then, communication to implants in the head seems to be fairly straightforward and predictable with the use of Equation 44. The modified log-distance, log-frequency model is accurate and able to describe the communication model presented by the human head from these four different positions. This model is the first step to designing complex systems to work in this environment.

5.3.1 Model Limitations

Just as important as the model itself are the limitations of the model - knowing where and when it can be used. This model was built off the assumption that the transmit antenna was the external antenna, it was in the far field and its transmitted wave was approximately a plane wave. This means that this model may not be valid for transmission *from* an implanted antenna. Geometrical complexity imposed by the skull may cause other effects not taken into account through the generation of this 'external antenna' transfer function. Therefore, reciprocity may not hold in all cases.

The model was also built off the assumption that the communication occurred perpendicular to the surface of the head. This means that the incoming plane wave is tangent to the head as it enters it. This usually means that the communication is occurring through the smallest amount of tissue. The model also may not hold if this condition is not satisfied.

Testing of the reciprocity of this model is done through attempting to predict the results of simulations for which the internal antenna is the transmitter. This is done for several different simulations and with only limited success. In general, we see this model will be useful for transmission *to* an implanted antenna.

One other limitation, which could eventually become a source of error for this transfer function, is the assumption that the body will not react to the placement of the antenna. The human body is a living medium that will, likely, react. It has been seen that scar tissue, mostly fat, can begin to form around an implanted antenna. This will add a new, separate, layer of tissue around the antenna. This new layer has not been taken into account in this transfer function and, therefore, cannot be approximated. This layer, normally composed of fat, will completely surround the implant. The fat, which has electrical properties as seen below in *Figure 41*, will likely cause an increase in power loss.

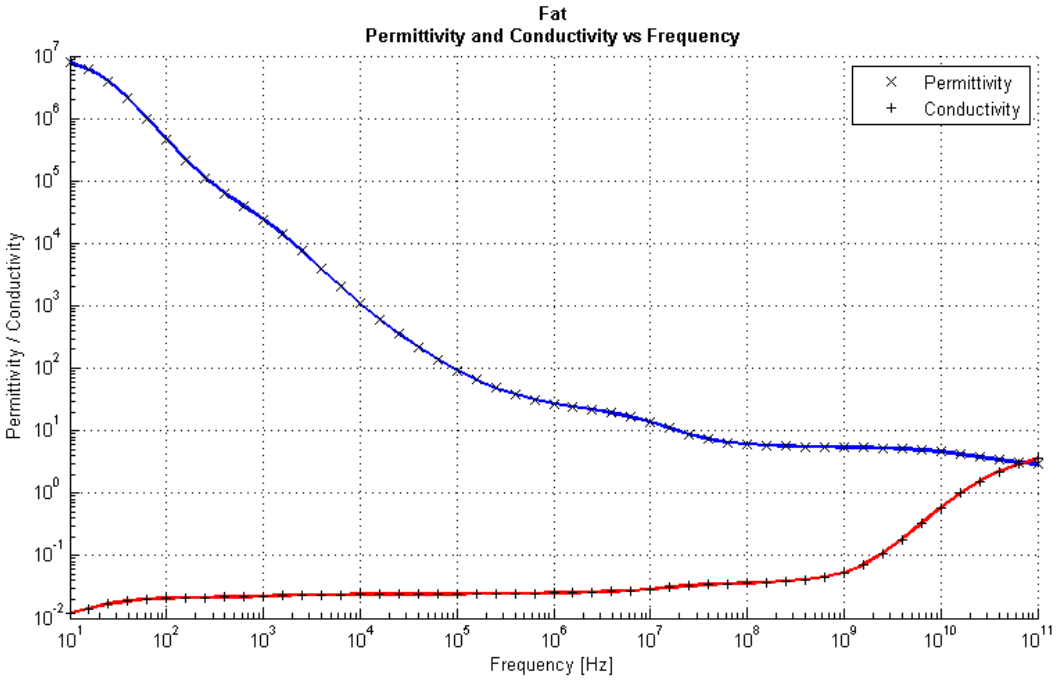

Figure 41: Permittivity and Conductivity of Fat vs. Frequency

Also, it should be noted that this final communication model has been obtained through curve fitting of the obtained data. That is to say, other communication models – which may or may not be of the same general form of this one – could be used to fit the data as well. As an example, a model could take the same form but add another frequency dependent variable, or even a constant. This can be done with simple modifications to the MATLAB functions and scripts attached in Appendix B.

6. Results and Prediction of Received Power Profiles

Now that a wideband characterization for the human head has been obtained for communication *to* an implanted sensor, it is necessary to characterize communication *from* an implanted sensor. The reasons for this are twofold. First, current work has only characterized narrowband communication through a multilayered sphere model of a human head – this work is too simplistic and we seek to expand upon the simulations by using the human body model. Secondly, we look to test the reciprocity of the estimated transfer function that was developed in Chapter 4.

To do this, we look specifically at simulation of power levels that are generated outside the head through the use of simple dipole antennas both inside and outside of the head. Because this type of simulation requires the use of specific antenna types, we are no longer looking at wideband characterizations (the use antennas is inherently narrowband).

To assure that these simulations were being done correctly, initial simulations were done to verify previously published results for a simplified model [24]. All of this work was done for dipoles tuned to approximately 400MHz.

6.1 Spherical Head Model

Kim and Rahmat-Samii have previously simulated a communication link that is established between a cranially implanted dipole antenna and an external dipole receive antenna [24]. The model that was used for the human head, in this case, was a simplified model made of six concentric spheres that were assigned the electrical properties of six different human tissues at the single frequency of 402MHz. The model used by Kim and Rahmat-Samii is shown below in *Figure 42* and the electrical properties that were assigned to the tissues are seen in *Table 12*.

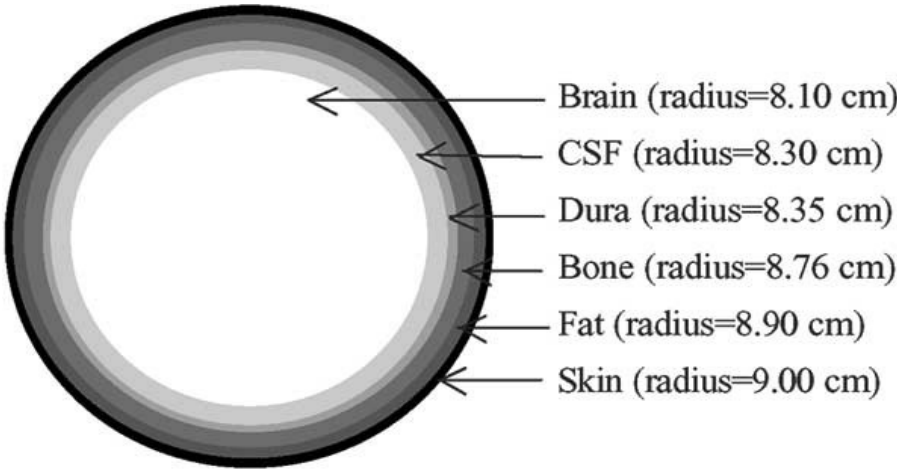

Figure 42: Spherical Six-Layered Head Model Used by Kim and Rahmat-Samii

Table 12: Electrical Data of Biological Tissues Used by Kim and Rahmat-Samii

	$Permittivity$ (ε_r)	$Conductivity$ $(\sigma, S/m)$
Brain	49.7	0.59
Cerebro Spinal Fluid	71.0	2.25
Dura	46.7	0.83
Bone	13.4	0.09
Fat	11.6	0.08
Skin	46.7	0.69

Next, two half-wavelength dipole antennas were designed to resonate at approximately 400MHz; one inside the head, and one outside of the head. Equations to design these antennas are well known and can be found in textbooks [55]. The inner dipole, because it is surrounded by a dielectric of approximately 50, is designed to be a half-dielectric-wavelength antenna. This translates to a dipole length of approximately 5.25cm.

This antenna was then placed inside the head at two different locations. The first location places the inner dipole directly in the center of the model and the second location then moves the

inner dipole 4.5cm towards the receiving antenna. For each of these simulations, the outer dipole is moved from 1m to 5m away. Results of the power levels obtained at the receive antenna were then plotted and compared to the results for two 400MHz dipoles communicating in free space. Kim and Rahmat-Samii's plot can be seen below in *Figure 43*.

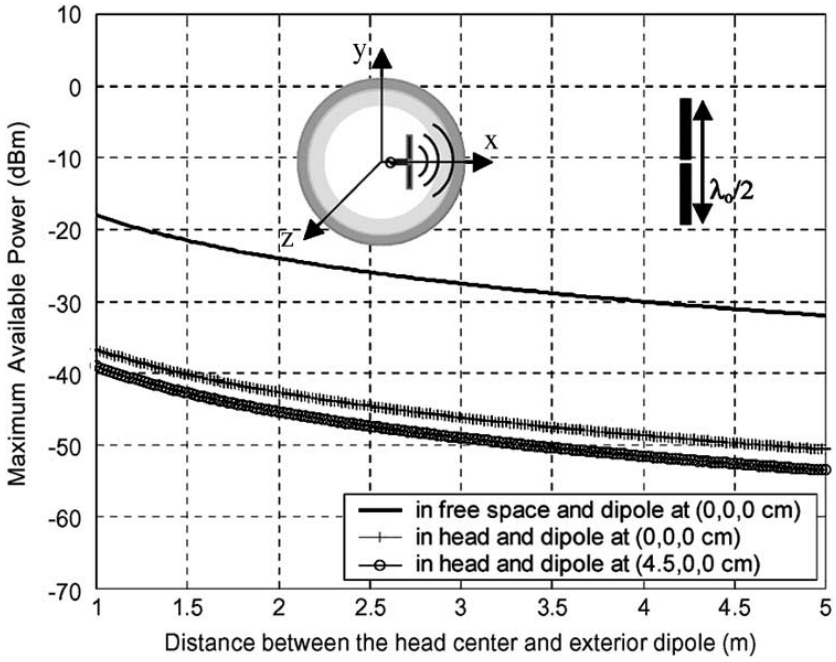

Figure 43: Maximum Available Power Obtained at an Exterior Dipole Antenna from an Internally Implanted Dipole

It should be noted that the maximum available power at the receiver is in units of dBm – which is referenced to a mW. The formula for the maximum available power is seen below:

$$P_{max} = S_{rec} A_{em} = S_{rec} \frac{\lambda^2}{4\pi} D_m \qquad 45$$

where S_{rec} is the power density at the receiving antenna (W/m^2), A_{em} is the maximum effective aperture of the receiving antenna (m^2), λ is wavelength of the incoming wave and D_m is the maximum directivity of the receive antenna. Their value was adjusted, however, such that the total power that the transmitting dipole delivered was 1.84mW. This adjustment was done to

make sure that the maximum Equivalent Isotropically Radiated Power (EIRP) limitations for an internally implanted dipole antenna ($25\mu W$ in free space) were met.

The results obtained by Kim and Rahmat-Samii show a worst-case receive sensitivity of approximately -55dBm at a distance of 5m. Their results also show that moving the implanted antenna closer to the external antenna actually decreased the power obtained there. This was caused by a smaller radiated power from the offset inner dipole [24].

6.1.1 Verification of Spherical Head Model Results

To verify these results, the dipole antennas had to be designed, the appropriate farfield parameters had to be calculated, then the final simulations had to be set up and the plots compared. This work is seen below.

The design of the outer dipole was done and the results and appropriate simulated values are shown below:

Table 13: External Dipole Dimensions, Variables

$Variable$	$Value$	$Description$
$lambda$	$67.22935cm$	$Wavelength$
d	$0.025\ lambda$	$Length\ of\ Discrete\ Element$
$l2$	$0.5\ lambda$	$Dipole\ Length$
r	$0.003369\ lambda$	$Wire\ Radius$

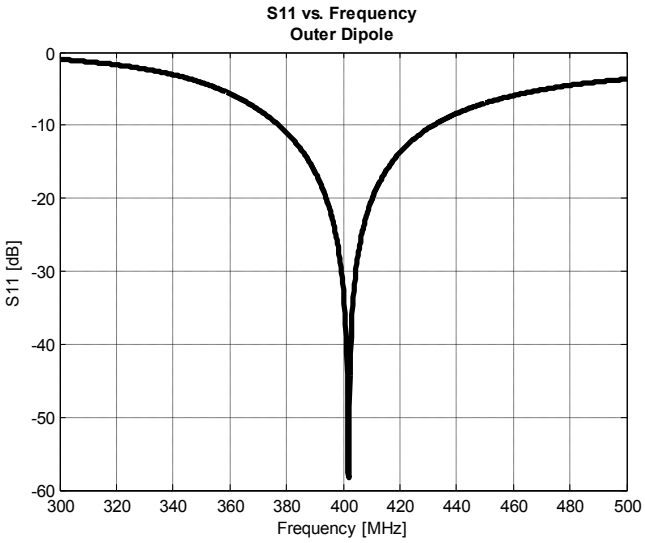

Figure 44: Return Loss Plot, External Dipole

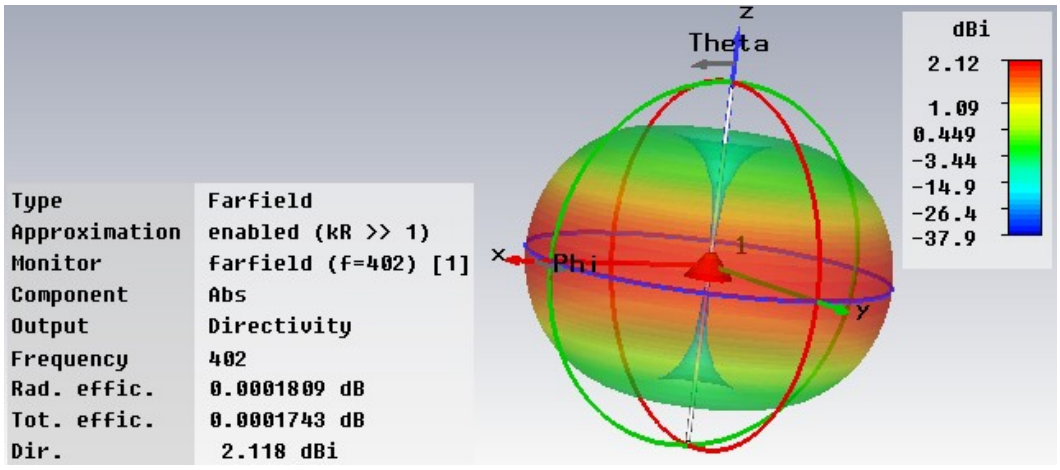

Figure 45: External Dipole, Radiation Pattern, Simulated Farfield Parameters

Similarly, the internal dipole was designed. The use of CST allowed for the optimization of the length of the dipole while inside the spherical model. Results for the matching and the variable values are shown below:

Table 14: Internal Dipole Dimensions, Variables

Variable	*Value*	*Description*
lambda	8.8306*cm*	*Wavelength*
d	0.025 *lambda*	*Length of Discrete Element*
l2	0.5 *lambda*	*Dipole Length*
r	0.003369 *lambda*	*Wire Radius*

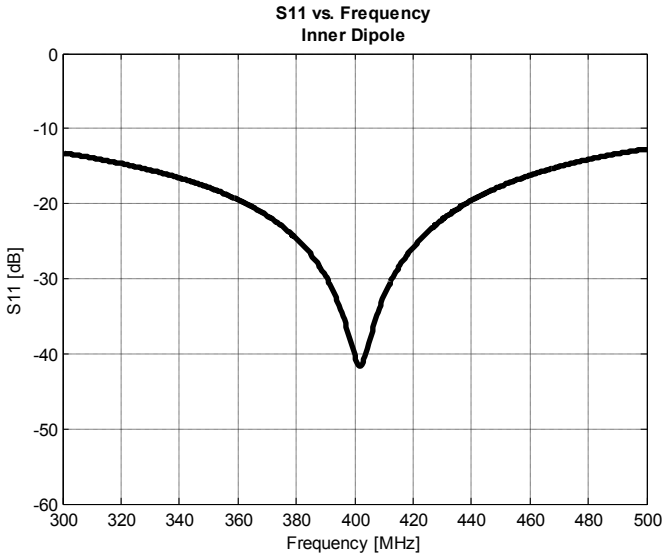

Figure 46: Return Loss Plot, Internal Dipole

Once the antennas were designed, the communication link simulations were then set up and run. A screen capture of one of these simulations is shown here:

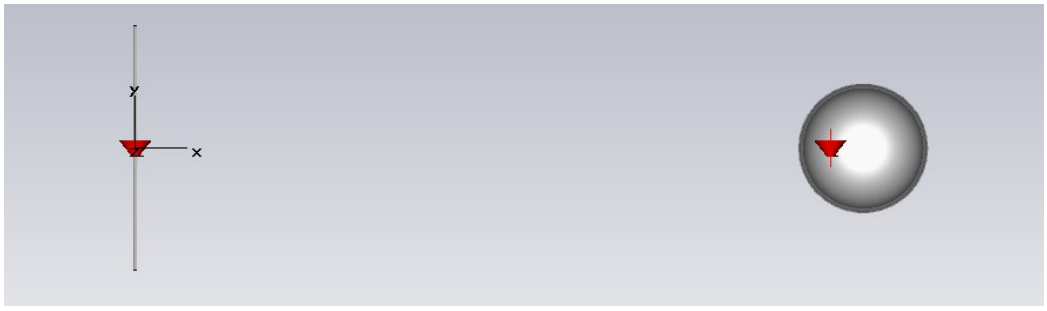

Figure 47: Communication Link Simulation, Distance From External Dipole to Center, 1m

Post-processing was then done to calculate the maximum available power at the receiver. To do this in CST, field monitors were set to record the electric and magnetic fields at 402MHz. These were then combined using Equation 21 to obtain the three dimensional Poynting vector field (W/m^2). This was plotted along the line that passed through both dipole antennas and the maximum value was obtained. The formula used to plot the final results in dB is seen below:

$$P_{max} = 10\log_{10}[S_{rec}A_{em}] - 27.352dB \quad (46)$$

where

$$A_{em} = \frac{\lambda^2}{4\pi}D_m = 0.0722 \quad (47)$$

as calculated by the directivity value of the external antenna found in *Figure 45*. The factor of $27.352dB$ that is subtracted from the power in Equation 46, is the adjustment for the assumption that only 1.84mW is delivered by the transmitting antenna. CST assumes a value of 1W is delivered. Taking the difference between 1W and 1.84mW in dB gives the value of $-27.352dB$.

Before displaying the results, however, it should be noted that the simulations done in this work and the simulations done by Kim and Rahmat-Samii are most likely slightly different. The antennas that were designed and simulated by Kim and Rahmat-Samii were only vaguely described and, therefore, the antennas designed in this paper may be not matched exactly as theirs were. Because of this vagueness in description, this paper attempted to design the best matched dipoles using optimization techniques and it is likely that the antenna designs seen in *Figure 44* and *Figure 46* by this paper are at least as well matched as those used by Kim and Rahmat-Samii. This would mean that it is possible that more power may be delivered at the receive antennas compared to the results from Kim and Rahmat-Samii. This change in absolute power values is irrelevant, however, as it is the relative values between the two simulations that is the most important to verify the results.

The results of the three simulations can be seen below in *Figure 48*. As expected, the results do not match up exactly with Kim and Rahmat-Samii's work, but the overall match is acceptable. The trend of the curves are similar and the DC offset seen for the bottom two curves is small. It is important to note that the same peculiar result – of lower power seen at the receiver with an offset transmitter – is confirmed by these simulations.

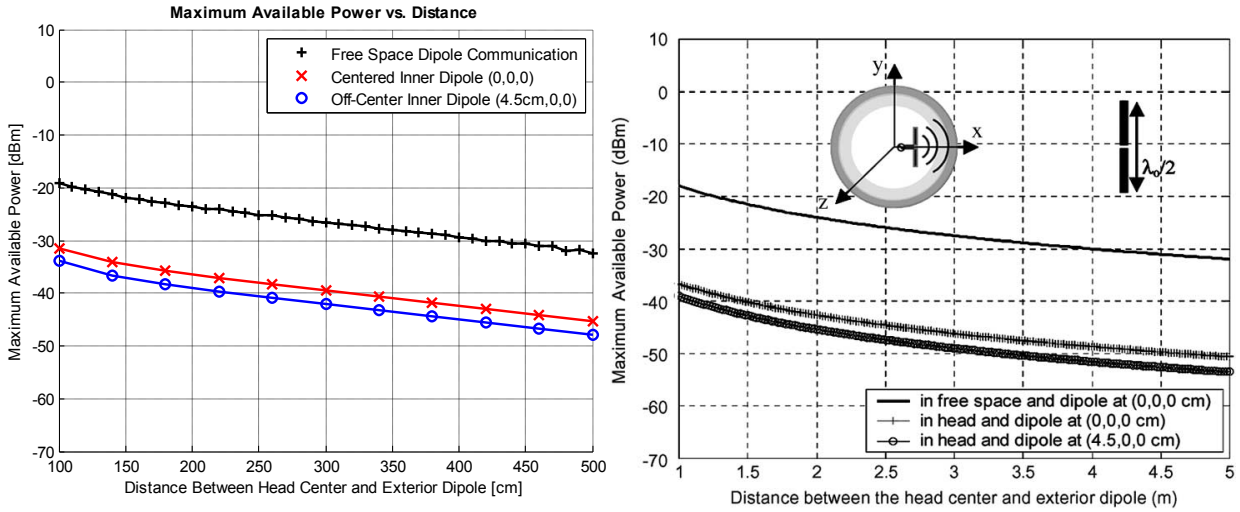

Figure 48: Communication Link Simulation, Distance From External Dipole to Center, 1m. Comparison to Results from Kim and Rahmat-Samii

Again, the differences seen in the results can be explained by different dipole designs caused by vague descriptions in the design of the dipoles used. Regardless of these differences, the results show that the relative difference between the bottom two curves for both the simulations for this paper and those done by Kim and Rahmat-Samii's, are equal. This confirms the correct techniques are being employed and the simulated results are accurate enough such that we can consider the simplified model results to be verified.

6.2 Human Head Model with Frequency Dependent Electrical Characteristics

6.2.1 Differences Between Spherical Model and Human Head Model

To extend the work by Kim and Rahmat-Samii the multilayered spherical model was replaced with the human body model's head. This model, with all of its geometrical and electrical complexities, will more accurately represent the human head in simulation. However, when we look closely, the geometry is not the only difference between the two models, the electrical characteristics of the tissues have also changed.

We now take a closer look at the complex permittivity of brain tissue as defined by both models. Kim and Rahmat-Samii provide a table of electrical characteristics that were used for their simulations. These electrical characteristics were not frequency dependent, but valid only for the antenna design frequency of 402MHz. Part of this table has been reproduced below, brain tissue is in bold text.

Table 15: Electrical Data of Biological Tissues Used in Kim and Rahmat-Samii's Spherical Head Simulations at 402MHz

Biological Tissue	*Permittivity* ε_r	*Conductivity* $(\sigma, S/m)$
Brain	**49.7**	**0.59**
Cerebro Spinal Fluid	71.0	2.25
Dura	46.7	0.83
Bone	13.1	0.09

These tissue properties were compiled by Yale University School of Medicine and correspond to the following plots for ε' and ε'' (as provided by the CST MWS software):

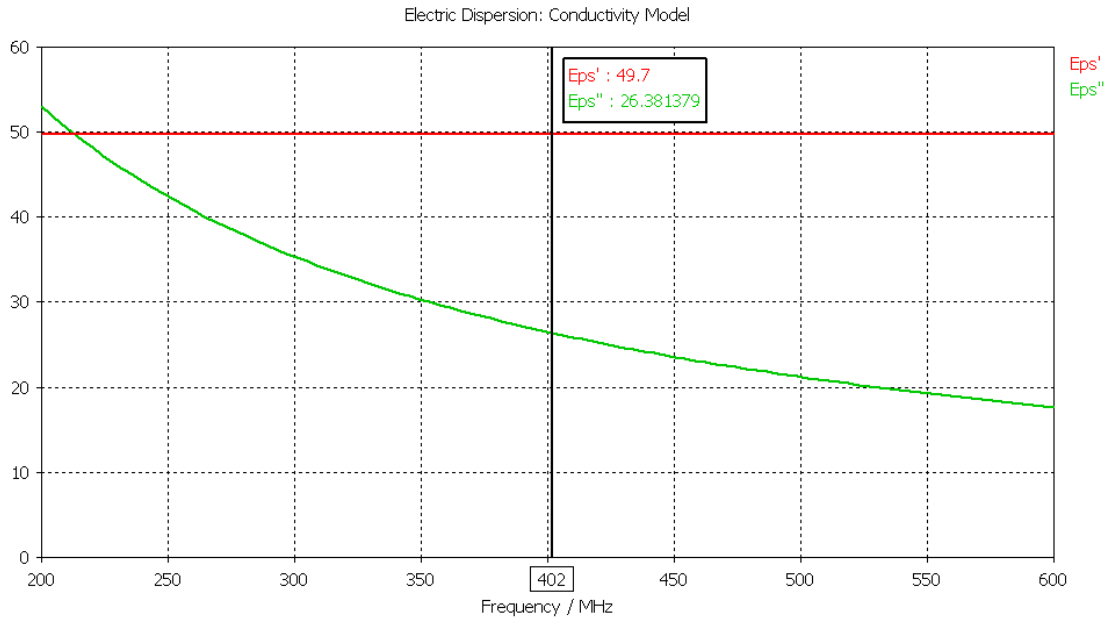

Figure 49: ε' and ε'' for Brain, as defined in Kim and Rahmat-Samii's Paper

Note that conductivity translates to ε'' through the following equation:

$$\varepsilon'' = \frac{\sigma}{2\pi f \varepsilon_0} = \frac{0.59}{2\pi(402e6)\varepsilon_0} = 26.381379 \qquad 48$$

The values of ε' and ε'' for the brain as defined by the human body model provided by the Ansoft Corporation are slightly different. Not only because the characteristics were taken from results compiled by Gabriel et. al. in their three paper series [1]–[3] (a different source) but because the electrical properties of the brain for the Ansoft model were created by averaging characteristics of the two types of matter in the brain; both white matter and grey matter. These characteristics can be seen below in *Figure 50*.

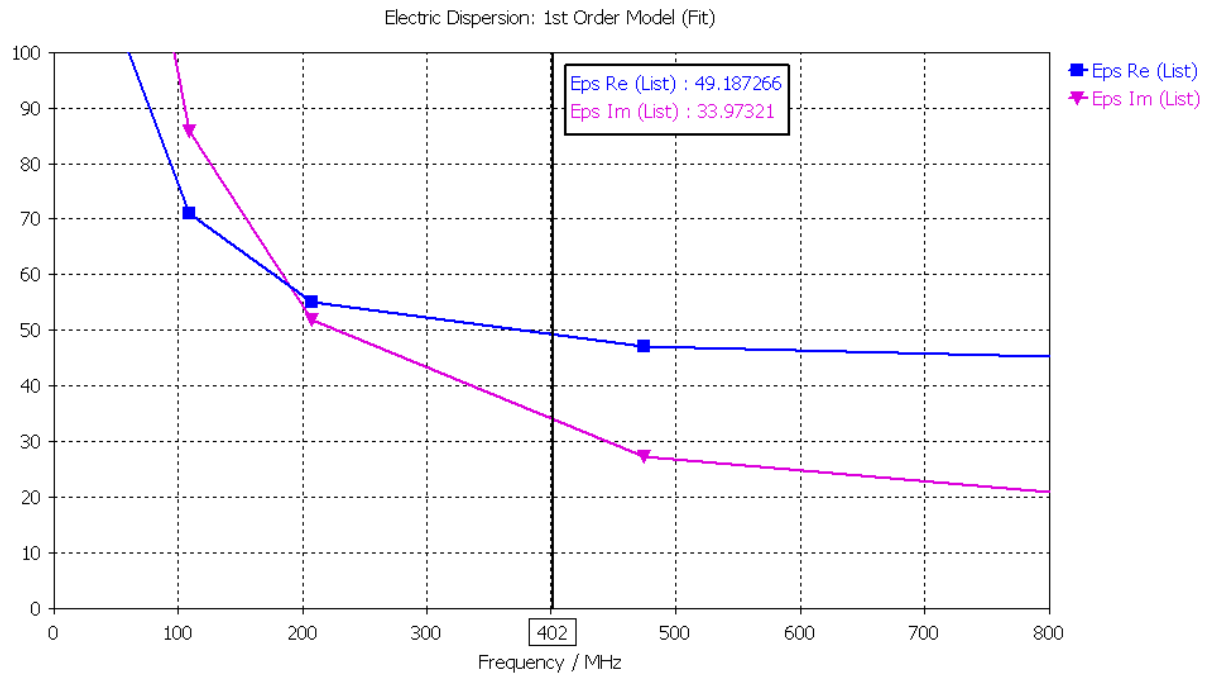

Figure 50: ε' and ε'' for Brain, as defined by Ansoft Corporation's Human Body Model

The ε' values for both models are quite similar at 400MHz, but when calculating the conductivity value from the ε'' value in *Figure 50* we find that $\sigma_{Human\ Body\ Model} = 0.7598\ [S/m]$. This is a 20% increase in conductivity. Because of this increase in conductivity, we expect to see much higher losses when using the human body model, as compared to the multilayered sphere model. Some of these losses, however, may be caused by geometry. To help separate out the losses caused by the differences in electrical characteristics with those caused by the differences in geometry, two separate simulations will be done. In the first, the human body model's geometry will be used with the human body model's electrical characteristics. Then, the human body model's geometry will be simulated with the electrical characteristics as used by Kim and Rahmat-Samii. This then allows us to say that the only difference between the two

simulations lies in the geometry of the model. The results from these simulations can be compared and conclusions can be drawn.

6.2.2 Human Head Model Setup

The following simulations, as has been stated before, will use the human head model. Below, in *Figure 51*, we see the dimensions of the model that were used. The center of the head is still located 6.5cm below the top-most point on the head, but part of the neck and shoulders have been cut out to reduce simulation time. Only the top 26.5cm were kept for these simulations. All objects below this point were deleted.

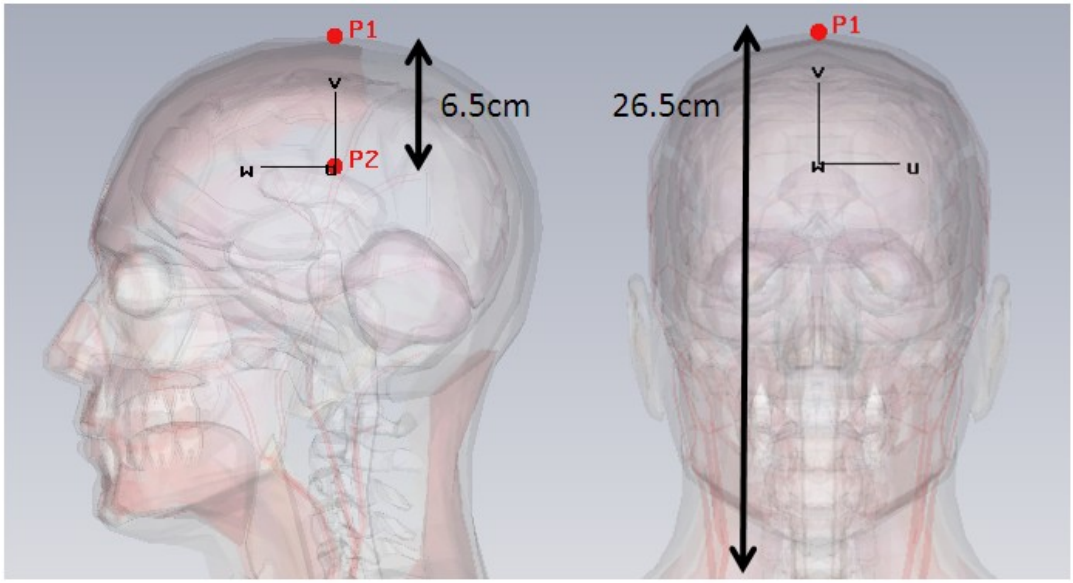

Figure 51: General Dimensions of the Human Body Model for Antenna Simulations

6.2.3 Received Power from Implanted Antenna, Varying Distance

6.2.3.1 Simulation Setup

The first series of simulations that were done investigated a dependence on distance. Basically, the simplified spherical model for the head was replaced with the more accurate human body model head. This, of course, means that the setup for this simulation was exactly the

same as the setup that was used previously to verify the simple spherical model's results. Simple illustrations of these setups are shown below in *Figure 52* and *Figure 53*. As can be seen, the inner dipole is placed either at the center of the head, as in *Figure 52*, or moved a distance of 4.5cm from the center of the head towards the external dipole, as seen in *Figure 53*. This is exactly what was done in the spherical model simulations. For both the centered and off-center dipoles it is set such that the distance d is defined as the distance from the center of the head to the external dipole.

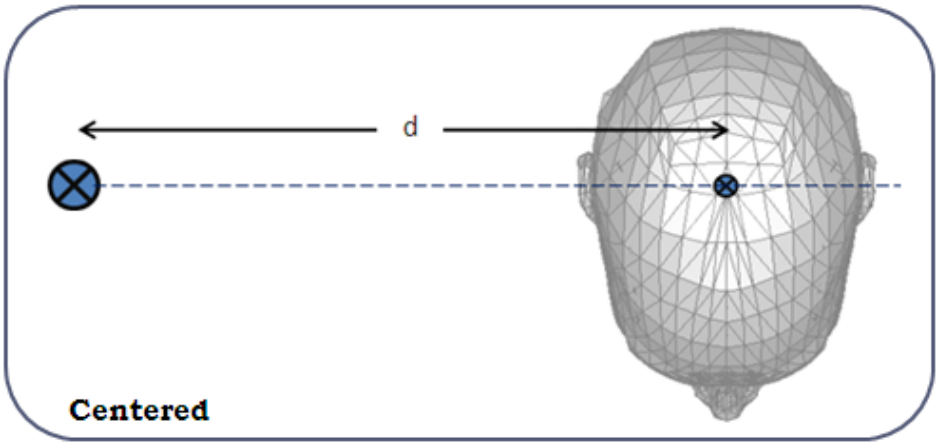

Figure 52: General Setup of Distance Power Level Simulation with Centered Inner Dipole

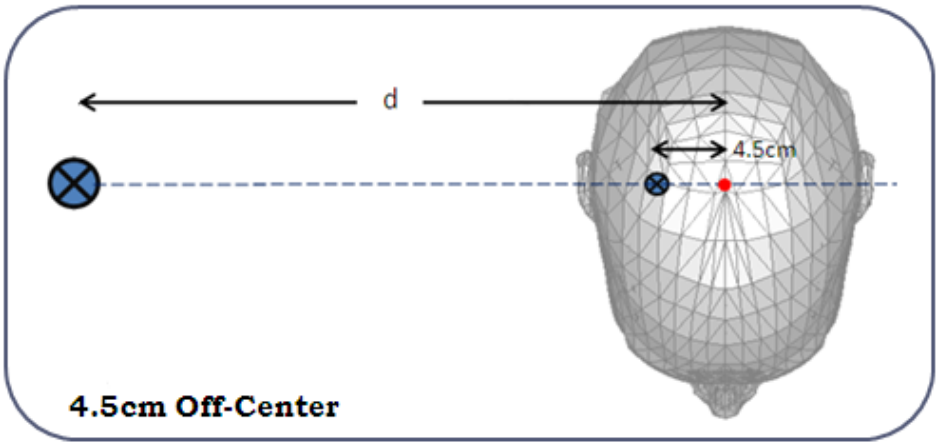

Figure 53: General Setup of Distance Power Level Simulation with Off-Center Inner Dipole

Only one decision had to be made to finish the setup of these simulations. This was an assumption of the angle at which angle the dipole communication would occur. The spherical model, by virtue of being spherical, is symmetrical. Therefore, all orientations could possibly represent any part of the head (the face, the right side, the top, the back, etc.). Kim and Rahmat-Samii's paper did not mention any specific orientation, so it was decided that for direct comparison to the spherical model, the dipole communication would take place through the side of the head (as shown). This orientation was chosen because it provided the closest match to the conditions in the spherical model: the spherical model had a constant radius of 9 cm and the points on the sides of the head are at a distance of 8.5 cm from the center.

6.2.3.2 Simulation Results

The location of the two dipoles, as seen in *Figure 52* and *Figure 53* mimic those of the original simplified spherical model – a centered inner dipole and an inner dipole that is moved 4.5cm from the center towards the external dipole. The results from running these simulations are shown below in *Figure 54*. These results are shown directly next to the results from Kim and Rahmat-Samii for an easy comparison.

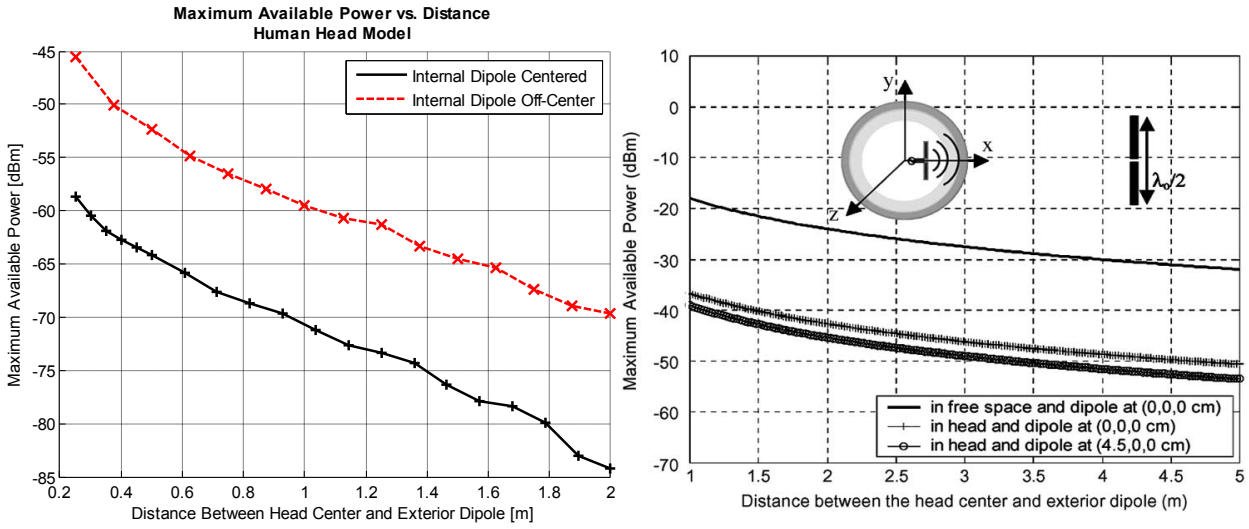

Figure 54: Maximum Available Power vs. Distance, Human Head Model, Centered and Off-Centered Inner Dipole. Comparison vs. Kim and Rahmat-Samii's Simplified Model.

It should first be noted that these two simulations were not done over the exact distance ranges as those of Kim and Rahmat-Samii. The human head model simulations were done at shorter distances but overlap the simple model in the region where d ranges from 1 to 2m. This was done because of the size and complexities in the model increased simulation times too much for distances over 2 meters.

When comparing the results to the results of Kim and Rahmat-Samii, we see many differences; two of which are glaring. The first difference is that the peculiar result (where power received at the external antenna was actually less for the off-center dipole than for the centered dipole) was not obtained. In fact, the off-center dipole generated approximately 12.1dB more power at the receive antenna.

The second difference, which is noticed upon inspection, is that the losses for the human head model are *much* greater than those seen in the simplified spherical model. In fact, if one

compares the centered dipole curves for the human head model and the spherical model, at the 1m mark we see that there is a difference of 34dBm; more specifically, the spherical model has a value of -37dBm while the human head model has a value of -71dBm. This loss, however, was expected because of the increased conductivity of the human body model's head.

The last major difference is seen in the rate of the power decrease. For the simple spherical model there is only a 5dB decrease in power as distance was increased from 1 meter to 2 meters – over the same distances, the power from the human head simulations decreased, on average, 13dB. This shows that the rate of power loss has increased through the use of the human head model.

Another simulation was done to see if the losses caused by the geometry of the head could be separated from the losses caused by the difference in electrical characteristics. For this simulation the geometry of the human body model's head was used, but the electrical characteristics of the brain were changed to equal that of the multilayered sphere simulations. The results of both simulations, for a centered dipole, are shown below in *Figure 55*: on the left half of we see a comparison between the results for a centered inner dipole with the body model permittivity and the spherical model permittivity and on the right side we see the results from Kim and Rahmat-Samii's simulations, for an easy comparison.

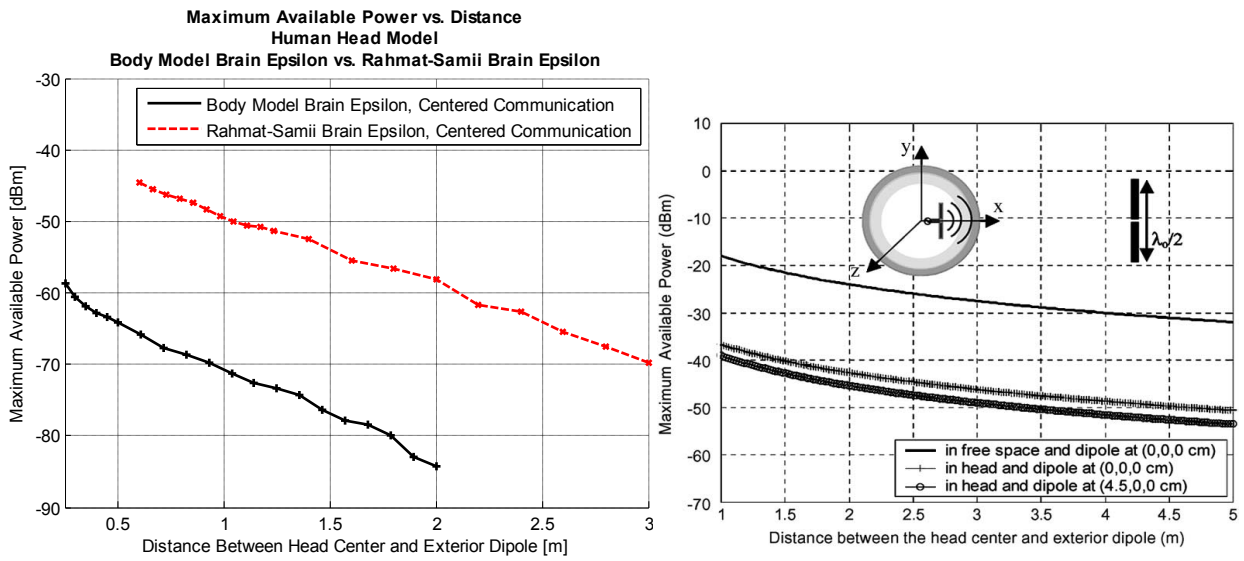

Figure 55: Maximum Available Power vs. Distance, Centered Internal Dipoles for Human Head Model with both Body Model Brain Epsilon and the Simpler Kim and Rahmat-Samii Brain Epsilon, Comparison vs. Kim and Rahmat-Samii's Simplified Model.

Regarding the left half of the figure, two notes should be made. First, the use of the permittivity used in the spherical model (which had a comparatively lower conductivity) resulted, as one would expect, in an increase of power seen at the receiver; quantitatively, there was a 22dB increase compared to the human body model. Second, the overall trend of the data on the left has not changed – the two plots seem to be just DC offsets from each other. This means that the change in permittivity did not cause the acceleration in power loss that is seen in the human body model results.

Making these notes and comparing the left and right sides of *Figure 55*, we can make conclusions regarding what the geometry of the head does to the power levels obtained at the receiver; namely that the geometry alone causes a minimum of 12dB of attenuation after

distances greater than or equal to 1 meter and the geometry tends to accelerate the loss of power as the external antenna distance is increased.

6.2.4 Received Power from Implanted Antenna Varying Communication Angle

The second type of simulation that was done investigated the rotational dependence of the external antenna for both centered and off-center internal dipoles. Unlike the spherical model, the physical human head model is not symmetrical. This asymmetry will cause the received power to exhibit some sort of rotational power dependence. This second set of simulations investigates the nature of this dependence for both a centered and 4.5cm off-center implanted dipole antenna. The centered dipole antenna was simulated first at two discrete distances of: $d = 25cm$ and $d = 50cm$, and then the off-center dipole was simulated at a distance of $d = 50cm$.

6.2.4.1 Centered Simulation Setup

Figure 56, below, shows the general setup for the rotational dependence simulation with a centered inner dipole.

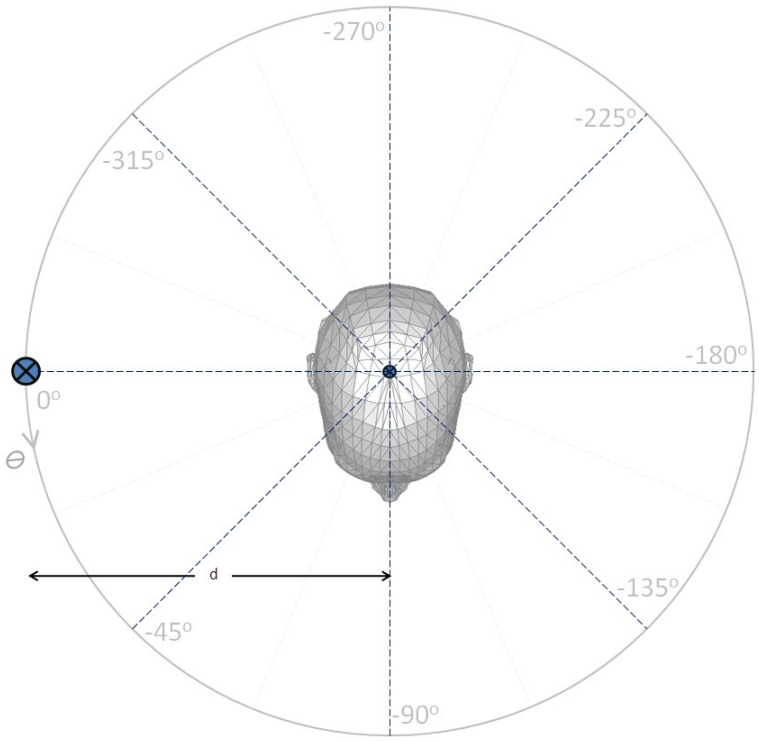

Figure 56: General Setup of Rotational Power Level Simulation with Centered Inner Dipole

In this figure we see that the inner and outer dipoles are denoted by the x-marked locations. We also find that the distance d is defined as the distance from the center of the head to the external dipole. For this simulation the variable θ is varied in increments of fifteen degrees and simulations were completed for two distances of the variable d; namely 25cm and 50cm.

As opposed to what may be assumed from *Figure 56* the actual simulations were set up such that the head and internal antenna were rotating while the dipole stayed in the same location. This was done to ease the post-processing and allow easier plotting in CST. This method, however, is harder to represent visually and it is easier to think of it as the dipole rotating around the head at a constant distance d, as shown above. The dotted blue lines in this figure emanates from inner dipole and extend outwards and intersect the circle of radius d at each different angle of θ. These lines show the most direct communication path from the location

of the internal dipole to the external dipole but may not necessarily show the exact path taken by the electromagnetic wave.

6.2.4.2 Centered Simulation Results

Simulated results for both distances with the centered inner dipole are shown below in *Figure 57*. The overall trend that one would predict based on line-of-sight communication is present: the two sides of the head, located at 0 and 180 degrees, have the least tissue to travel though and should therefore have the highest power level, the front of the head travels though the most tissue and should therefore have the lowest power level, the back of the head should be somewhere in between the side and the front, and all the other angles should work to gradually, and continuously link it all together.

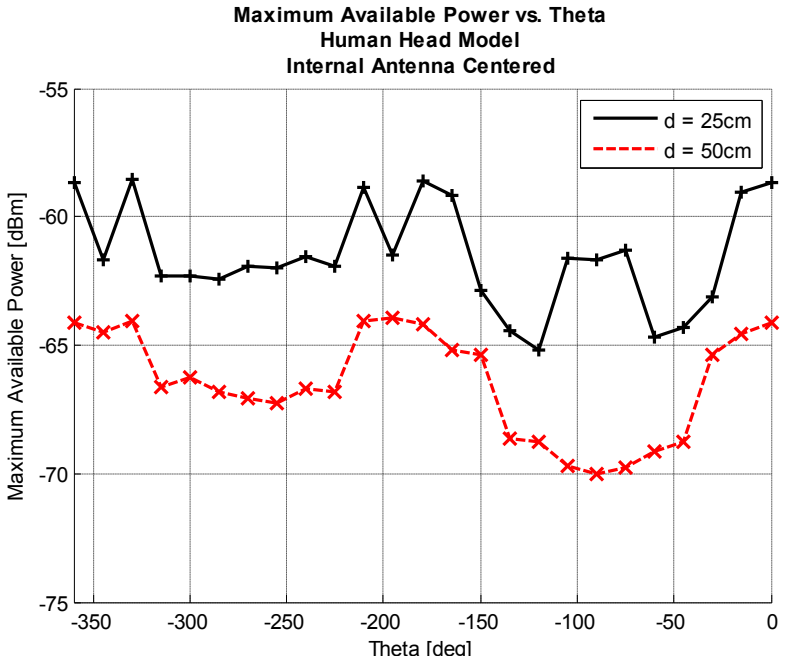

Figure 57: Maximum Available Power vs. Angle, Human Head Model, Centered, d = 25, 50cm

We do see some problems, however, with our results at $d = 25\ cm$. The same general trend seems to be present, and because the external antenna is 25cm closer there is more power,

but there are sudden spikes of up to 3dB better or worse performance in specific regions/value of θ. This may be caused by possible near-field effects and is briefly investigated later in this paper.

6.2.4.3 Off-Center Simulation Setup

Figure 58, below, shows the similar setup for the off-center rotational simulations.

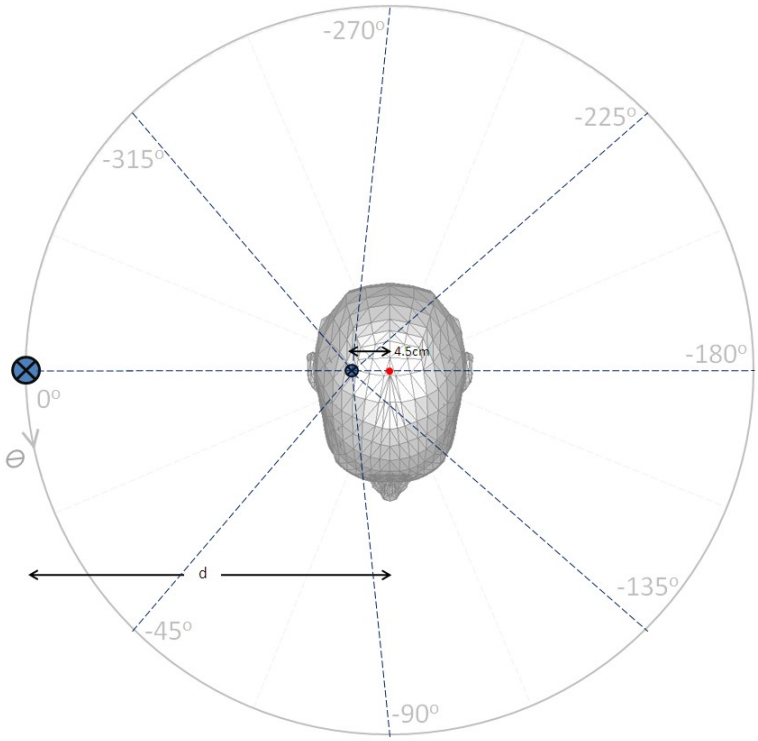

Figure 58: General Setup of Rotational Power Level Simulation with Off-Center Inner Dipole

Again, in this figure, the inner and outer dipoles are denoted by the x-marked locations. Note that the definition of distance d has remained the same for both the centered and off-centered simulations – it is the distance from the center of the head to the external dipole. Again, for this simulation θ is varied in increments of fifteen degrees. Similar to the centered dipole

setup figure, the dotted blue lines emanate from inner dipole and extend outwards and intersect the circle of radius d at each different angle of θ and these lines show the most direct communication path from the location of the internal dipole to the external dipole but may not necessarily show the exact path taken by the electromagnetic wave. It should also be mentioned that this simulation was only done for a single distance of the variable d; namely 50 cm.

6.2.4.4 Off-Center Simulation Results

Simulated results for the off-center dipole antenna at a distance of $d = 50\ cm$ are shown below in *Figure 59*. Superimposed on this figure are also the results for the centered dipole antenna at a distance of $d = 50\ cm$, for an easy comparison.

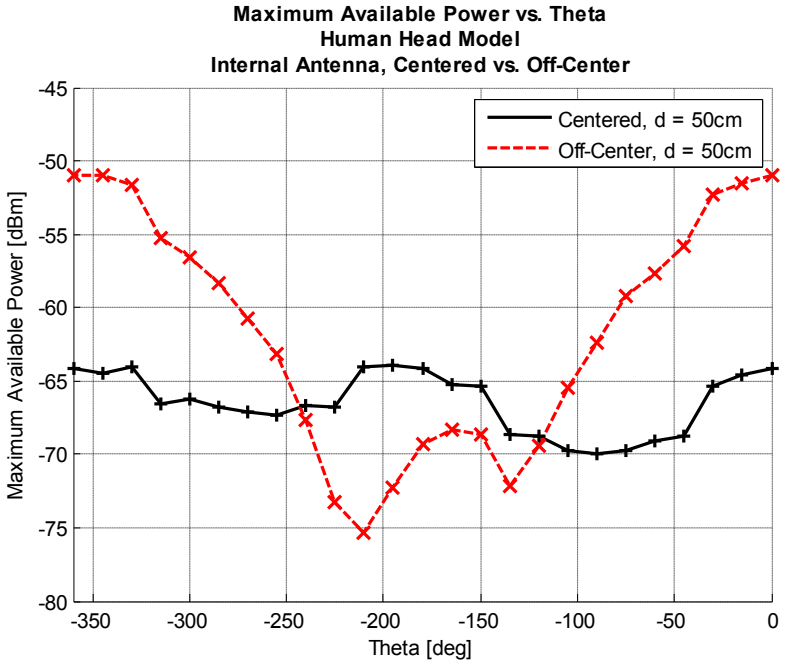

Figure 59: Maximum Available Power vs. Angle, Human Head Model, Centered vs. Off-Center, d = 50cm

As would be expected, the highest power level is greater than that of the centered simulation – after all, the dipole is a full 4.5 cm closer to the side of the head at this point. As we

travel around towards the front and back of the head, the intuitive decline in power is realized but what we see at the opposite side of the head is surprising; namely a small hump of seemingly inexplicable extra power – there is a local maximum in the region at the direct opposite side of the head.

What causes this local maximum is unknown, and is out of the scope of this work to investigate, but we can hypothesize that this hump could be attributed to effects of creeping waves that travel around the outside of the skull. These creeping waves, which have been shown to be the main propagation method of EM waves for on-body antennas [39], may present themselves when the implanted antenna is offset, and therefore closer to the skull. This creeping wave, if it exists, may somehow cause an increase in power seen at the receiver on the other side of the head. This is, however, only a hypothesis and will not be thoroughly tested in the paper.

6.2.5 Received Power Prediction using Modified Log-Distance Log-Frequency Model

6.2.5.1 Methodology for Prediction

The final transfer function obtained for communication through the head, seen in Equation 44, was obtained through the assumption that the transmit wave was approximately a plane wave (in the far field) and that the communication would occur perpendicular to the head. It is important, then, to only attempt prediction at points that satisfy these assumptions. These points change depending on the simulations that are being attempted. For any centered dipole simulation, as long as the external dipole is in the far field – greater than 50cm away, it seems – communication will be perpendicular through the head for four locations: the right, the front, the left and the back at $\theta = 0°, -90°, -180°, -270°$, respectively. For any off-center dipole simulation perpendicular communication only holds for the two sides of the head at $\theta = 0°, -180°$.

The actual prediction is made through the use of the final modified log-distance, log-frequency transfer function seen in Equation 44. These dipoles are designed to communicate at ~400MHz so if one plots Equation 44 vs. d for an f of 400MHz, you get a plot that describes how much loss an electromagnetic wave with a frequency of 400MHz experiences as it travels through varying amounts of tissue. Because the final equation does not assume any sort of antenna, it does not account for any antenna mismatch – therefore absolute value of loss cannot be obtained. However, *relative* losses should remain the same. Therefore, the actual prediction is obtained by subtracting two loss values obtained from the plot at two different depths. These depth values correspond to the two amounts of tissue between the internal and external antennas by line-of-sight. For example, if one wanted to predict the difference between the power levels at the side of the head and the front of the head for a centered dipole antenna, just mark 8.5cm (amount of tissue that the wave travels through when communicating though the side of the head) and 11.25cm (amount of tissue that the wave travels through when communicating through the front of the head) on the plot and read the difference between them; this value should match the simulated difference.

6.2.5.2 Prediction Results Varying Distance

To begin, we attempt to predict the results of the distance simulation. Our simulated results, replotted in below in *Figure 60*, shows that there is an approximately constant difference of 12.1dB between the centered and off-center internal dipoles; the off-center dipole has the greater power. *Figure 61* then shows the difference between the centered and off-center dipoles in terms of the amount of tissue that the electromagnetic wave will pass through – 4.0cm for the off-centered dipole and 8.5cm for the centered dipole. These two points are then marked on the

plot of Equation 44's estimate and the difference between them is taken. We can see from *Figure 62*, below, that our prediction of +12.12dB matches the simulated results quite well.

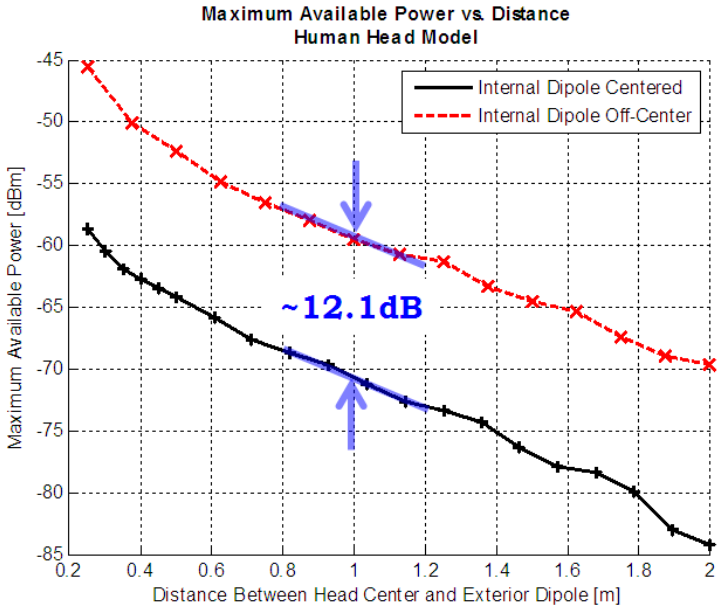

Figure 60: Maximum Available Power vs. Distance, Human Head Model, Centered and Off-Centered Inner Dipoles, Replotted

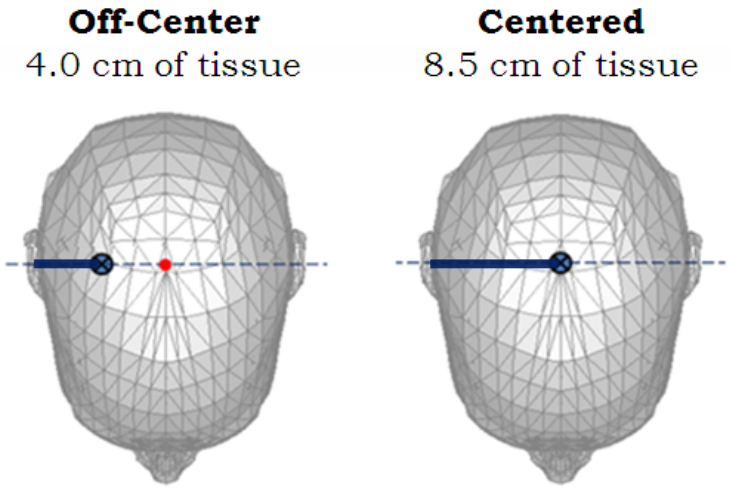

Figure 61: Line-of-Sight Tissue Distances for Centered and Off-Center Inner Dipoles

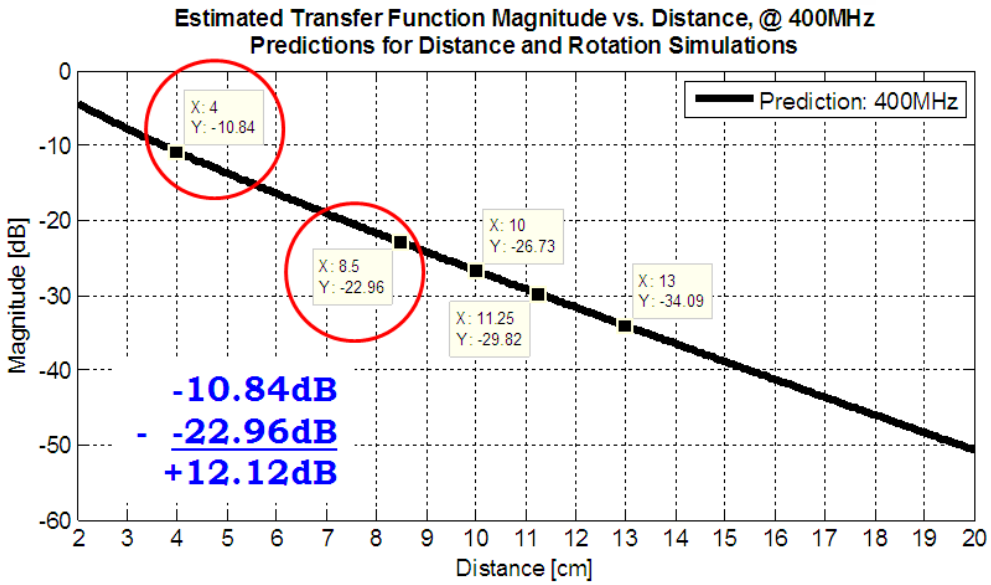

Figure 62: Predicted Power Losses for 400MHz vs. Distance, One Distance Prediction

6.2.5.3 Prediction Results Varying Communication Angle

More predictions can be made when one looks at the results of the antenna rotation simulations. For the centered internal antenna three predictions are made – figures of which can be seen below in *Figure 63*. The results of the centered rotation predictions are replotted in *Figure 64* and are shown with the differences calculated. The predictions, shown and calculated in *Figure 65*, can be seen to be quite close to the simulated values. For the prediction of the power difference between the sides and the front, we are approximately 1dB off, we are less than 1dB off for the power difference between the sides and the front, and we are approximately 0.2dB off for the difference between the back and the front.

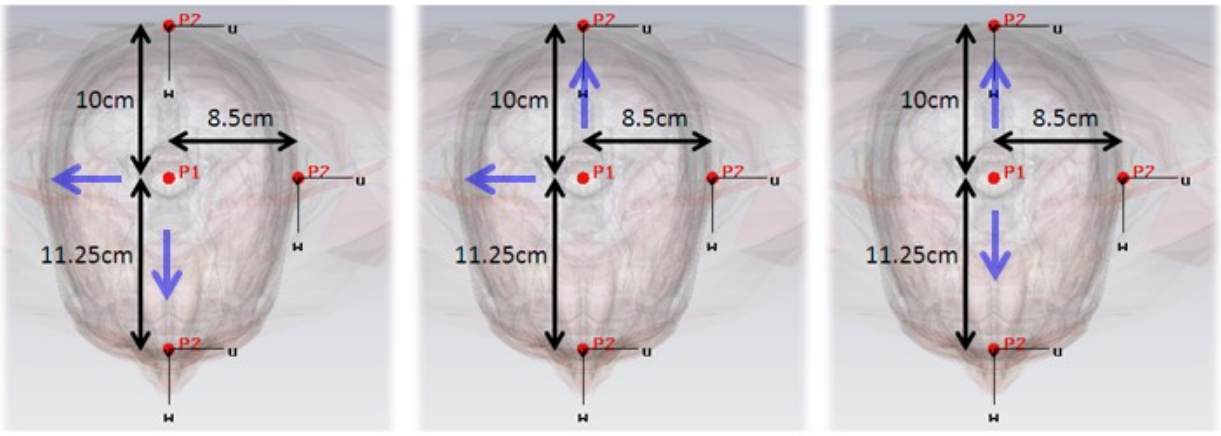

Figure 63: Three Predictions: Side to Front, Side to Back, Front to Back

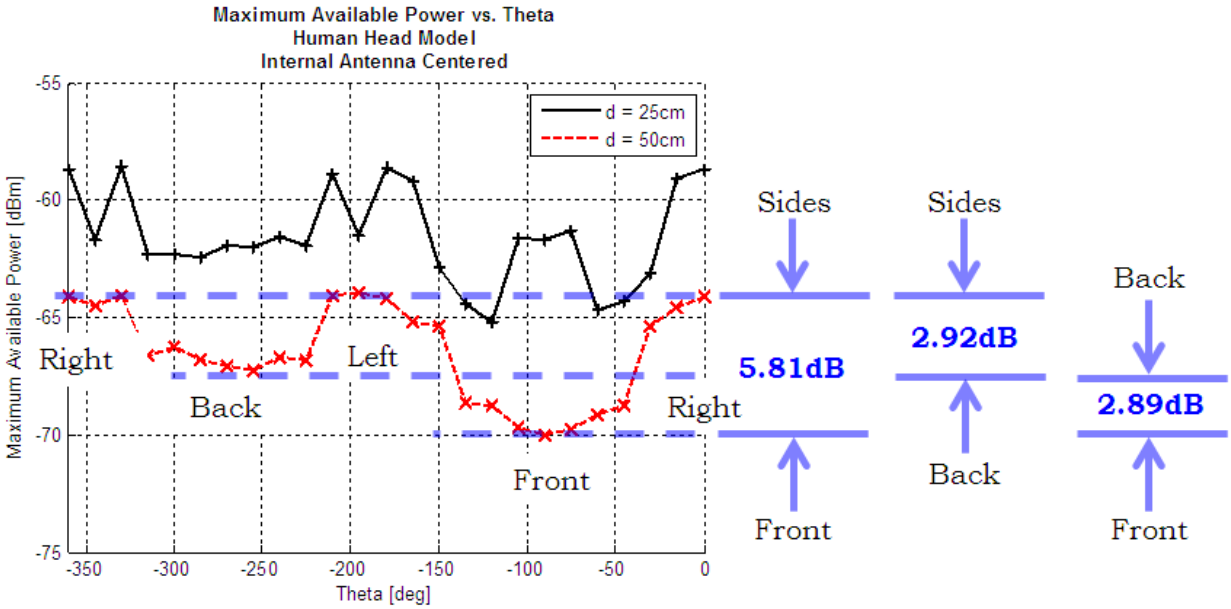

Figure 64: Maximum Available Power vs. Angle, Human Head Model, Centered, d = 25, 50cm, Replotted

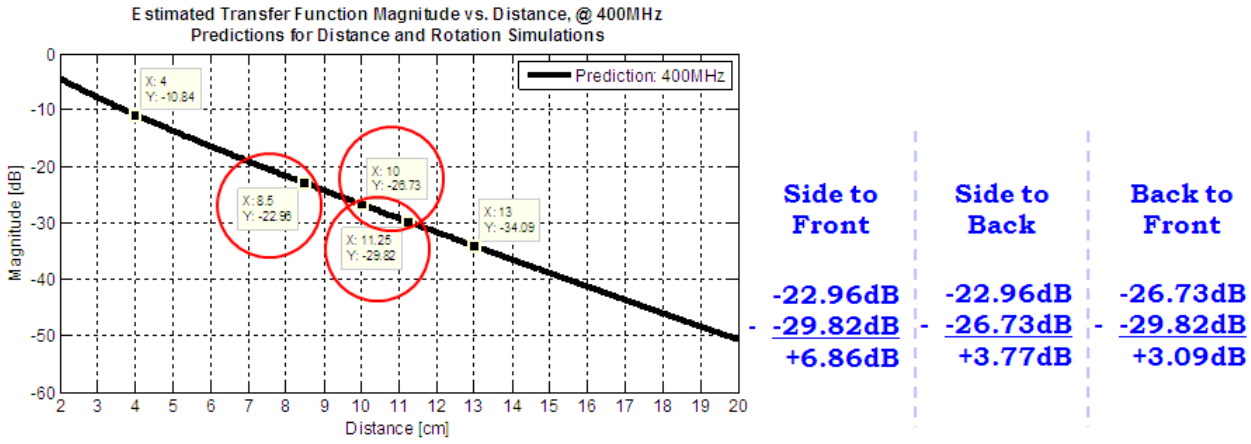

Figure 65: Predicted Power Losses for 400MHz vs. Distance, Three Rotation Predictions

With regard to the off-center internal antenna, only one prediction is attempted – a figure of which can be seen below in *Figure 66*. The simulated results can be seen in *Figure 67* and the predicted difference can be seen in *Figure 68*. This prediction is, comparatively, much worse than the other predictions – it is off by approximately 5dB.

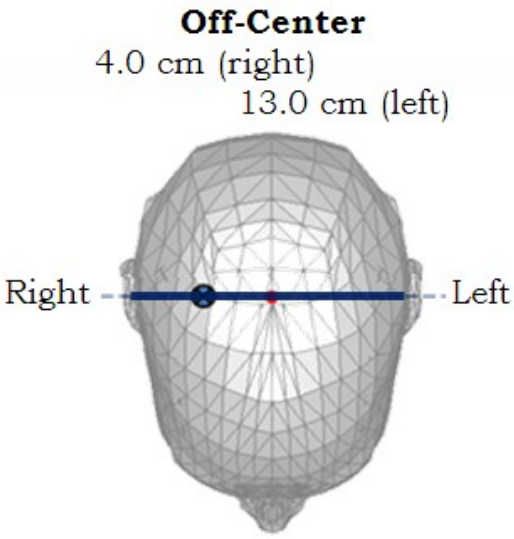

Figure 66: Line-of-Sight Tissue Distances for an Off-Center Inner Dipole

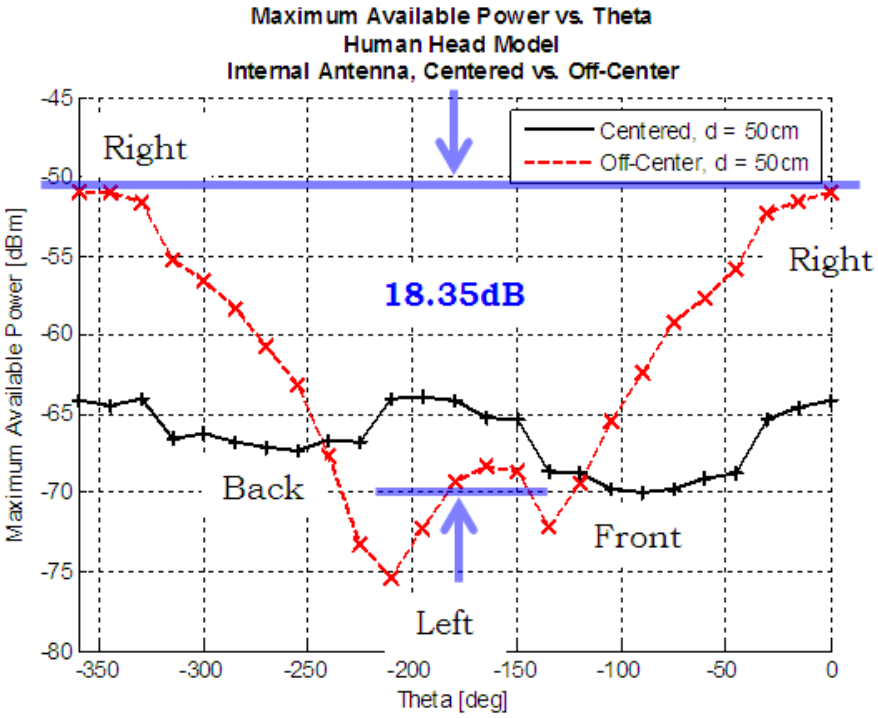

Figure 67: Maximum Available Power vs. Angle, Human Head Model, Centered vs. Off-Center, d = 50cm, Replotted

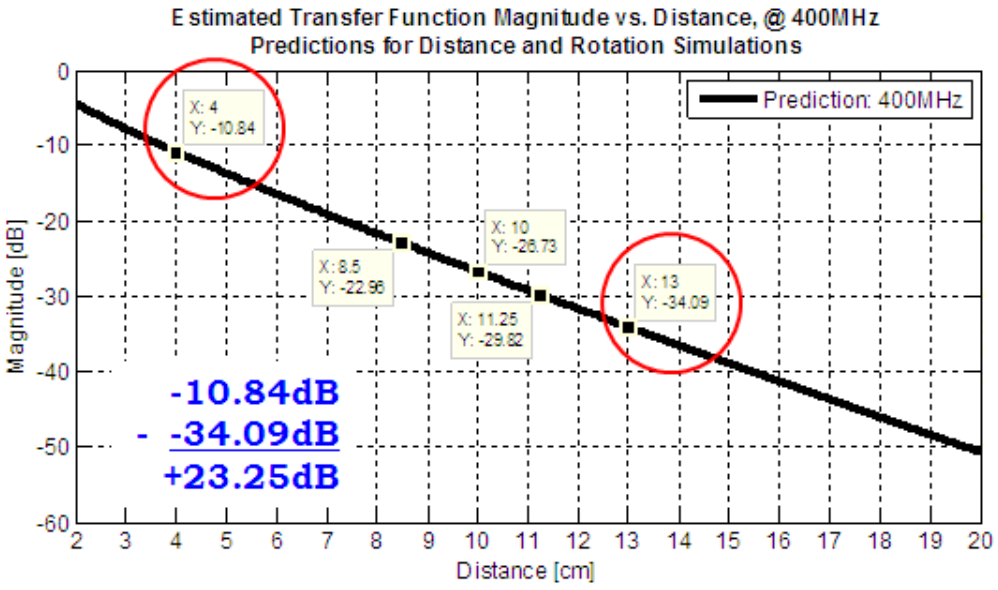

Figure 68: Predicted Power Losses for 400MHz vs. Distance, One Rotation Prediction

6.2.5.4 Prediction Limitations

Four of the five predictions were quite good, but the last prediction – for the off-center internal dipole – was not. This error clearly stems from the un-accounted for extra power around the far side of the head. What this shows, then, is that our transfer function does not take into account all the effects when used in a reciprocal situation (when the *internal* antenna is transmitting).

7. Single Simulations for Completion

Several simulations were done in addition to the above work such that all possibilities were simulated and examined. These simulations were one-time simulations and are briefly shown and explained below.

7.1 Near Field Simulation

To investigate the possibility of near field effects that might explain spikes in our power results, we ran distance simulations for $d \leq 50cm$. These simulations were run for a centered internal antenna at an angle at which the near field effects were thought to occur according to the generated plots. If near field effects are indeed present, the obtained power levels should oscillate for early values of distance and eventually settle out to show a smoother, less chaotic curve sometime before 50 cm. This oscillation occurs in the near field because the wave has not yet resolved into a coherent wave front. The 'turbulence' in the E-field causes oscillations in the E-field and therefore oscillations in the received power. Results for this simulation with a centered dipole and the head at an angle of $\theta = -90°$ are shown below in *Figure 69*.

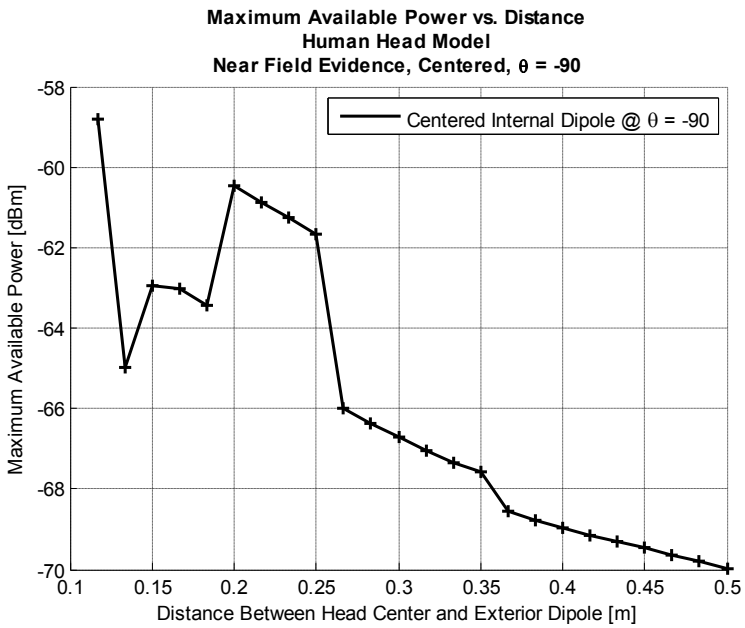

Figure 69: Near Field Effect Simulation, Centered Internal Dipole, $\theta = -90°$

From the plot seen in *Figure 69* we can clearly see oscillatory/chaotic behavior in the received power. This oscillation seems to die down completely just after 35 cm (Before 50 cm, as was predicted). At this specific angle, then, we have shown that near field effects will affect the received power. Received signals should, then, be received at a minimum of 35 cm from the center of the head.

7.2 Internal Communication

Another possibility regarding communication with antennas inside the human head is communication to *other* antennas inside the human head. A simulation was done with two dipole antennas placed inside the skull each 4.5 cm from the center in opposite directions. The setup of this simulation and E-field distribution result at 135 degrees is shown below in *Figure 70*.

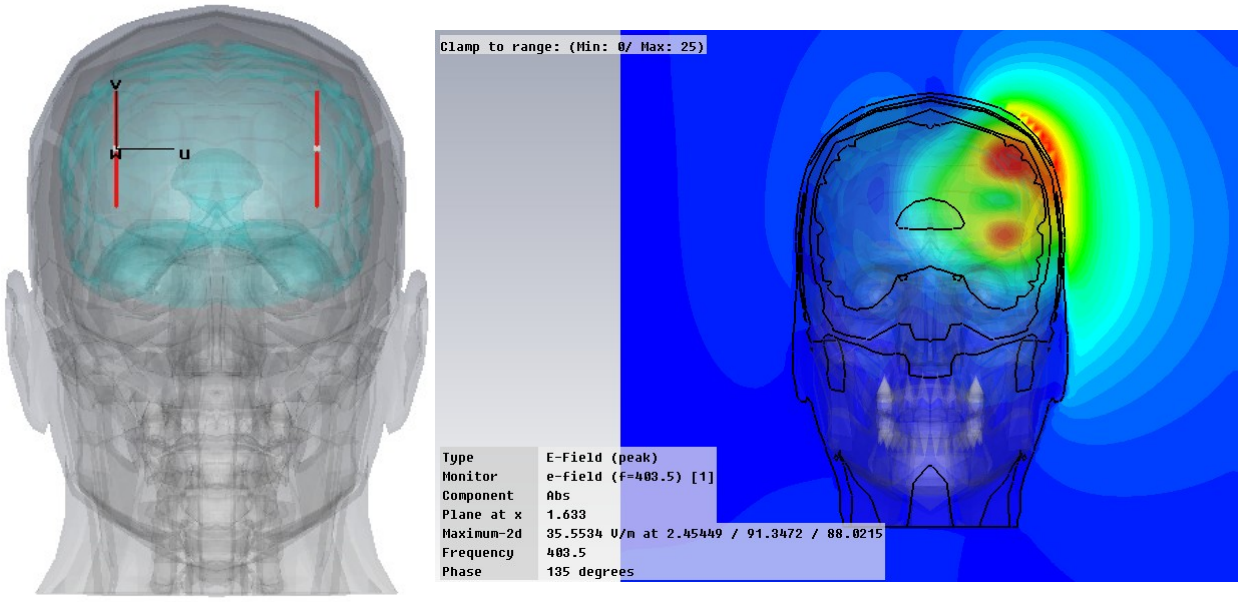

Figure 70: Internal Communication Setup, 3D to 2D E-Field Result at 135 degrees

In *Figure 70* we are shown the two antennas placed in the human head. The antenna at the origin of the coordinate system is the receive antenna and the transmit antenna is placed 9 cm away through the center of the head. The 3D E-field result was plotted on a 2D surface that cut directly through the two dipoles. This specific screen shot is one of several that were animated to show the progression of the EM wave. It is notable to show that the E-field does travel directly through the brain to generate a small field on the receive antenna, but we also see that it generates a field that on the outside of the head that actually 'creeps' around the head. This is shown by the higher power E-field seen at the upper left side of the skull (it is shown to be travelling in the animation). This seems to show that the creeping wave phenomenon described as the major mechanism by which energy is transferred for on body communications in [39] may occur with antennas that are located inside of the body. Overall, the final result obtained for this simulation for the received power was a value of -35.903dBm.

7.3 External Communication

Further work was done to see the effects of just placing a human head in between two antennas separated by a distance *d*. A picture of the setup of this simulation as well as an E-field distribution resulting from the simulation are shown below in *Figure 71*.

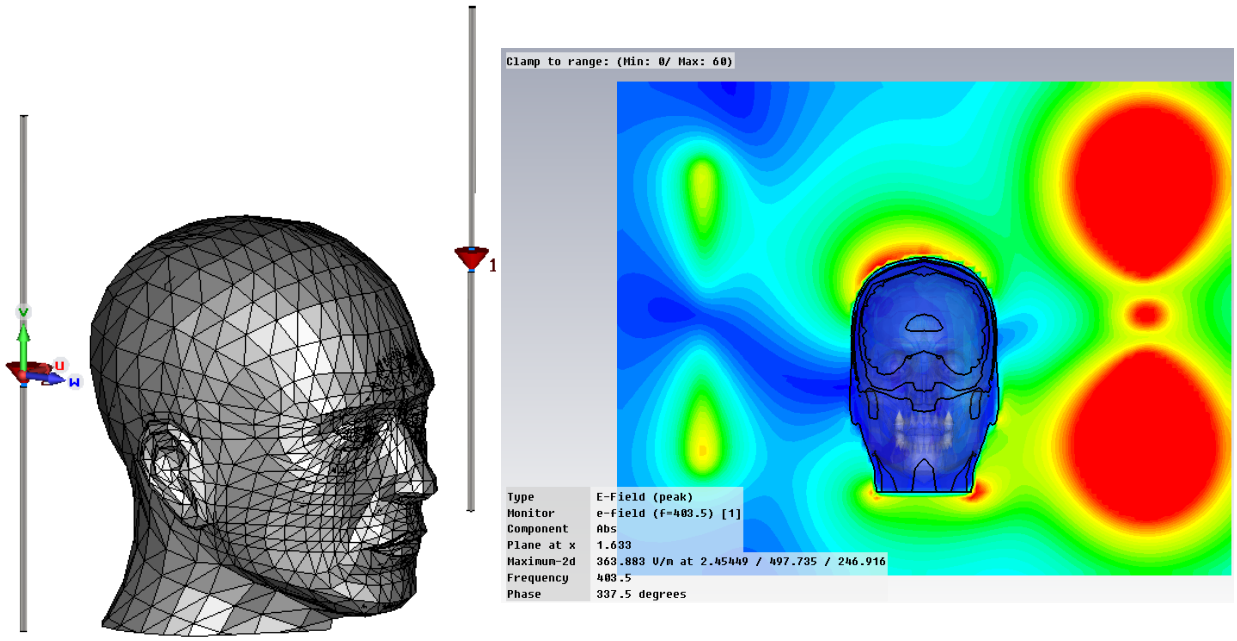

Figure 71: External Communication Setup, 3D to 2D E-Field Result at 337.5 degrees

Each of the dipole antennas were 25 cm from the center of the head and, as in the previous simulation, the antenna located at the coordinate system is the receive antenna. The 3D-to-2D E-field result shows a single frame of an animation that shows how the wave propagates and is received at the receive antenna. Mostly, the wave 'ignores' the head and travels around it, but some of the energy is transferred inside the head – when animated, this internal wave front, as expected, travels much slower that the wave in free space. The final result from this simulation for the power at the received antenna was -16.227dBm. Because we assumed that the antenna was transmitting only 1.83mW, this is a power loss of approximately 18.6dB.

7.4 Specific Absorption Rate

Specific Absorption Rate, or SAR, is a measure of the rate at which power is absorbed by the body when exposed to electromagnetic fields and are very important to simulate to ensure the safety of devices that will be used in or near the body. The formula for SAR is shown below:

$$SAR = \frac{\sigma|E|^2}{\rho} \qquad 49$$

where σ is the conductivity value (which is frequency dependent), $|E|^2$ represents the linear, squared magnitude of the electric field and ρ represents the density of the respective tissue. The units of SAR work out to equal $[W/kg]$. It should be noted here that our transfer function magnitude equation, which is used to estimate the power loss cannot be used to estimate the SAR – this is because the formula for SAR requires the magnitude of the electric field to be squared, whereas we estimate ExH*. A short SAR study, shown below, was examined for this work.

7.4.1 SAR Analysis with Internal Antenna as Transmitter

Although the dipole antenna will most likely not be used in practice for head located implanted antennas, a Specific Absorption Rate (SAR) study was done to analyze the possible SAR distribution throughout the head. This simulation was done for an antenna located at the center of the head and results are shown below in *Figure 72*.

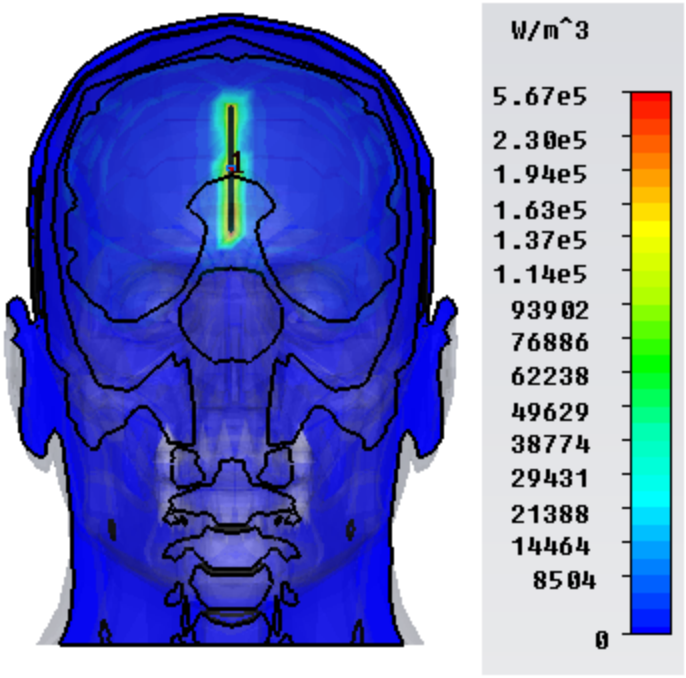

Figure 72: SAR Simulation Setup and Result

We see in *Figure 72* the power loss distribution for a small 2D slice through the center of the dipole antenna. Power loss distribution is not exactly SAR, however – you must define the density of each tissue. This data, however, was not provided in the human body model. Kim and Rahmat-Samii, however, used a value of $1040\ [kg/m^3]$ for brain in their paper [24].

The power loss distribution, in general, seems to mirror the shape of the dipole. The only place it seems to be different is around the port excitation itself – it has a larger sphere of power loss around it than the other locations. Interestingly enough, this is the point at which the highest power loss is found – upwards of $567{,}000\ [W/m^3]$. This is most likely because the excitation is not shielded at all from the tissue. However, if one was to use the value of $1040\ [kg/m^3]$ as the density of the brain, this would translate to a SAR value of approximately $545\ [W/kg]$ – this, of course, is much larger than the SAR value requirement of less than $1.6\ [W/kg]$. Our result,

however, is for a power level of 1W being delivered to the dipole. To be able to use this type of antenna, the power level delivered to the dipole would have to be scaled down such that it abides by the SAR restriction. This would mean the dipole could operate off of a maximum of only 2.94mW of power.

7.4.2 SAR Analysis with External Antenna as Transmitter

We now examine the SAR caused by the external antenna transmitting towards the head. As was done for the previous SAR calculation, CST MWS was used to obtain the power density, in $[W/m^3]$. Once obtained, the densities of multiple tissues were taken from [24], which are shown below in *Table 16*, and the SAR is plotted as the wave passes through the left side of the head in *Figure 73*.

Table 16: Tissue Densities Used by Kim and Rahmat-Samii for SAR Calculation

	$Density$ $(\rho, kg/m^3)$
Brain	1040
Bone	1810
Skin	1010
Muscle	1040

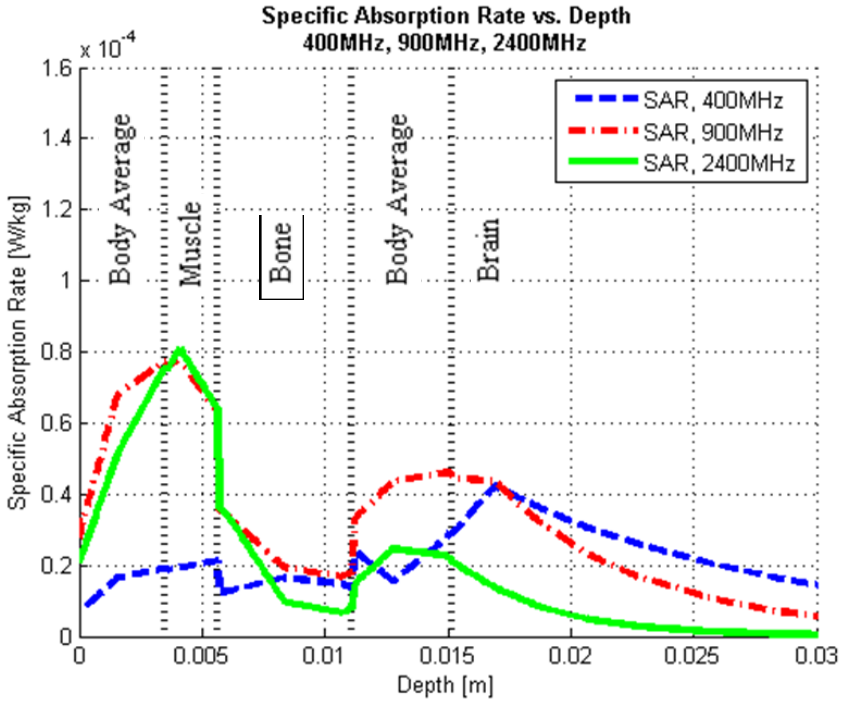

Figure 73: SAR Simulation Results, External Antenna as Transmitter

The vertical black dotted lines represent, for line of sight, the different layers of tissue in the model; each of which corresponds to a different density value. The first 3.5mm is composed of skin (or body_average), 3.5mm-5.6mm is muscle, 5.6mm-11.1mm is cancellous bone, 11.1mm-15.2mm is more body average and anything past 15.2mm is seen as brain. Although the external excitation had a power of 1W, we see extremely low values for SAR in this plot for three different frequencies. This is may be caused, dually, by power reflecting off the head (and not passing through), as well as CST MWS correcting the excitation power level such that power levels are normalized.

8. Conclusion

8.1 Major Contributions of Present Work

To summarize the work done by this paper, we find that there was the development and verification of an E-Field ratio technique to obtain transfer function measurements. The use of E-Field ratios and traditional power loss measurements have been used to obtain the transfer function data presented by the human head over a wide band; this distance and frequency dependent data has been recorded for multiple energy entry angles. The presentation of a new, more generalized version of the well known log-distance, log-frequency path loss models has been shown. Following this, there is the application of this generalized Indoor Propagation path loss model to the wideband transfer function data to describe the human head's magnitude transfer function characteristics. Next, narrowband receiver power level measurements were obtained through simulation of dipole antennas that are placed inside and outside of a detailed human head model – the implant was used as the transmitter and is placed at multiple locations within the head. Measurements at each implant location were recorded for multiple external antenna angles. We then showed that the estimated transfer function could be used to correctly predict the results of power level simulations.

From this work we find that our major contributions are:

1) A realistic human head model with frequency dependent tissue characteristics is used to obtain a transfer function that describes the magnitude and phase of an electromagnetic wave as it propagates through the human head. This transfer function varies over both frequency, and depth into the skull.

2) The obtained transfer function data, captured over a wide frequency range, is then approximated through the use of a modified log-distance, log-frequency communication model for path loss.
3) The estimated transfer function is then used to successfully predict received power from simulations of cranially implanted antennas.

8.2 Applications of Current Work

Applications for work with the brain tend to fall in two main categories: sensing and stimulation. Sensing is the capturing of neural impulses and stimulation is the application of electrical signals to the brain. The work described in this paper can be applied, actually, to both categories because of the necessity of communicating with whatever device is being used.

Many of the sensing applications for this work center around brain-computer interfaces (BCIs). Brain-computer interfaces translate brain signals (neural activity) into some sort of output that, in general, is used to communicate the will of the user. The applications for this type of interface are the most beneficial for the severely handicapped, disabled or 'locked in' individuals that have little to no control of their motor functions but whose mental faculties remain intact. The BCI would essentially allow the patient, through the translation of their brain signals, to interact with the world around them. The clearest example of an application for this would be for use in the next generation of prosthetic limbs. The first necessary part of the BCI equation is the recording of neural activity. This can be done in several ways and can be done from outside of the head, on the surface of the brain or from locations inside the brain.

Two methods of recording brain signals are electroencephalography (EEG) and electrocorticography (ECoG). An EEG records electroencephalographic activity from the scalp and is, therefore, a non-invasive method of recording neural impulses. Often a cap with sensors

is worn by the patient and the EEG activity is captured and processed to obtain the desired output – moving a cursor on a screen or controlling a prosthetic limb. EEG, however, requires an extensive training period to work well, it has low spatial resolution for recorded signals from the brain, and is susceptible to interference. Electrocorticography, as compared to EEG, is an invasive method of recording brain signals. In ECoG a matrix of sensors are placed on the outer cortex of the brain on the dura mater (directly beneath the skull, on top of the brain) and *these* are used to record the neural activity. Compared to EEG, ECoG has a much higher spatial resolution (fractions of millimeters for ECoG vs. centimeters for EEG), larger signal amplitudes, larger bandwidths and is less vulnerable to artifacts from other sources, such as noise. Pictures of how ECoG is achieved in practice are shown below [56]:

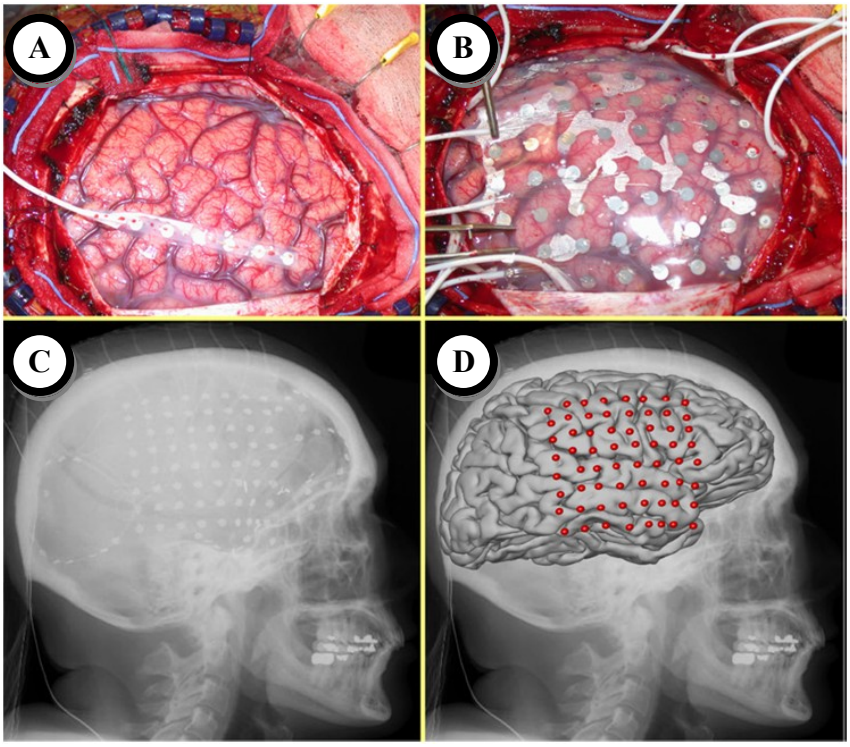

Figure 74: (A) Exposed human brain after craniotomy (B) 8x8 ECoG sensor grid placed on the human brain (C) X-Ray image of a human skull with ECoG sensor grid (D) Average brain template with electrode locations highlighted

As recently as 2006, this type of BCI was actually tested on human subjects with success. This neural interfacing used, however, percutaneous connectors (connectors that pass directly through the skin). The use of this type of connection brings implicit disadvantages such as infection risks, the possibility of damage (to both the connector and the connection through the skull) and more. As was presented in this work, wireless communication through the skull can be used to solve many of these problems. The next generation of these BCIs is moving towards the safer and easier to use wireless communication option. An example of a wireless neural activity transmitter device that has recently been fabricated is shown below [57]:

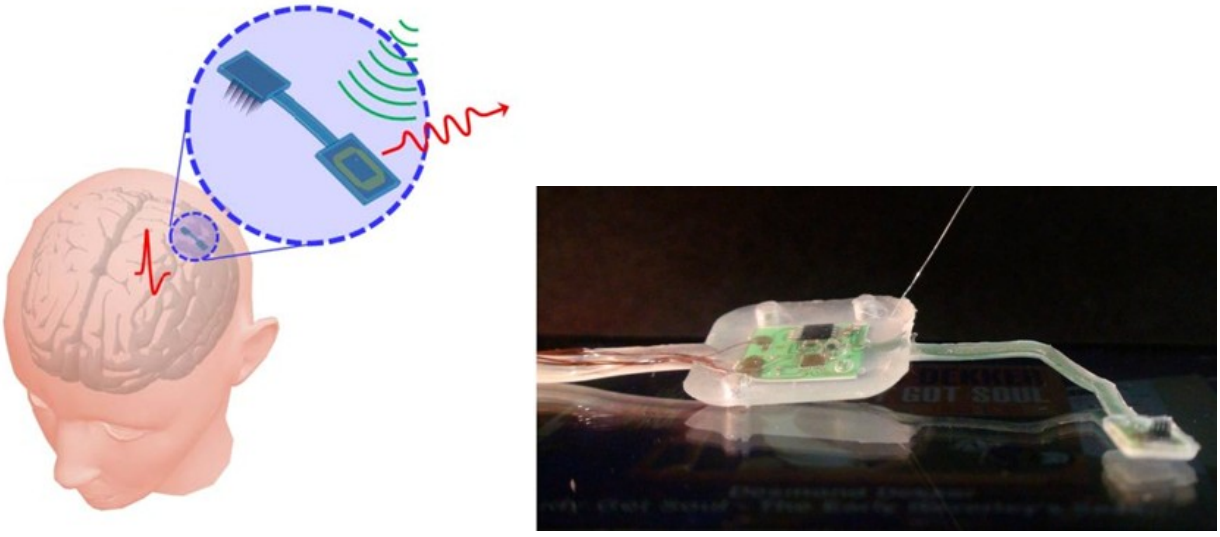

Figure 75: Neural Activity Recording Device, Concept and Fabricated Device

The largest application of this research regarding the stimulation of electrical signals is found in the need to better communicate with deeply implanted electrodes like those found in Deep Brain Simulation (DBS). Deep brain stimulation is an extremely important neurological therapy that is used to treat many different types of disorders and diseases. A classical DBS system consists of several electrical contacts that are placed deep inside the brain (different areas for the treatment of different conditions) which are then connected through a long wire that

travels down the back of the skull to a pulse generator that is implanted in the chest. Recent improvements have shown that the pulse generator can actually be implanted in the skull. Risks of damage caused by parts shifting in the skull and infection risks are increased with the use of the wire, etc.

Regarding how deep brain stimulation works, the implanted pulse generator (IPG) generates electrical impulses that travel through the electrodes and 'shock' the brain. This is an attractive procedure because of its reversibility – once the electrodes are removed, any side effects from their placement are eliminated. DBS requires multiple sessions with medical professionals to determine the best possible 'pulse schedule' as generated by the IPG. Once this is done, DBS has shown varying levels of success for many different diseases / disorders such as: Parkinson's disease, essential tremors, multiple sclerosis, chronic neuropathic pain, epilepsy, tourette syndrome, obsessive compulsive disorder, depression, etc. Work continues to see if it can be used to treat hypertension, obesity, aggressiveness, drug addiction and even if it can be used to improve memory. Communication with the IPG is necessary and, as shown in this work, could be done wirelessly to eliminate some risks that are caused by some current methods. Interestingly, DBS electrodes have also been seen to also double as sensing electrodes and could also be used for the wireless transfer of neural information required by BCIs and ECoG has also been used for stimulation in the treatment of epilepsy.

Therefore, this work can be seen as a first step towards characterizing wireless interfaces for use in neural sensing and stimulation. The use of this work to create these wireless links for electrocorticography and DBS will help to increasing patient comfort, decreasing the risk of infection, decreasing the risk of complications, simplify use and, overall, be safer.

8.3 Future Work

The field of implantable antennas is very young this work is one of the first milestones. If implants are eventually going to be in use, better antennas must be designed. This work focused on the use of simple dipole antennas, however extensions of this work can include the design and simulation of more specialized antennas – specifically for use on the surface of the brain or for more deeply implanted electrodes.

Simulation using the E-field ratio technique allows for phase data to be captured just as easily as magnitude data. This paper briefly shows examples of this data but further studies could focus more on examination of the phase data of the transfer functions.

Note also that all of the work for this paper was done in simulation. Simulations, no matter how precise, are just simulations. Actual physical data must be captured and analyzed. Although verification of this current work is infeasible for human testing (as the antenna design rules this out), work can be done using phantom models to experimentally verify simulated results.

Lastly, in the field of communications, work can be done in the future using simulation results to design antenna diversity systems to boost performance of a communication system transmitting from the head. More work could be done, as well, to try and characterize the effects of oblique incidence to the head – which may be causing the effects that we have attributed to creeping waves. To more fully realize an accurate model for internal-to-external antenna communication, the creeping wave effect should be further examined to show that it is in fact a creeping wave and, if so, characterize its effect on the channel so that the approximated path loss is closer to reality.

REFERENCES

[1] C. Gabriel, S. Gabriel, and E. Corthout, “The dielectric properties of biological tissues: I. Literature survey,” *Phys. Med. Biol.*, vol. 41, pp. 2231-2249, 1996.

[2] S. Gabriel, R. W. Lau, and C. Gabriel, “The dielectric properties of biological tissues: II. Measurements in the frequency range 10 Hz to 20 GHz,” *Phys. Med. Biol.*, vol. 41, pp. 2251–2269, 1996.

[3] S. Gabriel, R.W. Lau, and C. Gabriel. “The dielectric properties of biological tissues: III. Parametric models for the dielectric spectrum of tissues,” *Phys. Med. Biol.*, vol. 41, pp. 2271-2293, 1996.

[4] D. Miklavcic, N. Pavselj, and F. X. Hart, “Electric properties of tissues,” in *Wiley Encyclopedia of Biomedical Engineering*. New York: Wiley, 2006.

[5] C. Gabriel, T. Y. A. Chan, and E. H. Grant, “Admittance models for open ended coaxial probes and their place in dielectric spectroscopy,” *Phys Med. Biol*, vol. 39, pp. 2183–2200, 1994.

[6] K. R. Foster, J. L. Schepps, R. D. Stoy and H. P. Schwan, Dielectric properties of brain tissue between 0.01 and 10 GHz, Phys. Med. Biol. 24, 1177-1187, 1979.

[7] M. Mrozowski and M. A. Stuchly, “Parameterization of media dispersive properties for FDTD,” *IEEE Trans. Antennas Propag.*, vol. 45, no. 9, pp. 1438–1439, Sep. 1997.

[8] J.M. Alison, R.J. Sheppard, Dielectric properties of human blood at microwave Frequencies, *Phys. Med. Biol.* ,Vo1.38, pp. 971 - 978, 1993.

[9] D. V. Land and A. M. Campbell, “A quick accurate method for measuring the microwave dielectric properties of small tissue samples,” *Phys. Med. Biol.*, vol. 37, pp. 183–192, 1992.

[10] D. Popovic, L. McCartney, C. Beasley, M. Lazenik, M. Okoniewski, S. C. Hagness, J. H. Booske, "Precision open-ended coaxial probes for in vivo and ex vivo Spectroscopy of biological tissues at microwave frequencies", Trans. IEEE Microw. Theory Tech., Vol. MTT-53, No. 5, pp. 1713-1721, 2005.

[11] A. P. O’Rourke, M. Lazebnik, J. Bertram, M. C. Converse, S. C. Hagness, J. G.Webster, and D. M. Mahvi, “Dielectric properties of human normal, malignant, and cirrhotic liver tissue: In vivo and ex vivo measurements from 0.5 to 20 GHz using a precision open-ended coaxial probe,” *Phys. Med. Biol.*, vol. 52, pp. 4707–4719, Jul. 2007.

[12] J. L. Schepps and K. R. Foster, “The UHF and microwave dielectric properties of normal and tumor tissue: Variation in dielectric properties with tissue water content,” *Phys. Medicine and Biology,* vol. 25, no. 6, pp. 1149–1159, 1980.

[13] S. Grimnes and Ø. Martinsen, *Bioimpedance and Bioelectricity Basics*. London, UK: Academic, 2000.

[14] M. Yvanoff, J. Venkataraman, "A Feasibility Study of Tissue Characterization Using LC Sensors," *IEEE Transactions on Antennas and Propagation,* vol. 57, issue 4, pp. 885-893, Apr. 2009.

[15] W. D. Hurt, "Multiterm Debye dispersion relations for permittivity of muscle," *IEEE Trans. Biomed. Eng.*, vol. BME-32, pp. 60–64, Jan. 1985.

[16] FCC Rules and Regulations, "Medical Device Radiocommunications Service", *Part 95*, Aug. 2009.

[17] CommLaw Conspectus: Journal of Communications Law and Policy, "Selected FCC Docket Summaries, 2009," [Online]. Available: http://commlaw.cua.edu. [Accessed: Nov, 2009].

[18] H. Savci, A. Sula, Z. Wang, N. S. Dogan, and E. Arvas. MICS transceivers: regulatory standards and applications (medical implant communications service). In Proceedings of IEEE SoutheastCon 2005, pages 179–182, April 2005.

[19] Australian Communications Authority, "Planning for Medical Implant Communications Systems (MICS) & Related Devices", *Document: SPP 6/03*, Oct. 2003.

[20] Huan-Bang Li, Takashi Takahashi, Masahiro Toyoda, Yasuyuki Mori, and Ryuji Kohno, "Wireless Body Area Network Combined with Satellite Communication for Remote Medical and Healthcare Applications," Journal of Wireless Personal Communications, to be appeared.

[21] FCC Rules and Regulations, "WMTS Band Plan", *Part 95*, Mar. 2003.

[22] B. Zhen, H. Li, and R. Kohno, *IEEE body area networks and medical implant communications*. Brussels, Belgium: ICST, 2008.

[23] P. S. Hall and Y. Hao*, Antennas and Propagation for Body-Centric Wireless Communications*. Norwood, MA: Artech House, 2006.

[24] J. Kim and Y. Rahmat-Samii, "Implanted antennas inside a human body: simulations, designs and characterizations," *IEEE Trans. Microwave Theory Tech.*, vol. 52, no. 8, pp. 1934–1943, Aug. 2004.

[25] J. Kim and Y. Rahmat-Samii, "SAR reduction of implanted planar inverted f antennas with non-uniform width radiator," *Antennas and Propagation Society International Symposium.*, pp. 1091-1094, July 2006.

[26] P. Soontornpipit, C. Y. Furse and Y. C. Chung, "Design of Implantable Microstrip Antenna for Communication With Medical implants," IEEE Trans. Microwave Theory Tech., vol. 52, no.8, pp. 1944-1951, Aug.2004.

[27] Lee, C.M.; Yo, T.C.; Luo, C.H.; Tu, C.H.; Juang, Y.Z., **"**Compact broadband stacked implantable antenna for biotelemetry with medical devices," *Electronics Letters,* Volume 43, Issue 12,Page(s): 660 – 662, June 7 2007

[28] A.J. Johansson, *Wireless Communication with Medical Implants: Antennas and Propagation*, Ph.D. thesis, Lund University, Sweden, June 2004.

[29] M. Norris and J.-D. Richard, "Sub-miniature antenna design for wireless implants," in *Proceedings of the IET Seminar on Antennas and Propagation for Body-Centric Wireless Communications*, pp. 57–62, London, UK, April 2007.

[30] P. Soontornpipit, C. M. Furse, and Y. C. Chung, "Miniaturized biocompatible microstrip antenna using genetic algorithm," *IEEE Trans. Antennas Propag.*, vol. 53, no. 6, pp. 1939–1945, Jun. 2005.

[31] Yasir Ahmed, Yang Hao and Clive Parini, "*A 31.5 GHZ Patch Antenna Design for Medical Implants",* University of London, *International Journal of Antennas & Propagation", volume 2008, (2008), article ID 167980.*

[32] A. J. Johansson, "Wave-propagation from medical implants–influence of body shape on radiation pattern", EMBS/BMES Conference, Vol.2, pp. 1409-1410, 2002.

[33] A. J. Johansson, A. Karlsson, "Wave-Propagation from Medical Implants – Influence of Arm Movements on the Radiation Pattern," *Proceedings of radiovetenskap och kommunikation RVK 02, Radiovetenskap och Kommunikation*, Stockholm, Sweden, pp. 705-708, 2002-06-11/2002-06-13

[34] Miry C., Gillard R., Loison R., "An Application of the Multi-Level DG-FDTD to the Analysis of the Transmission Between a Dipole in Free-Space and an Implanted Antenna in a Simplified Body Model with Various Positions," *Communications présentées à EUCAP 2009 IETR – UMR CNRS 6164*, Berlin, Germany, March 23-27 2009.

[35] S. Hagness, A. Taflove, and J. E. Bridges, "Three-dimensional FDTD analysis of a pulsed microwave confocal system for breast cancer detection: Design of an antenna-array element," *IEEE Trans. Antennas Propagat.*, vol. 47, pp. 783–791, May 1999.

[36] X. Li, E. J. Bond, S. C. Hagness, B. D. Van Veen, and D. van derWeide, "Three-dimensional microwave imaging via space–time beamforming for breast cancer detection," presented at the *IEEE AP-S Int. Symp. And USNC/URSI Radio Science Meeting*, San Antonio, TX, June 2002.

[37] E. C. Fear, S. C. Hagness, P. M. Meaney, M. Okoniewski, and M. A. Stuchly, "Enhancing breast tumor detection with near field imaging," *IEEE Microwave Mag.*, vol. 3, pp. 8–56, Mar 2002.

[38] Jun-ichi Takada, Takahiro Aoyagi, Kenichi Takizawa, Norihiko Katayama, Hirokazu Sawada, Takehiko Kobayashi, Kamya Yekeh Yazdandoost, Huan-bang Li, and Ryuji Kohno, "Static Propagation and Channel Models in Body Area," COST 2100 6th Management Committee Meeting, TD(08)639, Oct. 2008.

[39] J. Ryckaert, P. De Doncker, R. Meys, A. de Le Hoye, S. Donnay, "Channel model for wireless communication around the human body", Electronics Letters, Vol.40, Nr.9, pp.543-544, April 2004.

[40] A. Fort, C. Desset, P. Wambacq, and L. Biesen, "Indoor body-area channel model for narrowband communications," *Microwaves, Antennas & Propagation, IET*, vol. 1, no. 6, pp. 1197–1203, Dec. 2007

[41] A.A. Serra, P. Nepa, G. Manara, and P.S. Hall, "Diversity Measurements for On-Body Communication Systems," *IEEE Antenna and Wireless Propagation Letters*, vol. 6 (1), pp. 361 – 363, 2007.

[42] A. Fort, C. Desset, P. deDoncker, P. Wambacq, and L. van Biesen, "An ultra-wideband body area propagation channel model-from statistics to implementation," *IEEE Transactions on Microwave Theory and Techniques*, vol. 54, no. 4, pp. 1820–1826, April 2006.

[43] S. Gupta, S. Lalwani, Y. Prakash, E. Elsharawy, and L. Schwiebert. Towards a propagation model for wireless biomedical applications. In IEEE Intl. Conference on Communications, May 2003.

[44] A. Alomainy, Y. Hao, Y. Yuan, and Y. Liu, "Modelling and Characterization of Radio Propagation from Wireless Implants at Different Frequencies," in Proc. European Conference on Wireless Technology, Sep. 2006.

[45] K. Tai, H. Harada, R. Kohno, "Channel Modeling and Signaling of Medical Implanted Communication Systems and a Step to Medical ICT," in Proc. Mobile and Wireless Communications Summit, 2007.

[46] P. Debye, *Polar Molecules*, Chem. Catalog Co., New York, 1929.

[47] C. A. Balanis, *Advanced Engineering Electromagnetics.* New York: Wiley, 1989.

[48] Italian National Research Council, "Dielectric Properites of Body Tissues," *Institute for Applied Physics*, [Online]. Available: http://niremf.ifac.cnr.it/tissprop/htmlclie/htmlclie.htm [Accessed: June 2009].

[49] Y. Duroc, T.-P. Vuong, and S. Tedjini, "Realistic modeling of antennas for ultra wide band systems," in *Proc. IEEE Radio and Wireless Conf.*, Jan. 2006, pp. 347–350.

[50] Y. Duroc, A. Ghiotto, T.-P. Vuong, and S. Tedjini, "UWB antennas: Systems with transfer function and impulse response," *IEEE Trans. Antennas Propag.*, vol. 55, no. 5, pp. 1449–1451, May 2007.

[51] Mohammadian, A. H., A. Rajkotia, and S. S. Soliman, "Characterization of UWB transmit-receive antenna system," *Proc. of Ultra Wideband Systems and Technologies*, 157–161, 2003.

[52] C. D. Meyer, *Matrix Analysis and Applied Linear Algebra*, SIAM, Philadelphia, 2000.

[53] T. Rappaport. Wireless Communications: Principles & Practice 2nd edn. Prentice-Hall, Inc., New Jersey, 2002.

[54] A. F. Molisch et al., "IEEE 802.15.4a channel model - final report," Tech. Rep. Document IEEE 802.15-04-0662-02-004a, 2005.

[55] Balanis, C. A. Antenna Theory: Analysis and Design 3rd edn (Wiley, Hoboken, New Jersey, 2005).

[56] Schalk G, Miller KJ, Anderson NR, Wilson JA, Smyth MD, Ojemann JG, Moran DW, Wolpaw JR, Leuthardt EC (2008) Two-dimensional movement control using electrocorticographic signals in humans. J Neural Eng 5:75–84.

[57] Nanophotonics and Neuroengineering Laboratory, "Wireless, Ultra Low Power, Broadband Neural Recording Microsystem," *Brown University*. [Online]. Available: http://nurmikko.engin.brown.edu/?q=node/1. [Accessed: Nov. 2009].

APPENDIX A

SECOND ORDER POLYNOMIAL CURVE FITTING

$$\widehat{X}(f,d) = k + n(d) + m\left(\frac{f}{f_0}\right) + l(d)^2 + a\left(\frac{f}{f_0}\right)^2 \qquad 50$$

Table 17: MMSE Variables and Ave Error for a Second Order Polynomial Model, All Angles

	Front	***Left***	***Back***	***Top***
k	29.9429	36.6127	36.6284	48.3164
n	−763.5749	−997.0426	−955.5864	−1281.68
m	−5.4761	−5.375	−5.5593	−6.5642
l	684.9203	2344.9749	2490.2842	4168.5266
a	0.1902	0.14392	0.19218	0.23108
$\sigma_{error}\ [dB]$	4.2497	5.1596	4.7308	6.2798

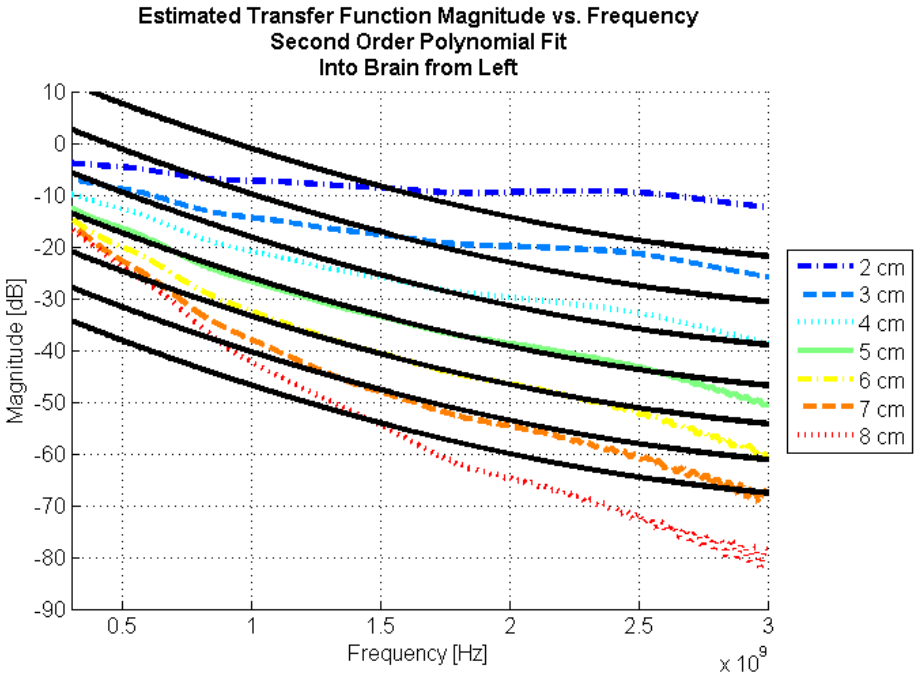

Figure 76: Simulated and Estimated Curves, 2:1:8cm, 2nd Order Polynomial Fit, Left

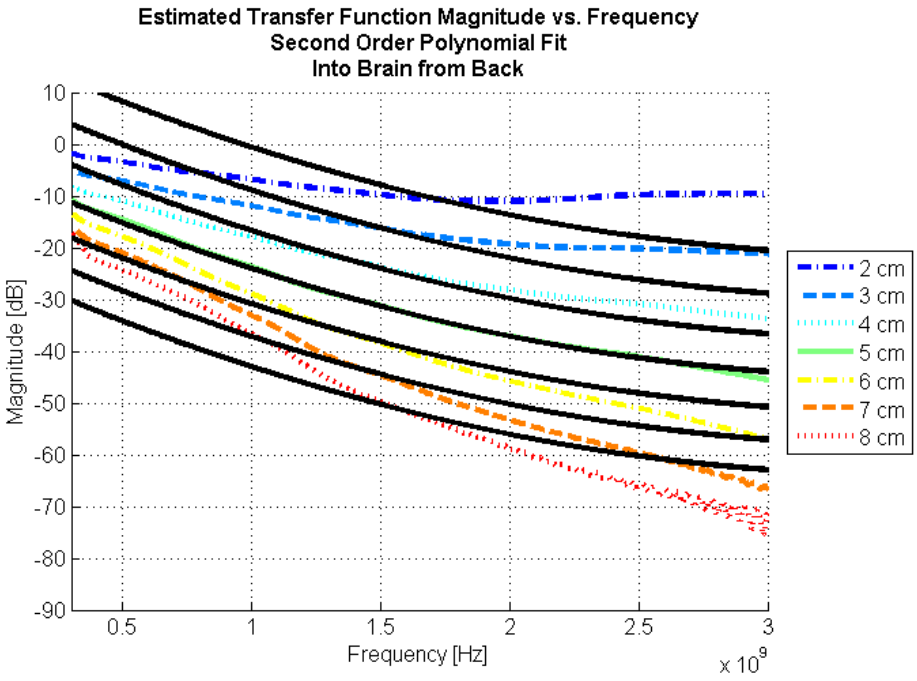

Figure 77: Simulated and Estimated Curves, 2:1:8cm, 2nd Order Polynomial Fit, Back

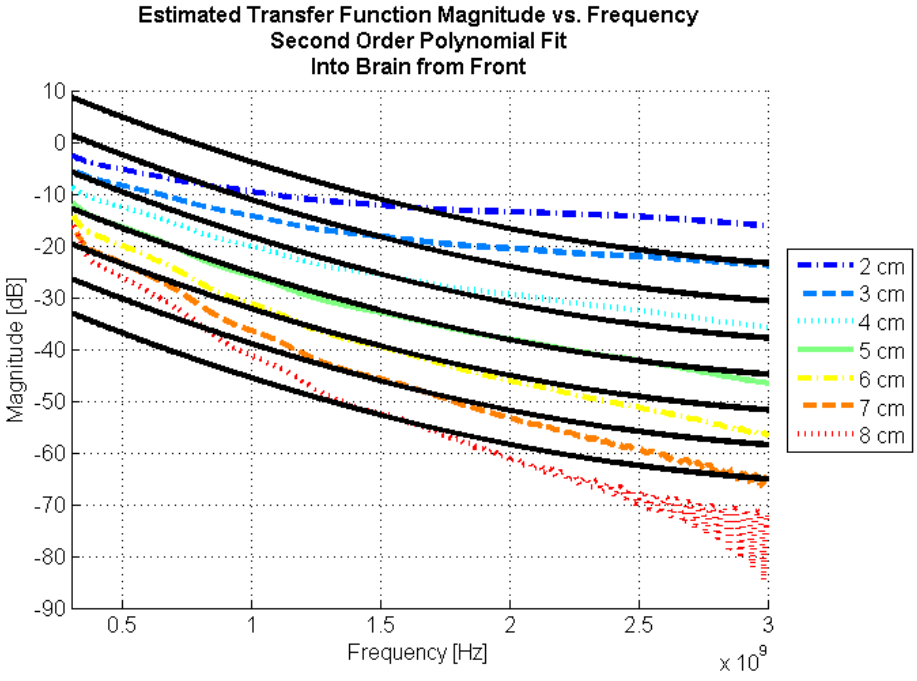

Figure 78: Simulated and Estimated Curves, 2:1:8cm, 2nd Order Polynomial Fit, Front

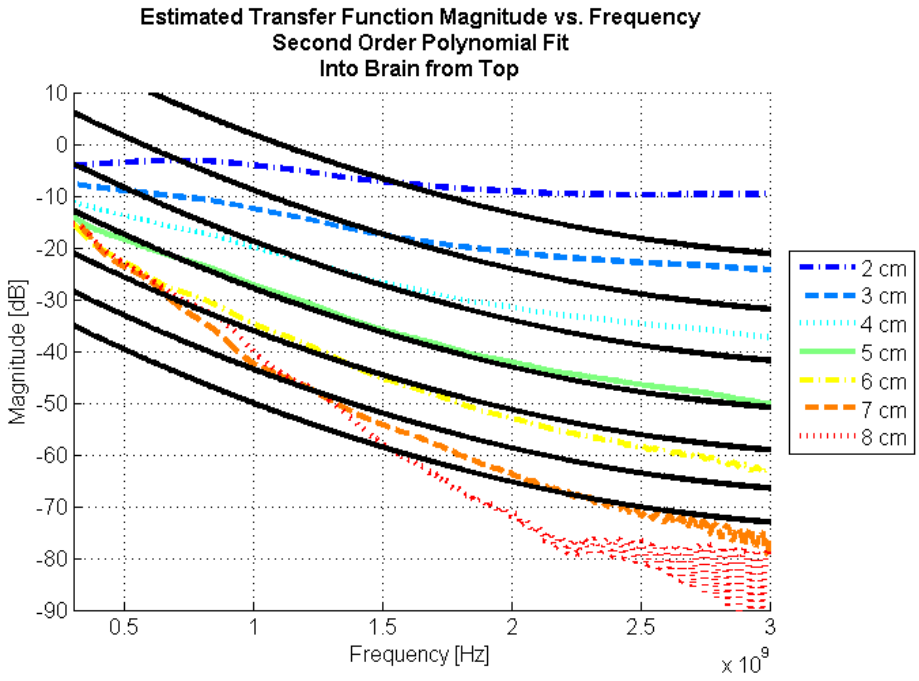

Figure 79: Simulated and Estimated Curves, 2:1:8cm, 2nd Order Polynomial Fit, Top

MODIFIED SECOND ORDER POLYNOMIAL CURVE FITTING

$$\hat{X}(f,d) = k\left(\frac{d}{d_0}\right) + n\left(\frac{f}{f_0}\right)(d) + m\left(\frac{d}{d_0}\right)\left(\frac{f}{f_0}\right) + l\left(\frac{f}{f_0}\right)(d)^2 + a\left(\frac{d}{d_0}\right)\left(\frac{f}{f_0}\right)^2 \quad (51)$$

Table 18: MMSE Variables and Ave Error for a Modified Second Order Polynomial Model, All Angles

	Front	***Left***	***Back***	***Top***
k	-2.6268	-2.4107	-1.7994	-1.2455
n	-0.039789	-0.037702	-0.037567	-0.044396
m	-1.9895	-1.8851	-1.8783	-2.2198
l	-135.8625	-288.0038	-235.1522	-443.2648
a	0.072551	0.073593	0.070497	0.099219
σ_{error}	1.0459	1.9680	1.8315	2.9974

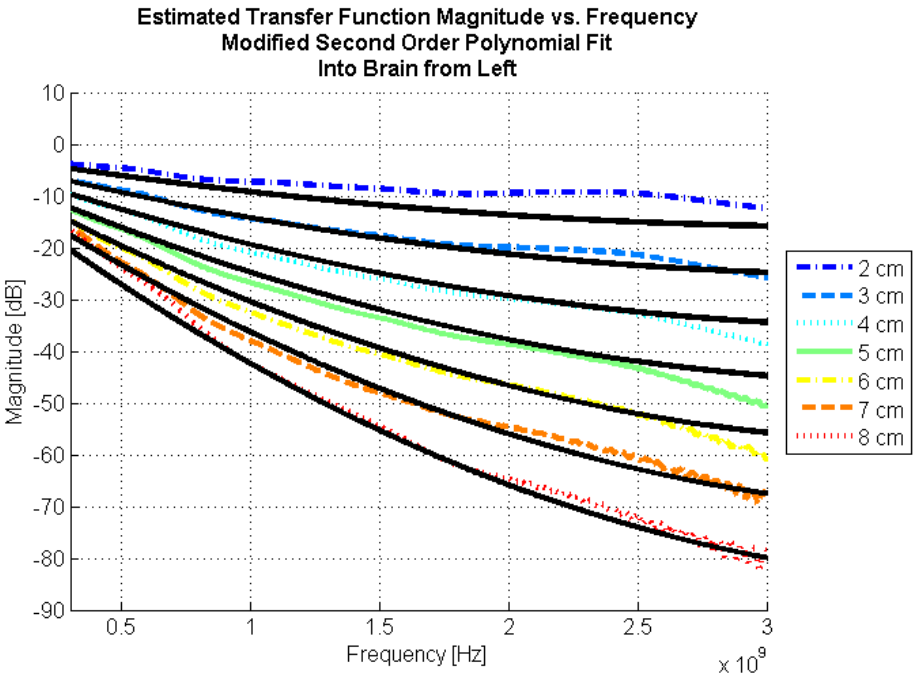

Figure 80: Simulated and Estimated Curves, 2:1:8cm, Modified 2nd Order Polynomial Fit, Left

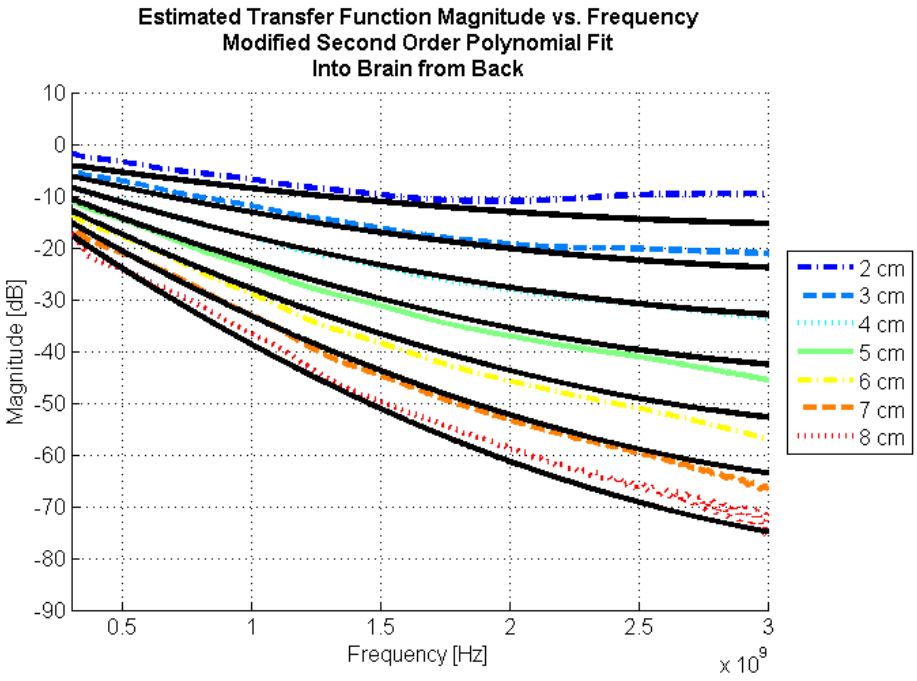

Figure 81: Simulated and Estimated Curves, 2:1:8cm, Modified 2nd Order Polynomial Fit, Back

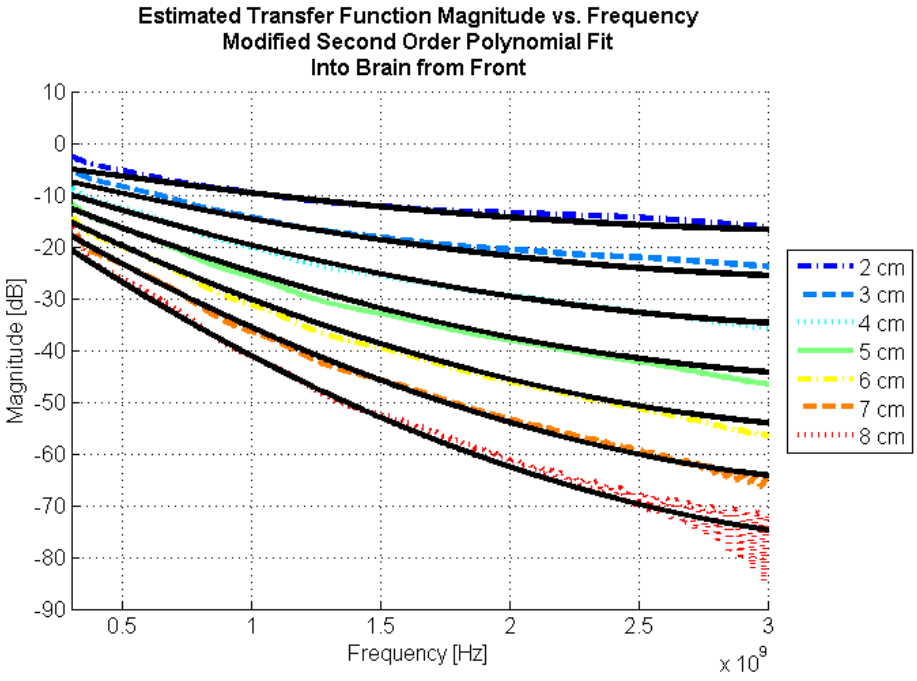

Figure 82: Simulated and Estimated Curves, 2:1:8cm, Modified 2nd Order Polynomial Fit, Front

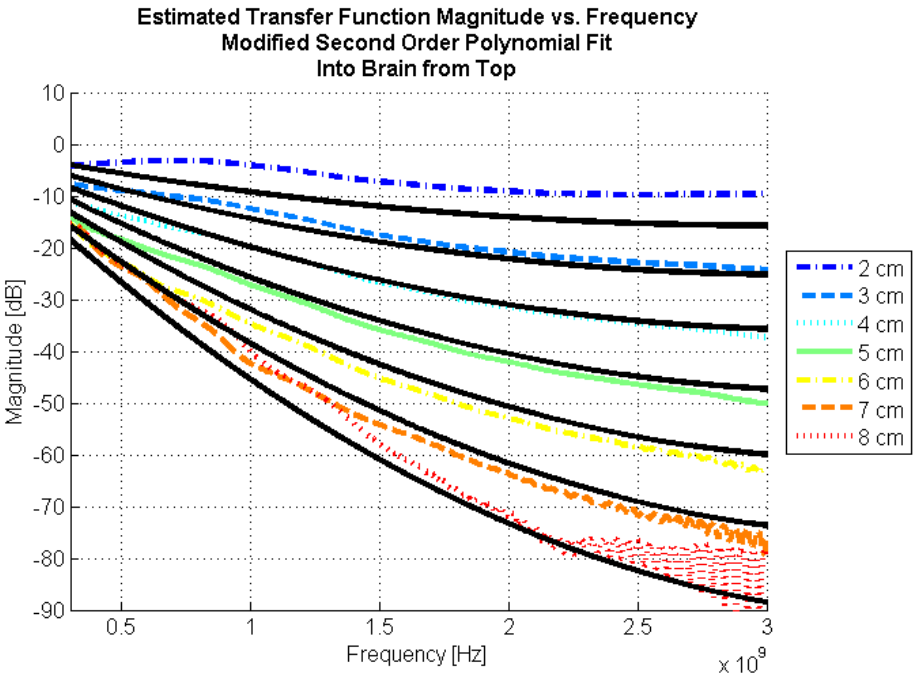

Figure 83: Simulated and Estimated Curves, 2:1:8cm, Modified 2nd Order Polynomial Fit, Top

APPENDIX B

MATLAB CODE – m-files and their functions are listed below; many of the files are quite similar. For this reason, only m-files with a dark grey background are shown in their entirety.

m-file name	**function**
f_extractTF	This function is used to import an input and output time domain signal and calculate the FFTs of each of them. Using this data, we output three main things: the time domain signals again (when plotted vs. t), the calculated frequency domain signals (when plotted vs. f_FFT), and the final transfer function (when plotted vs. f_FFT).
f_import_left_data.m	This script uses the f_extractTF() to output the transfer functions for each depth into the head from the left. The transfer function is output from this function as a complex number - if one would like to take the magnitude or phase, it must be done in the program that calls this function afterwards.
f_import_back_data.m	Same as above, for data from the back of the head
f_import_front_data.m	Same as above, for data from the front of the head
f_import_top_data.m	Same as above, for data from the top of the head
f_estimate_LINEAR.m	Same as below, for Simple Linear Model
f_estimate_LINEAR_FandD.m	Same as below, for Modified Linear Model
f_estimate_INDOOR.m	Same as below, for Indoor Propagation Model
f_estimate.m	This function calculates the theoretical estimate with the MMSE estimated variables 'k' 'n' and 'm'. This estimate is based on the Modified Indoor Propagation model.
f_estimate_POLY.m	Same as above, for 2nd-Order Polynomial Model
f_estimate_MOD_POLY.m	Same as above, for Modified 2nd-Order Polynomial Model
f_MMSE_fit_LINEAR.m	Same as below, for Simple Linear Model
f_MMSE_fit_LINEAR_FandD.m	Same as below, for Modified Linear Model
f_MMSE_fit_INDOOR.m	Same as below, for Indoor Propagation Model
f_MMSE_fit_MOD_INDOOR.m	This function outputs variables 'k' 'n' and 'm' - three variables that are estimated in a MMSE type way. The variables 'b' and 'A' are piecewise generated matrices that represent the 'simulated losses' and the 'coefficients of the three variables,' respectively. 'x' represents the three variables and is estimated through the variable 'x_hat.'

m-file name	function
f_MMSE_fit_POLY.m	Same as above, for 2nd-Order Polynomial Model
f_MMSE_fit_MOD_POLY.m	Same as above, for Modified 2nd-Order Polynomial Model
LINEAR_fits.m	Same as below, for Simple Linear Model
LINEAR_FandD_fits.m	Same as below, for Modified Linear Model
INDOOR_fits.m	Same as below, for Indoor Propagation Model
MOD_INDOOR_fits.m	This script imports all transfer function data from all angles (top, side, front, back), converts these to magnitude (in dB) and then proceeds to fit each angle individually with a MMSE Modified Indoor Propagation model fit. The simulated curves and their estimates are then plotted in four individual plots.
POLY_fits.m	Same as above, for 2nd-Order Polynomial Model
MOD_POLY_fits.m	Same as above, for Modified 2nd-Order Polynomial Model
MULTIPLE_fits.m	This script imports all transfer function data from all angles (top, side, front, back), converts these to magnitude (in dB) and then proceeds to fit ALL THE DATA with a MMSE Modified Indoor Propagation Model fit. The simulated curves and their SINGLE ESTIMATE are then plotted in a single plot.
Plot3D.m	This script plots all the simulated transfer function magnitude data vs. frequency and distance in a 3D plot. The Poynting vector simulation plots are overlaid on this plot to show the correlation.
Power_Plots.m	2-D Version of the above m-file
Estimated_Transfer_... Functions_DISTANCE.m	This program uses the k n and m values as generated from the final MMSE estimation for all the data using the Modified Indoor Propagation Model fit to then estimate, for specific values of distance, what the transfer function would look like.
VARIOUS OTHER SCRIPTS	For other plotting or other quick calculations...

```
% Michael Pecoraro
% August, 2009
%
%   This function is used to import an input and output time domain signal
% and calculate the FFTs of each of them. Using this data, we output three
% main things: the time domain signals again (when plotted vs. t), the
```

```
% calculated frequency domain signals (when plotted vs. f_FFT), and the
% final transfer function (when plotted vs. f_FFT).

function [t, t_input, t_output, f_FFT, f_FFT_input, f_FFT_output, f_FFT_TF] =
f_extractTF(path1, path2, optionin, optionout)

% INPUTS:
%        path1: Path denoting location of 'input signal' data
%        path2: Path denoting location of 'output signal' data
%     optionin: Time [nsec], sets all data to 0 after this time, input sig
%    optionout: Time [nsec], sets all data to 0 after this time, output sig

% OUTPUTS:
%            t: Time vector used to calculate the FFTs, Transfer functions
%      t_input: Time domain input signal, when plotted vs. t
%     t_output: Time domain output signal, when plotted vs. t
%        f_FFT: Frequency vector generated through FFT setup
%  f_FFT_input: Frequency domain input signal, when plotted vs. f_FFT
% f_FFT_output: Frequency domain output signal, when plotted vs. f_FFT
%     f_FFT_TF: Frequency domain transfer function, when plotted vs. f_FFT

%% Import All Data
t_output_data = importdata( path2 , ' ' , 2 );

  % X-Axis, Time, in nsec
  to = t_output_data.data( : , 1 );
  to = to .' * ( 1e-9 );
  t = linspace(0,to(end),2000);

  % Y-Axis: Output Signal
  t_output = t_output_data.data( : , 2 ) .';
  t_output = interp1(to,t_output,t);
  if optionout ~= 0
      index =  find( t >= optionout*1e-9 );
      t_output( index ) = 0;
  end

t_input_data = importdata( path1 , ' ' , 2 );

  % X-Axis: Time, in nsec
  ti = t_input_data.data( : , 1 );
  ti = ti .' * ( 1e-9 );

  % Y-Axis: Input Signal
  t_input = t_input_data.data( : , 2 ) .';
  t_input = interp1(ti,t_input,t);
  index = find( isnan( t_input ) == 1 );
  t_input( index ) = 0;
  if optionin ~= 0
      index =  find( t >= optionin*1e-9 );
      t_input( index ) = 0;
  end

%% Performing Calculations for/of FFT Implementation
dt = t( 2 ) - t( 1 );
```

```
fs = 1 / dt;
n = nextpow2( 64 * length( t ) );
N = 2^n;
f_FFT = linspace( 0 , fs/2 , N/2 );

f_FFT_input = fft( t_input , N );
  f_FFT_input = f_FFT_input( 1:N/2 );
f_FFT_output = fft( t_output , N );
  f_FFT_output = f_FFT_output( 1:N/2 );

%% Calculating the Transfer Function
f_FFT_TF = ( f_FFT_output ) ./ ( f_FFT_input );

end
```

```
% Michael Pecoraro
% Tuesday, September 08, 2009
%
%   This script uses the f_extractTF() to output the transfer functions for
% each depth into the head from the left. The transfer function is output
% from this function as a complex number - if one would like to take the
% magnitude or phase, it must be done in the program that calls this
% function afterwards.

function ...
[f_FFT,...
 TF000, TF005, TF010, TF015, TF020,...
 TF025, TF030, TF035, TF040, TF045,...
 TF050, TF055, TF060, TF065, TF070,...
 TF075, TF080, TF085, TF090, TF095, TF100] = f_import_left_data()

% INPUTS:
%        NONE
%
% OUTPUTS:
%      f_FFT: Frequency vector generated through FFT setup. This value is
%             actually calculated in the f_extractTF() function.
%      TF###: These are the individual transfer functions where ### denotes
%             the distance for which the transfer function has been
%             calculated, in mm. Therefore: TF055 is the transfer function
%             for 55mm, or 5.5cm in the head.

% RUN RESULTS
[t    , t_input    , t_output    , ...
 f_FFT, f_FFT_input, f_FFT_output, TF000] = f_extractTF(...
    'C:\Documents and Settings\map2082\My Documents\Downloads\Head Data\Head
Data\01 Left Side\E_000mm.txt',...
    'C:\Documents and Settings\map2082\My Documents\Downloads\Head Data\Head
Data\01 Left Side\E_000mm.txt',0,0);

[t    , t_input    , t_output    , ...
 f_FFT, f_FFT_input, f_FFT_output, TF005] = f_extractTF(...
    'C:\Documents and Settings\map2082\My Documents\Downloads\Head Data\Head
Data\01 Left Side\E_000mm.txt',...
```

```
    'C:\Documents and Settings\map2082\My Documents\Downloads\Head Data\Head
Data\01 Left Side\E_005mm.txt',0,0);

[t    , t_input    , t_output    , ...
 f_FFT, f_FFT_input, f_FFT_output, TF010] = f_extractTF(...
    'C:\Documents and Settings\map2082\My Documents\Downloads\Head Data\Head
Data\01 Left Side\E_000mm.txt',...
    'C:\Documents and Settings\map2082\My Documents\Downloads\Head Data\Head
Data\01 Left Side\E_010mm.txt',0,0);

[t    , t_input    , t_output    , ...
 f_FFT, f_FFT_input, f_FFT_output, TF015] = f_extractTF(...
    'C:\Documents and Settings\map2082\My Documents\Downloads\Head Data\Head
Data\01 Left Side\E_000mm.txt',...
    'C:\Documents and Settings\map2082\My Documents\Downloads\Head Data\Head
Data\01 Left Side\E_015mm.txt',0,0);

[t    , t_input    , t_output    , ...
 f_FFT, f_FFT_input, f_FFT_output, TF020] = f_extractTF(...
    'C:\Documents and Settings\map2082\My Documents\Downloads\Head Data\Head
Data\01 Left Side\E_000mm.txt',...
    'C:\Documents and Settings\map2082\My Documents\Downloads\Head Data\Head
Data\01 Left Side\E_020mm.txt',0,0);

[t    , t_input    , t_output    , ...
 f_FFT, f_FFT_input, f_FFT_output, TF025] = f_extractTF(...
    'C:\Documents and Settings\map2082\My Documents\Downloads\Head Data\Head
Data\01 Left Side\E_000mm.txt',...
    'C:\Documents and Settings\map2082\My Documents\Downloads\Head Data\Head
Data\01 Left Side\E_025mm.txt',0,0);

[t    , t_input    , t_output    , ...
 f_FFT, f_FFT_input, f_FFT_output, TF030] = f_extractTF(...
    'C:\Documents and Settings\map2082\My Documents\Downloads\Head Data\Head
Data\01 Left Side\E_000mm.txt',...
    'C:\Documents and Settings\map2082\My Documents\Downloads\Head Data\Head
Data\01 Left Side\E_030mm.txt',0,0);

[t    , t_input    , t_output    , ...
 f_FFT, f_FFT_input, f_FFT_output, TF035] = f_extractTF(...
    'C:\Documents and Settings\map2082\My Documents\Downloads\Head Data\Head
Data\01 Left Side\E_000mm.txt',...
    'C:\Documents and Settings\map2082\My Documents\Downloads\Head Data\Head
Data\01 Left Side\E_035mm.txt',0,0);

[t    , t_input    , t_output    , ...
 f_FFT, f_FFT_input, f_FFT_output, TF040] = f_extractTF(...
    'C:\Documents and Settings\map2082\My Documents\Downloads\Head Data\Head
Data\01 Left Side\E_000mm.txt',...
    'C:\Documents and Settings\map2082\My Documents\Downloads\Head Data\Head
Data\01 Left Side\E_040mm.txt',0,0);

[t    , t_input    , t_output    , ...
 f_FFT, f_FFT_input, f_FFT_output, TF045] = f_extractTF(...
    'C:\Documents and Settings\map2082\My Documents\Downloads\Head Data\Head
```

```
Data\01 Left Side\E_000mm.txt',...
    'C:\Documents and Settings\map2082\My Documents\Downloads\Head Data\Head
Data\01 Left Side\E_045mm.txt',0,0);

[t    , t_input    , t_output    , ...
 f_FFT, f_FFT_input, f_FFT_output, TF050] = f_extractTF(...
    'C:\Documents and Settings\map2082\My Documents\Downloads\Head Data\Head
Data\01 Left Side\E_000mm.txt',...
    'C:\Documents and Settings\map2082\My Documents\Downloads\Head Data\Head
Data\01 Left Side\E_050mm.txt',0,0);

[t    , t_input    , t_output    , ...
 f_FFT, f_FFT_input, f_FFT_output, TF055] = f_extractTF(...
    'C:\Documents and Settings\map2082\My Documents\Downloads\Head Data\Head
Data\01 Left Side\E_000mm.txt',...
    'C:\Documents and Settings\map2082\My Documents\Downloads\Head Data\Head
Data\01 Left Side\E_055mm.txt',0,0);

[t    , t_input    , t_output    , ...
 f_FFT, f_FFT_input, f_FFT_output, TF060] = f_extractTF(...
    'C:\Documents and Settings\map2082\My Documents\Downloads\Head Data\Head
Data\01 Left Side\E_000mm.txt',...
    'C:\Documents and Settings\map2082\My Documents\Downloads\Head Data\Head
Data\01 Left Side\E_060mm.txt',0,0);

[t    , t_input    , t_output    , ...
 f_FFT, f_FFT_input, f_FFT_output, TF065] = f_extractTF(...
    'C:\Documents and Settings\map2082\My Documents\Downloads\Head Data\Head
Data\01 Left Side\E_000mm.txt',...
    'C:\Documents and Settings\map2082\My Documents\Downloads\Head Data\Head
Data\01 Left Side\E_065mm.txt',0,0);

[t    , t_input    , t_output    , ...
 f_FFT, f_FFT_input, f_FFT_output, TF070] = f_extractTF(...
    'C:\Documents and Settings\map2082\My Documents\Downloads\Head Data\Head
Data\01 Left Side\E_000mm.txt',...
    'C:\Documents and Settings\map2082\My Documents\Downloads\Head Data\Head
Data\01 Left Side\E_070mm.txt',0,0);
[t    , t_input    , t_output    , ...
 f_FFT, f_FFT_input, f_FFT_output, TF075] = f_extractTF(...
    'C:\Documents and Settings\map2082\My Documents\Downloads\Head Data\Head
Data\01 Left Side\E_000mm.txt',...
    'C:\Documents and Settings\map2082\My Documents\Downloads\Head Data\Head
Data\01 Left Side\E_075mm.txt',0,0);

[t    , t_input    , t_output    , ...
 f_FFT, f_FFT_input, f_FFT_output, TF080] = f_extractTF(...
    'C:\Documents and Settings\map2082\My Documents\Downloads\Head Data\Head
Data\01 Left Side\E_000mm.txt',...
    'C:\Documents and Settings\map2082\My Documents\Downloads\Head Data\Head
Data\01 Left Side\E_080mm.txt',0,0);

[t    , t_input    , t_output    , ...
 f_FFT, f_FFT_input, f_FFT_output, TF085] = f_extractTF(...
    'C:\Documents and Settings\map2082\My Documents\Downloads\Head Data\Head
```

```
Data\01 Left Side\E_000mm.txt',...
    'C:\Documents and Settings\map2082\My Documents\Downloads\Head Data\Head
Data\01 Left Side\E_085mm.txt',0,0);

[t    , t_input    , t_output    , ...
 f_FFT, f_FFT_input, f_FFT_output, TF090] = f_extractTF(...
    'C:\Documents and Settings\map2082\My Documents\Downloads\Head Data\Head
Data\01 Left Side\E_000mm.txt',...
    'C:\Documents and Settings\map2082\My Documents\Downloads\Head Data\Head
Data\01 Left Side\E_090mm.txt',0,0);

[t    , t_input    , t_output    , ...
 f_FFT, f_FFT_input, f_FFT_output, TF095] = f_extractTF(...
    'C:\Documents and Settings\map2082\My Documents\Downloads\Head Data\Head
Data\01 Left Side\E_000mm.txt',...
    'C:\Documents and Settings\map2082\My Documents\Downloads\Head Data\Head
Data\01 Left Side\E_095mm.txt',0,0);

[t    , t_input    , t_output    , ...
 f_FFT, f_FFT_input, f_FFT_output, TF100] = f_extractTF(...
    'C:\Documents and Settings\map2082\My Documents\Downloads\Head Data\Head
Data\01 Left Side\E_000mm.txt',...
    'C:\Documents and Settings\map2082\My Documents\Downloads\Head Data\Head
Data\01 Left Side\E_100mm.txt',0,0);

end
```

```
% Michael Pecoraro
% October, 2009
%
%   This function calculates the theoretical estimate with the MMSE
% estimated variables 'k' 'n' and 'm'. This estimate is based on the
% Modified Indoor Propagation model.

function [est] = f_estimate(f,d,k,n,m,d0,f0)

% INPUTS:
%        f: Frequencies over which the function will be evaluated.
%        d: Single distance value for which the function will be evaluated.
%        k: Value of the 'k' parameter, estimated through MMSE techniques
%        n: Value of the 'n' parameter, estimated through MMSE techniques
%        m: Value of the 'm' parameter, estimated through MMSE techniques
%       d0: Arbitrary value of 'initial' distance - should be the same as the
%           d0 used in the estimation of all k, n, and m parameters.
%        f0: Arbitrary value of 'initial' frequency - should be the same as
the
%           f0 used in the estimation of all k, n, and m parameters.

% OUTPUTS:
%      est: Estimated transfer function magnitude for the specific frequency
%           range and distance that were input.

est = k*(d/d0) - n*(10*log10(d/d0)).*(f/f0) - m*(10*log10(f/f0)).*(d/d0);
```

```
end
```

```
% Michael Pecoraro
% October, 2009
%
%   This function outputs variables 'k' 'n' and 'm' - three variables that
% are estimated in a MMSE type way. The variables 'b' and 'A' are piecewise
% generated matrices that represent the 'simulated losses'and the
% 'coefficients of the three variables,' respectively. 'x' represents the
% three variables and is estimated through the variable 'x_hat.'

function [k n m MMSE] = f_MMSE_fit_MOD_INDOOR(D_matrix,d0,d,f0,f)

% INPUTS:
% D_matrix: Frequencies over which the function will be evaluated.
%       d0: Arbitrary value of 'initial' distance - should be the same as the
%           d0 used in the estimation of all k, n, and m parameters.
%        d: Distances corresponding to each of the D_matrix columns
%        f0: Arbitrary value of 'initial' frequency - should be the same as
the
%           f0 used in the estimation of all k, n, and m parameters.
%        f: Frequencies over which the fit will be performed

% OUTPUTS:
%        k: Estimated 'k' value
%        n: Estimated 'n' value
%        m: Estimated 'm' value
%     MMSE: The Minimum Mean Squared Error for the estimated fit

%% Calculations
N = size(D_matrix,2);

% Setting up blank variables.
b = [];
dVert = [];
freqVert = [];

for i = 1:N
    b = [b; D_matrix(:,i)];               % Simulated values per distance
    dVert = [dVert; d(i)*ones(size(f'))]; % Column of distance for which the
values were obtained
    freqVert = [freqVert; f'];              % Column of frequencies for which
the values were obtained
end

A1 = ones(size(b))   .*(dVert/d0);
A2 = -10*log10(dVert/d0).*(freqVert/f0);
A3 = -10*log10(freqVert/f0).*(dVert/d0);
A = [A1 A2 A3]; % Coefficients of the variables in the model equation

x_hat = inv(A'*A) * (A'*b); % Formula to estimate the variables

k = x_hat(1);
n = x_hat(2);
```

```
m = x_hat(3);

MMSE = (A*x_hat - b).' * (A*x_hat - b); % Formula for MMSE

end
```

```
% Michael Pecoraro
% November, 2009
%
%   This script imports all transfer function data from all angles (top,
% side, front, back), converts these to magnitude (in dB) and then proceeds
% to fit each angle individually with a MMSE Modified Indoor Propagation
% model fit.
%   The simulated curves and their estimates are then plotted in four
% individual plots.

clc
clear
close all

frequency = (300e6:1e6:3000e6); % X axis points

%% IMPORTING
% IMPORTING LEFT SIDE DATA
[f_FFT,...
 TF000, TF005, TF010, TF015, TF020,...
 TF025, TF030, TF035, TF040, TF045,...
 TF050, TF055, TF060, TF065, TF070,...
 TF075, TF080, TF085, TF090, TF095, TF100] = f_import_left_data();

iTF000l = 20*log10(abs(interp1(f_FFT,TF000,frequency)));
iTF005l = 20*log10(abs(interp1(f_FFT,TF005,frequency)));
iTF010l = 20*log10(abs(interp1(f_FFT,TF010,frequency)));
iTF015l = 20*log10(abs(interp1(f_FFT,TF015,frequency)));
iTF020l = 20*log10(abs(interp1(f_FFT,TF020,frequency)));
iTF025l = 20*log10(abs(interp1(f_FFT,TF025,frequency)));
iTF030l = 20*log10(abs(interp1(f_FFT,TF030,frequency)));
iTF035l = 20*log10(abs(interp1(f_FFT,TF035,frequency)));
iTF040l = 20*log10(abs(interp1(f_FFT,TF040,frequency)));
iTF045l = 20*log10(abs(interp1(f_FFT,TF045,frequency)));
iTF050l = 20*log10(abs(interp1(f_FFT,TF050,frequency)));
iTF055l = 20*log10(abs(interp1(f_FFT,TF055,frequency)));
iTF060l = 20*log10(abs(interp1(f_FFT,TF060,frequency)));
iTF065l = 20*log10(abs(interp1(f_FFT,TF065,frequency)));
iTF070l = 20*log10(abs(interp1(f_FFT,TF070,frequency)));
iTF075l = 20*log10(abs(interp1(f_FFT,TF075,frequency)));
iTF080l = 20*log10(abs(interp1(f_FFT,TF080,frequency)));
iTF085l = 20*log10(abs(interp1(f_FFT,TF085,frequency)));
iTF090l = 20*log10(abs(interp1(f_FFT,TF090,frequency)));
iTF095l = 20*log10(abs(interp1(f_FFT,TF095,frequency)));
iTF100l = 20*log10(abs(interp1(f_FFT,TF100,frequency)));

% ORGANIZING LEFT SIDE DATA
D_matrixl   =   [   iTF020l'   iTF030l'   iTF040l'   iTF050l'   iTF060l'   iTF070l'
```

```
iTF080l'];
dl          = [ 0.020     0.030     0.040     0.050     0.060     0.070     0.080
];


% IMPORTING BACK DATA
[f_FFT,...
 TF000, TF005, TF010, TF015, TF020,...
 TF025, TF030, TF035, TF040, TF045,...
 TF050, TF055, TF060, TF065, TF070,...
 TF075, TF080, TF085, TF090, TF095, TF100] = f_import_back_data();

iTF000b = 20*log10(abs(interp1(f_FFT,TF000,frequency)));
iTF005b = 20*log10(abs(interp1(f_FFT,TF005,frequency)));
iTF010b = 20*log10(abs(interp1(f_FFT,TF010,frequency)));
iTF015b = 20*log10(abs(interp1(f_FFT,TF015,frequency)));
iTF020b = 20*log10(abs(interp1(f_FFT,TF020,frequency)));
iTF025b = 20*log10(abs(interp1(f_FFT,TF025,frequency)));
iTF030b = 20*log10(abs(interp1(f_FFT,TF030,frequency)));
iTF035b = 20*log10(abs(interp1(f_FFT,TF035,frequency)));
iTF040b = 20*log10(abs(interp1(f_FFT,TF040,frequency)));
iTF045b = 20*log10(abs(interp1(f_FFT,TF045,frequency)));
iTF050b = 20*log10(abs(interp1(f_FFT,TF050,frequency)));
iTF055b = 20*log10(abs(interp1(f_FFT,TF055,frequency)));
iTF060b = 20*log10(abs(interp1(f_FFT,TF060,frequency)));
iTF065b = 20*log10(abs(interp1(f_FFT,TF065,frequency)));
iTF070b = 20*log10(abs(interp1(f_FFT,TF070,frequency)));
iTF075b = 20*log10(abs(interp1(f_FFT,TF075,frequency)));
iTF080b = 20*log10(abs(interp1(f_FFT,TF080,frequency)));
iTF085b = 20*log10(abs(interp1(f_FFT,TF085,frequency)));
iTF090b = 20*log10(abs(interp1(f_FFT,TF090,frequency)));
iTF095b = 20*log10(abs(interp1(f_FFT,TF095,frequency)));
iTF100b = 20*log10(abs(interp1(f_FFT,TF100,frequency)));

% ORGANIZING BACK DATA
D_matrixb  =  [  iTF020b'  iTF030b'  iTF040b'  iTF050b'  iTF060b'  iTF070b'
iTF080b'];
db          = [ 0.020     0.030     0.040     0.050     0.060     0.070     0.080
];


% IMPORTING TOP DATA
[f_FFT,...
 TF000, TF005, TF010, TF015, TF020,...
 TF025, TF030, TF035, TF040, TF045,...
 TF050, TF055, TF060, TF065, TF070,...
 TF075, TF080, TF085, TF090, TF095, TF100] = f_import_top_data();

iTF000t = 20*log10(abs(interp1(f_FFT,TF000,frequency)));
iTF005t = 20*log10(abs(interp1(f_FFT,TF005,frequency)));
iTF010t = 20*log10(abs(interp1(f_FFT,TF010,frequency)));
iTF015t = 20*log10(abs(interp1(f_FFT,TF015,frequency)));
iTF020t = 20*log10(abs(interp1(f_FFT,TF020,frequency)));
iTF025t = 20*log10(abs(interp1(f_FFT,TF025,frequency)));
iTF030t = 20*log10(abs(interp1(f_FFT,TF030,frequency)));
```

```
iTF035t = 20*log10(abs(interp1(f_FFT,TF035,frequency)));
iTF040t = 20*log10(abs(interp1(f_FFT,TF040,frequency)));
iTF045t = 20*log10(abs(interp1(f_FFT,TF045,frequency)));
iTF050t = 20*log10(abs(interp1(f_FFT,TF050,frequency)));
iTF055t = 20*log10(abs(interp1(f_FFT,TF055,frequency)));
iTF060t = 20*log10(abs(interp1(f_FFT,TF060,frequency)));
iTF065t = 20*log10(abs(interp1(f_FFT,TF065,frequency)));
iTF070t = 20*log10(abs(interp1(f_FFT,TF070,frequency)));
iTF075t = 20*log10(abs(interp1(f_FFT,TF075,frequency)));
iTF080t = 20*log10(abs(interp1(f_FFT,TF080,frequency)));
iTF085t = 20*log10(abs(interp1(f_FFT,TF085,frequency)));
iTF090t = 20*log10(abs(interp1(f_FFT,TF090,frequency)));
iTF095t = 20*log10(abs(interp1(f_FFT,TF095,frequency)));
iTF100t = 20*log10(abs(interp1(f_FFT,TF100,frequency)));

% ORGANIZING TOP DATA
D_matrixt   =   [   iTF020t'   iTF030t'   iTF040t'   iTF050t'   iTF060t'   iTF070t'
iTF080t'];
dt          = [ 0.020     0.030     0.040     0.050     0.060     0.070     0.080
];



% IMPORTING FRONT DATA
[f_FFT,...
 TF000, TF005, TF010, TF015, TF020,...
 TF025, TF030, TF035, TF040, TF045,...
 TF050, TF055, TF060, TF065, TF070,...
 TF075, TF080, TF085, TF090, TF095, TF100] = f_import_front_data();

iTF000f = 20*log10(abs(interp1(f_FFT,TF000,frequency)));
iTF005f = 20*log10(abs(interp1(f_FFT,TF005,frequency)));
iTF010f = 20*log10(abs(interp1(f_FFT,TF010,frequency)));
iTF015f = 20*log10(abs(interp1(f_FFT,TF015,frequency)));
iTF020f = 20*log10(abs(interp1(f_FFT,TF020,frequency)));
iTF025f = 20*log10(abs(interp1(f_FFT,TF025,frequency)));
iTF030f = 20*log10(abs(interp1(f_FFT,TF030,frequency)));
iTF035f = 20*log10(abs(interp1(f_FFT,TF035,frequency)));
iTF040f = 20*log10(abs(interp1(f_FFT,TF040,frequency)));
iTF045f = 20*log10(abs(interp1(f_FFT,TF045,frequency)));
iTF050f = 20*log10(abs(interp1(f_FFT,TF050,frequency)));
iTF055f = 20*log10(abs(interp1(f_FFT,TF055,frequency)));
iTF060f = 20*log10(abs(interp1(f_FFT,TF060,frequency)));
iTF065f = 20*log10(abs(interp1(f_FFT,TF065,frequency)));
iTF070f = 20*log10(abs(interp1(f_FFT,TF070,frequency)));
iTF075f = 20*log10(abs(interp1(f_FFT,TF075,frequency)));
iTF080f = 20*log10(abs(interp1(f_FFT,TF080,frequency)));
iTF085f = 20*log10(abs(interp1(f_FFT,TF085,frequency)));
iTF090f = 20*log10(abs(interp1(f_FFT,TF090,frequency)));
iTF095f = 20*log10(abs(interp1(f_FFT,TF095,frequency)));
iTF100f = 20*log10(abs(interp1(f_FFT,TF100,frequency)));

% ORGANIZING FRONT DATA
D_matrixf   =   [   iTF020f'   iTF030f'   iTF040f'   iTF050f'   iTF060f'   iTF070f'
iTF080f'];
df          = [ 0.020     0.030     0.040     0.050     0.060     0.070     0.080
];
```

```
clear TF*

%% Fitting
d0 = 0.02;
f0 = 250e6;

[k_b n_b m_b MMSE_b] = f_MMSE_fit_MOD_INDOOR(D_matrixb,d0,db,f0,frequency);
ave_b = sqrt(MMSE_b/length(frequency)/length(db));
disp(['k_b = ' num2str(k_b)]);
disp(['n_b = ' num2str(n_b)]);
disp(['m_b = ' num2str(m_b)]);
disp(['sigma_b = ' num2str(ave_b)]);
disp(' ');

[k_l n_l m_l MMSE_l] = f_MMSE_fit_MOD_INDOOR(D_matrixl,d0,dl,f0,frequency);
ave_l = sqrt(MMSE_l/length(frequency)/length(dl));
disp(['k_l = ' num2str(k_l)]);
disp(['n_l = ' num2str(n_l)]);
disp(['m_l = ' num2str(m_l)]);
disp(['sigma_l = ' num2str(ave_l)]);
disp(' ');

[k_f n_f m_f MMSE_f] = f_MMSE_fit_MOD_INDOOR(D_matrixf,d0,df,f0,frequency);
ave_f = sqrt(MMSE_f/length(frequency)/length(df));
disp(['k_f = ' num2str(k_f)]);
disp(['n_f = ' num2str(n_f)]);
disp(['m_f = ' num2str(m_f)]);
disp(['sigma_f = ' num2str(ave_f)]);
disp(' ');

[k_t n_t m_t MMSE_t] = f_MMSE_fit_MOD_INDOOR(D_matrixt,d0,dt,f0,frequency);
ave_t = sqrt(MMSE_t/length(frequency)/length(dt));
disp(['k_t = ' num2str(k_t)]);
disp(['n_t = ' num2str(n_t)]);
disp(['m_t = ' num2str(m_t)]);
disp(['sigma_t = ' num2str(ave_t)]);
disp(' ');


%% PLOTTING
colors = jet(7);
%_____________________LEFT
figure;
hold on;
plot(frequency, iTF020l,':','LineWidth',3.5,'Color',colors(1,:));
plot(frequency, iTF030l,':','LineWidth',3.5,'Color',colors(2,:));
plot(frequency, iTF040l,':','LineWidth',3.5,'Color',colors(3,:));
plot(frequency, iTF050l,':','LineWidth',3.5,'Color',colors(4,:));
plot(frequency, iTF060l,':','LineWidth',3.5,'Color',colors(5,:));
plot(frequency, iTF070l,':','LineWidth',3.5,'Color',colors(6,:));
plot(frequency, iTF080l,':','LineWidth',3.5,'Color',colors(7,:));
hold off;

f = linspace(300e6,3000e6,2000);
```

```
hold on;
plot(f,f_estimate(f,0.020,k_l,n_l,m_l,d0,f0),'k','LineWidth',3)
plot(f,f_estimate(f,0.030,k_l,n_l,m_l,d0,f0),'k','LineWidth',3)
plot(f,f_estimate(f,0.040,k_l,n_l,m_l,d0,f0),'k','LineWidth',3)
plot(f,f_estimate(f,0.050,k_l,n_l,m_l,d0,f0),'k','LineWidth',3)
plot(f,f_estimate(f,0.060,k_l,n_l,m_l,d0,f0),'k','LineWidth',3)
plot(f,f_estimate(f,0.070,k_l,n_l,m_l,d0,f0),'k','LineWidth',3)
plot(f,f_estimate(f,0.080,k_l,n_l,m_l,d0,f0),'k','LineWidth',3)
hold off;

set(gca,'XLim',[300e6 3e9]);
set(gca,'YLim',[-90 10]);
title({'Estimated Transfer Function Magnitude vs. Frequency';'Modified Indoor
Propagation Model';...
       'Into Brain from Left'},'FontWeight','bold');
xlabel('Frequency [Hz]');
ylabel('Magnitude [dB]');
grid on;

%_____________________BACK
figure;
hold on;
plot(frequency, iTF020b,':','LineWidth',3.5,'Color',colors(1,:));
plot(frequency, iTF030b,':','LineWidth',3.5,'Color',colors(2,:));
plot(frequency, iTF040b,':','LineWidth',3.5,'Color',colors(3,:));
plot(frequency, iTF050b,':','LineWidth',3.5,'Color',colors(4,:));
plot(frequency, iTF060b,':','LineWidth',3.5,'Color',colors(5,:));
plot(frequency, iTF070b,':','LineWidth',3.5,'Color',colors(6,:));
plot(frequency, iTF080b,':','LineWidth',3.5,'Color',colors(7,:));
hold off;

f = linspace(300e6,3000e6,2000);

hold on;
plot(f,f_estimate(f,0.020,k_b,n_b,m_b,d0,f0),'k','LineWidth',3)
plot(f,f_estimate(f,0.030,k_b,n_b,m_b,d0,f0),'k','LineWidth',3)
plot(f,f_estimate(f,0.040,k_b,n_b,m_b,d0,f0),'k','LineWidth',3)
plot(f,f_estimate(f,0.050,k_b,n_b,m_b,d0,f0),'k','LineWidth',3)
plot(f,f_estimate(f,0.060,k_b,n_b,m_b,d0,f0),'k','LineWidth',3)
plot(f,f_estimate(f,0.070,k_b,n_b,m_b,d0,f0),'k','LineWidth',3)
plot(f,f_estimate(f,0.080,k_b,n_b,m_b,d0,f0),'k','LineWidth',3)
hold off;

set(gca,'XLim',[300e6 3e9]);
set(gca,'YLim',[-90 10]);
title({'Estimated Transfer Function Magnitude vs. Frequency';'Modified Indoor
Propagation Model';...
       'Into Brain from Back'},'FontWeight','bold');
xlabel('Frequency [Hz]');
ylabel('Magnitude [dB]');
grid on;

%_____________________FRONT
figure;
```

```
hold on;
plot(frequency, iTF020f,':','LineWidth',3.5,'Color',colors(1,:));
plot(frequency, iTF030f,':','LineWidth',3.5,'Color',colors(2,:));
plot(frequency, iTF040f,':','LineWidth',3.5,'Color',colors(3,:));
plot(frequency, iTF050f,':','LineWidth',3.5,'Color',colors(4,:));
plot(frequency, iTF060f,':','LineWidth',3.5,'Color',colors(5,:));
plot(frequency, iTF070f,':','LineWidth',3.5,'Color',colors(6,:));
plot(frequency, iTF080f,':','LineWidth',3.5,'Color',colors(7,:));
hold off;

f = linspace(300e6,3000e6,2000);

hold on;
plot(f,f_estimate(f,0.020,k_f,n_f,m_f,d0,f0),'k','LineWidth',3)
plot(f,f_estimate(f,0.030,k_f,n_f,m_f,d0,f0),'k','LineWidth',3)
plot(f,f_estimate(f,0.040,k_f,n_f,m_f,d0,f0),'k','LineWidth',3)
plot(f,f_estimate(f,0.050,k_f,n_f,m_f,d0,f0),'k','LineWidth',3)
plot(f,f_estimate(f,0.060,k_f,n_f,m_f,d0,f0),'k','LineWidth',3)
plot(f,f_estimate(f,0.070,k_f,n_f,m_f,d0,f0),'k','LineWidth',3)
plot(f,f_estimate(f,0.080,k_f,n_f,m_f,d0,f0),'k','LineWidth',3)
hold off;

set(gca,'XLim',[300e6 3e9]);
set(gca,'YLim',[-90 10]);
title({'Estimated Transfer Function Magnitude vs. Frequency';'Modified Indoor
Propagation Model';...
       'Into Brain from Front'},'FontWeight','bold');
xlabel('Frequency [Hz]');
ylabel('Magnitude [dB]');
grid on;

%_____________________TOP
figure;
hold on;
plot(frequency, iTF020t,':','LineWidth',3.5,'Color',colors(1,:));
plot(frequency, iTF030t,':','LineWidth',3.5,'Color',colors(2,:));
plot(frequency, iTF040t,':','LineWidth',3.5,'Color',colors(3,:));
plot(frequency, iTF050t,':','LineWidth',3.5,'Color',colors(4,:));
plot(frequency, iTF060t,':','LineWidth',3.5,'Color',colors(5,:));
plot(frequency, iTF070t,':','LineWidth',3.5,'Color',colors(6,:));
plot(frequency, iTF080t,':','LineWidth',3.5,'Color',colors(7,:));
hold off;

f = linspace(300e6,3000e6,2000);

hold on;
plot(f,f_estimate(f,0.020,k_t,n_t,m_t,d0,f0),'k','LineWidth',3)
plot(f,f_estimate(f,0.030,k_t,n_t,m_t,d0,f0),'k','LineWidth',3)
plot(f,f_estimate(f,0.040,k_t,n_t,m_t,d0,f0),'k','LineWidth',3)
plot(f,f_estimate(f,0.050,k_t,n_t,m_t,d0,f0),'k','LineWidth',3)
plot(f,f_estimate(f,0.060,k_t,n_t,m_t,d0,f0),'k','LineWidth',3)
plot(f,f_estimate(f,0.070,k_t,n_t,m_t,d0,f0),'k','LineWidth',3)
plot(f,f_estimate(f,0.080,k_t,n_t,m_t,d0,f0),'k','LineWidth',3)
hold off;
```

```
set(gca,'XLim',[300e6 3e9]);
set(gca,'YLim',[-90 10]);
title({'Estimated Transfer Function Magnitude vs. Frequency';'Modified Indoor
Propagation Model';...
       'Into Brain from Top'},'FontWeight','bold');
xlabel('Frequency [Hz]');
ylabel('Magnitude [dB]');
grid on;
```

```
% Michael Pecoraro
% November, 2009
%
%   This script imports all transfer function data from all angles (top,
% side, front, back), converts these to magnitude (in dB) and then proceeds
% to fit ALL THE DATA with a MMSE Modified Indoor Propagation Model fit.
%   The simulated curves and their SINGLE ESTIMATE are then plotted in a
% single plot.

clc
clear
close all

frequency = (300e6:1e6:3000e6); % X axis points

%% IMPORTING
% IMPORTING LEFT SIDE DATA
[f_FFT,...
 TF000, TF005, TF010, TF015, TF020,...
 TF025, TF030, TF035, TF040, TF045,...
 TF050, TF055, TF060, TF065, TF070,...
 TF075, TF080, TF085, TF090, TF095, TF100] = f_import_left_data();

iTF000l = 20*log10(abs(interp1(f_FFT,TF000,frequency)));
iTF005l = 20*log10(abs(interp1(f_FFT,TF005,frequency)));
iTF010l = 20*log10(abs(interp1(f_FFT,TF010,frequency)));
iTF015l = 20*log10(abs(interp1(f_FFT,TF015,frequency)));
iTF020l = 20*log10(abs(interp1(f_FFT,TF020,frequency)));
iTF025l = 20*log10(abs(interp1(f_FFT,TF025,frequency)));
iTF030l = 20*log10(abs(interp1(f_FFT,TF030,frequency)));
iTF035l = 20*log10(abs(interp1(f_FFT,TF035,frequency)));
iTF040l = 20*log10(abs(interp1(f_FFT,TF040,frequency)));
iTF045l = 20*log10(abs(interp1(f_FFT,TF045,frequency)));
iTF050l = 20*log10(abs(interp1(f_FFT,TF050,frequency)));
iTF055l = 20*log10(abs(interp1(f_FFT,TF055,frequency)));
iTF060l = 20*log10(abs(interp1(f_FFT,TF060,frequency)));
iTF065l = 20*log10(abs(interp1(f_FFT,TF065,frequency)));
iTF070l = 20*log10(abs(interp1(f_FFT,TF070,frequency)));
iTF075l = 20*log10(abs(interp1(f_FFT,TF075,frequency)));
iTF080l = 20*log10(abs(interp1(f_FFT,TF080,frequency)));
iTF085l = 20*log10(abs(interp1(f_FFT,TF085,frequency)));
iTF090l = 20*log10(abs(interp1(f_FFT,TF090,frequency)));
iTF095l = 20*log10(abs(interp1(f_FFT,TF095,frequency)));
iTF100l = 20*log10(abs(interp1(f_FFT,TF100,frequency)));
```

```
% ORGANIZING LEFT SIDE DATA
D_matrixl   =   [  iTF020l'  iTF030l'  iTF040l'  iTF050l'  iTF060l'  iTF070l'
iTF080l'];
dl          = [ 0.020     0.030     0.040     0.050     0.060     0.070     0.080
];



% IMPORTING BACK DATA
[f_FFT,...
 TF000, TF005, TF010, TF015, TF020,...
 TF025, TF030, TF035, TF040, TF045,...
 TF050, TF055, TF060, TF065, TF070,...
 TF075, TF080, TF085, TF090, TF095, TF100] = f_import_back_data();

iTF000b = 20*log10(abs(interp1(f_FFT,TF000,frequency)));
iTF005b = 20*log10(abs(interp1(f_FFT,TF005,frequency)));
iTF010b = 20*log10(abs(interp1(f_FFT,TF010,frequency)));
iTF015b = 20*log10(abs(interp1(f_FFT,TF015,frequency)));
iTF020b = 20*log10(abs(interp1(f_FFT,TF020,frequency)));
iTF025b = 20*log10(abs(interp1(f_FFT,TF025,frequency)));
iTF030b = 20*log10(abs(interp1(f_FFT,TF030,frequency)));
iTF035b = 20*log10(abs(interp1(f_FFT,TF035,frequency)));
iTF040b = 20*log10(abs(interp1(f_FFT,TF040,frequency)));
iTF045b = 20*log10(abs(interp1(f_FFT,TF045,frequency)));
iTF050b = 20*log10(abs(interp1(f_FFT,TF050,frequency)));
iTF055b = 20*log10(abs(interp1(f_FFT,TF055,frequency)));
iTF060b = 20*log10(abs(interp1(f_FFT,TF060,frequency)));
iTF065b = 20*log10(abs(interp1(f_FFT,TF065,frequency)));
iTF070b = 20*log10(abs(interp1(f_FFT,TF070,frequency)));
iTF075b = 20*log10(abs(interp1(f_FFT,TF075,frequency)));
iTF080b = 20*log10(abs(interp1(f_FFT,TF080,frequency)));
iTF085b = 20*log10(abs(interp1(f_FFT,TF085,frequency)));
iTF090b = 20*log10(abs(interp1(f_FFT,TF090,frequency)));
iTF095b = 20*log10(abs(interp1(f_FFT,TF095,frequency)));
iTF100b = 20*log10(abs(interp1(f_FFT,TF100,frequency)));

% ORGANIZING BACK DATA
D_matrixb   =   [  iTF020b'  iTF030b'  iTF040b'  iTF050b'  iTF060b'  iTF070b'
iTF080b'];
db          = [ 0.020     0.030     0.040     0.050     0.060     0.070     0.080
];



% IMPORTING TOP DATA
[f_FFT,...
 TF000, TF005, TF010, TF015, TF020,...
 TF025, TF030, TF035, TF040, TF045,...
 TF050, TF055, TF060, TF065, TF070,...
 TF075, TF080, TF085, TF090, TF095, TF100] = f_import_top_data();

iTF000t = 20*log10(abs(interp1(f_FFT,TF000,frequency)));
iTF005t = 20*log10(abs(interp1(f_FFT,TF005,frequency)));
iTF010t = 20*log10(abs(interp1(f_FFT,TF010,frequency)));
iTF015t = 20*log10(abs(interp1(f_FFT,TF015,frequency)));
iTF020t = 20*log10(abs(interp1(f_FFT,TF020,frequency)));
```

```
iTF025t = 20*log10(abs(interp1(f_FFT,TF025,frequency)));
iTF030t = 20*log10(abs(interp1(f_FFT,TF030,frequency)));
iTF035t = 20*log10(abs(interp1(f_FFT,TF035,frequency)));
iTF040t = 20*log10(abs(interp1(f_FFT,TF040,frequency)));
iTF045t = 20*log10(abs(interp1(f_FFT,TF045,frequency)));
iTF050t = 20*log10(abs(interp1(f_FFT,TF050,frequency)));
iTF055t = 20*log10(abs(interp1(f_FFT,TF055,frequency)));
iTF060t = 20*log10(abs(interp1(f_FFT,TF060,frequency)));
iTF065t = 20*log10(abs(interp1(f_FFT,TF065,frequency)));
iTF070t = 20*log10(abs(interp1(f_FFT,TF070,frequency)));
iTF075t = 20*log10(abs(interp1(f_FFT,TF075,frequency)));
iTF080t = 20*log10(abs(interp1(f_FFT,TF080,frequency)));
iTF085t = 20*log10(abs(interp1(f_FFT,TF085,frequency)));
iTF090t = 20*log10(abs(interp1(f_FFT,TF090,frequency)));
iTF095t = 20*log10(abs(interp1(f_FFT,TF095,frequency)));
iTF100t = 20*log10(abs(interp1(f_FFT,TF100,frequency)));

% ORGANIZING TOP DATA
D_matrixt   =   [   iTF020t'   iTF030t'   iTF040t'   iTF050t'   iTF060t'   iTF070t'
iTF080t'];
dt          = [ 0.020     0.030     0.040     0.050     0.060     0.070     0.080
];



% IMPORTING FRONT DATA
[f_FFT,...
 TF000, TF005, TF010, TF015, TF020,...
 TF025, TF030, TF035, TF040, TF045,...
 TF050, TF055, TF060, TF065, TF070,...
 TF075, TF080, TF085, TF090, TF095, TF100] = f_import_front_data();

iTF000f = 20*log10(abs(interp1(f_FFT,TF000,frequency)));
iTF005f = 20*log10(abs(interp1(f_FFT,TF005,frequency)));
iTF010f = 20*log10(abs(interp1(f_FFT,TF010,frequency)));
iTF015f = 20*log10(abs(interp1(f_FFT,TF015,frequency)));
iTF020f = 20*log10(abs(interp1(f_FFT,TF020,frequency)));
iTF025f = 20*log10(abs(interp1(f_FFT,TF025,frequency)));
iTF030f = 20*log10(abs(interp1(f_FFT,TF030,frequency)));
iTF035f = 20*log10(abs(interp1(f_FFT,TF035,frequency)));
iTF040f = 20*log10(abs(interp1(f_FFT,TF040,frequency)));
iTF045f = 20*log10(abs(interp1(f_FFT,TF045,frequency)));
iTF050f = 20*log10(abs(interp1(f_FFT,TF050,frequency)));
iTF055f = 20*log10(abs(interp1(f_FFT,TF055,frequency)));
iTF060f = 20*log10(abs(interp1(f_FFT,TF060,frequency)));
iTF065f = 20*log10(abs(interp1(f_FFT,TF065,frequency)));
iTF070f = 20*log10(abs(interp1(f_FFT,TF070,frequency)));
iTF075f = 20*log10(abs(interp1(f_FFT,TF075,frequency)));
iTF080f = 20*log10(abs(interp1(f_FFT,TF080,frequency)));
iTF085f = 20*log10(abs(interp1(f_FFT,TF085,frequency)));
iTF090f = 20*log10(abs(interp1(f_FFT,TF090,frequency)));
iTF095f = 20*log10(abs(interp1(f_FFT,TF095,frequency)));
iTF100f = 20*log10(abs(interp1(f_FFT,TF100,frequency)));

% ORGANIZING FRONT DATA
D_matrixf   =   [   iTF020f'   iTF030f'   iTF040f'   iTF050f'   iTF060f'   iTF070f'
iTF080f'];
```

```
df          = [ 0.020     0.030     0.040     0.050     0.060     0.070     0.080
];

clear TF*

%% Fitting
d0 = 0.02;
f0 = 250e6;

D_matrix = [D_matrixf D_matrixl D_matrixb D_matrixt];
d = [df dl db dt];

[k n m MMSE] = f_MMSE_fit_MOD_INDOOR(D_matrix,d0,d,f0,frequency);
ave = sqrt(MMSE/length(frequency)/length(d));
disp(['k = ' num2str(k)]);
disp(['n = ' num2str(n)]);
disp(['m = ' num2str(m)]);
disp(['sigma = ' num2str(ave)]);
disp(' ');


%% PLOTTING
colors = jet(7);

figure;
hold on;
%_________________________LEFT
plot(frequency, iTF020l,':','LineWidth',3.5,'Color',colors(1,:));
plot(frequency, iTF030l,':','LineWidth',3.5,'Color',colors(2,:));
plot(frequency, iTF040l,':','LineWidth',3.5,'Color',colors(3,:));
plot(frequency, iTF050l,':','LineWidth',3.5,'Color',colors(4,:));
plot(frequency, iTF060l,':','LineWidth',3.5,'Color',colors(5,:));
plot(frequency, iTF070l,':','LineWidth',3.5,'Color',colors(6,:));
plot(frequency, iTF080l,':','LineWidth',3.5,'Color',colors(7,:));
%_________________________BACK
plot(frequency, iTF020b,':','LineWidth',3.5,'Color',colors(1,:));
plot(frequency, iTF030b,':','LineWidth',3.5,'Color',colors(2,:));
plot(frequency, iTF040b,':','LineWidth',3.5,'Color',colors(3,:));
plot(frequency, iTF050b,':','LineWidth',3.5,'Color',colors(4,:));
plot(frequency, iTF060b,':','LineWidth',3.5,'Color',colors(5,:));
plot(frequency, iTF070b,':','LineWidth',3.5,'Color',colors(6,:));
plot(frequency, iTF080b,':','LineWidth',3.5,'Color',colors(7,:));
%_________________________FRONT
plot(frequency, iTF020f,':','LineWidth',3.5,'Color',colors(1,:));
plot(frequency, iTF030f,':','LineWidth',3.5,'Color',colors(2,:));
plot(frequency, iTF040f,':','LineWidth',3.5,'Color',colors(3,:));
plot(frequency, iTF050f,':','LineWidth',3.5,'Color',colors(4,:));
plot(frequency, iTF060f,':','LineWidth',3.5,'Color',colors(5,:));
plot(frequency, iTF070f,':','LineWidth',3.5,'Color',colors(6,:));
plot(frequency, iTF080f,':','LineWidth',3.5,'Color',colors(7,:));
%_________________________TOP
plot(frequency, iTF020t,':','LineWidth',3.5,'Color',colors(1,:));
plot(frequency, iTF030t,':','LineWidth',3.5,'Color',colors(2,:));
plot(frequency, iTF040t,':','LineWidth',3.5,'Color',colors(3,:));
plot(frequency, iTF050t,':','LineWidth',3.5,'Color',colors(4,:));
```

```
plot(frequency, iTF060t,':','LineWidth',3.5,'Color',colors(5,:));
plot(frequency, iTF070t,':','LineWidth',3.5,'Color',colors(6,:));
plot(frequency, iTF080t,':','LineWidth',3.5,'Color',colors(7,:));
hold off;

f = linspace(300e6,3000e6,2000);
hold on;
plot(f,f_estimate(f,0.020,k,n,m,d0,f0),'k','LineWidth',3)
plot(f,f_estimate(f,0.030,k,n,m,d0,f0),'k','LineWidth',3)
plot(f,f_estimate(f,0.040,k,n,m,d0,f0),'k','LineWidth',3)
plot(f,f_estimate(f,0.050,k,n,m,d0,f0),'k','LineWidth',3)
plot(f,f_estimate(f,0.060,k,n,m,d0,f0),'k','LineWidth',3)
plot(f,f_estimate(f,0.070,k,n,m,d0,f0),'k','LineWidth',3)
plot(f,f_estimate(f,0.080,k,n,m,d0,f0),'k','LineWidth',3)
hold off;

set(gca,'XLim',[300e6 3e9]);
set(gca,'YLim',[-90 10]);
title({'Estimated Transfer Function Magnitude vs. Frequency';'Modified Indoor
Propagation Model';...
       'Into Brain from Front, Left, Back and Top'},'FontWeight','bold');
xlabel('Frequency [Hz]');
ylabel('Magnitude [dB]');
grid on;
```

```
% Michael Pecoraro
% November, 2009
%
%   This script plots all the simulated transfer function magnitude data
% vs. frequency and distance in a 3D plot. The Poynting vector simulation
% plots are overlaid on this plot to show the correlation.

clc
clear
close all

% Transparency values - use 0.75 to see it, 0.05 to hide it
Left  = 0.75;
Back  = 0.05;
Top   = 0.05;
Front = 0.05;

frequency = (300e6:50e6:3000e6); % X axis points

%% IMPORTING
% IMPORTING LEFT SIDE DATA
[f_FFT,...
 TF000, TF005, TF010, TF015, TF020,...
 TF025, TF030, TF035, TF040, TF045,...
 TF050, TF055, TF060, TF065, TF070,...
 TF075, TF080, TF085, TF090, TF095, TF100] = f_import_left_data();

iTF000 = 20*log10(abs(interp1(f_FFT,TF000,frequency)));
iTF005 = 20*log10(abs(interp1(f_FFT,TF005,frequency)));
```

```
iTF010 = 20*log10(abs(interp1(f_FFT,TF010,frequency)));
iTF015 = 20*log10(abs(interp1(f_FFT,TF015,frequency)));
iTF020 = 20*log10(abs(interp1(f_FFT,TF020,frequency)));
iTF025 = 20*log10(abs(interp1(f_FFT,TF025,frequency)));
iTF030 = 20*log10(abs(interp1(f_FFT,TF030,frequency)));
iTF035 = 20*log10(abs(interp1(f_FFT,TF035,frequency)));
iTF040 = 20*log10(abs(interp1(f_FFT,TF040,frequency)));
iTF045 = 20*log10(abs(interp1(f_FFT,TF045,frequency)));
iTF050 = 20*log10(abs(interp1(f_FFT,TF050,frequency)));
iTF055 = 20*log10(abs(interp1(f_FFT,TF055,frequency)));
iTF060 = 20*log10(abs(interp1(f_FFT,TF060,frequency)));
iTF065 = 20*log10(abs(interp1(f_FFT,TF065,frequency)));
iTF070 = 20*log10(abs(interp1(f_FFT,TF070,frequency)));
iTF075 = 20*log10(abs(interp1(f_FFT,TF075,frequency)));
iTF080 = 20*log10(abs(interp1(f_FFT,TF080,frequency)));
iTF085 = 20*log10(abs(interp1(f_FFT,TF085,frequency)));
iTF090 = 20*log10(abs(interp1(f_FFT,TF090,frequency)));
iTF095 = 20*log10(abs(interp1(f_FFT,TF095,frequency)));
iTF100 = 20*log10(abs(interp1(f_FFT,TF100,frequency)));

D_matrix1 = [ iTF000' iTF005' iTF010' iTF015' iTF020' iTF025' iTF030' iTF035'
iTF040'  iTF045'  iTF050'  iTF055'  iTF060'  iTF065'  iTF070'  iTF075'  iTF080'
iTF085' iTF090' iTF095' iTF100' ];
d1         = [  0.000   0.005   0.010   0.015   0.020   0.025   0.030   0.035
0.040   0.045   0.050   0.055   0.060   0.065   0.070   0.075   0.080   0.085
0.090   0.095   0.100  ];

% IMPORTING BACK DATA
[f_FFT,...
 TF000, TF005, TF010, TF015, TF020,...
 TF025, TF030, TF035, TF040, TF045,...
 TF050, TF055, TF060, TF065, TF070,...
 TF075, TF080, TF085, TF090, TF095, TF100] = f_import_back_data();

iTF000 = 20*log10(abs(interp1(f_FFT,TF000,frequency)));
iTF005 = 20*log10(abs(interp1(f_FFT,TF005,frequency)));
iTF010 = 20*log10(abs(interp1(f_FFT,TF010,frequency)));
iTF015 = 20*log10(abs(interp1(f_FFT,TF015,frequency)));
iTF020 = 20*log10(abs(interp1(f_FFT,TF020,frequency)));
iTF025 = 20*log10(abs(interp1(f_FFT,TF025,frequency)));
iTF030 = 20*log10(abs(interp1(f_FFT,TF030,frequency)));
iTF035 = 20*log10(abs(interp1(f_FFT,TF035,frequency)));
iTF040 = 20*log10(abs(interp1(f_FFT,TF040,frequency)));
iTF045 = 20*log10(abs(interp1(f_FFT,TF045,frequency)));
iTF050 = 20*log10(abs(interp1(f_FFT,TF050,frequency)));
iTF055 = 20*log10(abs(interp1(f_FFT,TF055,frequency)));
iTF060 = 20*log10(abs(interp1(f_FFT,TF060,frequency)));
iTF065 = 20*log10(abs(interp1(f_FFT,TF065,frequency)));
iTF070 = 20*log10(abs(interp1(f_FFT,TF070,frequency)));
iTF075 = 20*log10(abs(interp1(f_FFT,TF075,frequency)));
iTF080 = 20*log10(abs(interp1(f_FFT,TF080,frequency)));
iTF085 = 20*log10(abs(interp1(f_FFT,TF085,frequency)));
iTF090 = 20*log10(abs(interp1(f_FFT,TF090,frequency)));
iTF095 = 20*log10(abs(interp1(f_FFT,TF095,frequency)));
iTF100 = 20*log10(abs(interp1(f_FFT,TF100,frequency)));
```

```
% ORGANIZING BACK DATA
D_matrix2 = [ iTF000' iTF005' iTF010' iTF015' iTF020' iTF025' iTF030' iTF035'
iTF040'  iTF045'  iTF050'  iTF055'  iTF060'  iTF065'  iTF070'  iTF075'  iTF080'
iTF085' iTF090' iTF095' iTF100' ];
d2         = [  0.000   0.005   0.010   0.015   0.020   0.025   0.030   0.035
0.040   0.045   0.050   0.055   0.060   0.065   0.070   0.075   0.080   0.085
0.090   0.095   0.100  ];

% IMPORTING TOP DATA
[f_FFT,...
 TF000, TF005, TF010, TF015, TF020,...
 TF025, TF030, TF035, TF040, TF045,...
 TF050, TF055, TF060, TF065, TF070,...
 TF075, TF080, TF085, TF090, TF095, TF100] = f_import_top_data();

iTF000 = 20*log10(abs(interp1(f_FFT,TF000,frequency)));
iTF005 = 20*log10(abs(interp1(f_FFT,TF005,frequency)));
iTF010 = 20*log10(abs(interp1(f_FFT,TF010,frequency)));
iTF015 = 20*log10(abs(interp1(f_FFT,TF015,frequency)));
iTF020 = 20*log10(abs(interp1(f_FFT,TF020,frequency)));
iTF025 = 20*log10(abs(interp1(f_FFT,TF025,frequency)));
iTF030 = 20*log10(abs(interp1(f_FFT,TF030,frequency)));
iTF035 = 20*log10(abs(interp1(f_FFT,TF035,frequency)));
iTF040 = 20*log10(abs(interp1(f_FFT,TF040,frequency)));
iTF045 = 20*log10(abs(interp1(f_FFT,TF045,frequency)));
iTF050 = 20*log10(abs(interp1(f_FFT,TF050,frequency)));
iTF055 = 20*log10(abs(interp1(f_FFT,TF055,frequency)));
iTF060 = 20*log10(abs(interp1(f_FFT,TF060,frequency)));
iTF065 = 20*log10(abs(interp1(f_FFT,TF065,frequency)));
iTF070 = 20*log10(abs(interp1(f_FFT,TF070,frequency)));
iTF075 = 20*log10(abs(interp1(f_FFT,TF075,frequency)));
iTF080 = 20*log10(abs(interp1(f_FFT,TF080,frequency)));
iTF085 = 20*log10(abs(interp1(f_FFT,TF085,frequency)));
iTF090 = 20*log10(abs(interp1(f_FFT,TF090,frequency)));
iTF095 = 20*log10(abs(interp1(f_FFT,TF095,frequency)));
iTF100 = 20*log10(abs(interp1(f_FFT,TF100,frequency)));

% ORGANIZING TOP DATA
D_matrix3 = [ iTF000' iTF005' iTF010' iTF015' iTF020' iTF025' iTF030' iTF035'
iTF040'  iTF045'  iTF050'  iTF055'  iTF060'  iTF065'  iTF070'  iTF075'  iTF080'
iTF085' iTF090' iTF095' iTF100' ];
d3         = [  0.000   0.005   0.010   0.015   0.020   0.025   0.030   0.035
0.040   0.045   0.050   0.055   0.060   0.065   0.070   0.075   0.080   0.085
0.090   0.095   0.100  ];

% IMPORTING FRONT DATA
[f_FFT,...
 TF000, TF005, TF010, TF015, TF020,...
 TF025, TF030, TF035, TF040, TF045,...
 TF050, TF055, TF060, TF065, TF070,...
 TF075, TF080, TF085, TF090, TF095, TF100] = f_import_front_data();

iTF000 = 20*log10(abs(interp1(f_FFT,TF000,frequency)));
iTF005 = 20*log10(abs(interp1(f_FFT,TF005,frequency)));
iTF010 = 20*log10(abs(interp1(f_FFT,TF010,frequency)));
iTF015 = 20*log10(abs(interp1(f_FFT,TF015,frequency)));
```

```
iTF020 = 20*log10(abs(interp1(f_FFT,TF020,frequency)));
iTF025 = 20*log10(abs(interp1(f_FFT,TF025,frequency)));
iTF030 = 20*log10(abs(interp1(f_FFT,TF030,frequency)));
iTF035 = 20*log10(abs(interp1(f_FFT,TF035,frequency)));
iTF040 = 20*log10(abs(interp1(f_FFT,TF040,frequency)));
iTF045 = 20*log10(abs(interp1(f_FFT,TF045,frequency)));
iTF050 = 20*log10(abs(interp1(f_FFT,TF050,frequency)));
iTF055 = 20*log10(abs(interp1(f_FFT,TF055,frequency)));
iTF060 = 20*log10(abs(interp1(f_FFT,TF060,frequency)));
iTF065 = 20*log10(abs(interp1(f_FFT,TF065,frequency)));
iTF070 = 20*log10(abs(interp1(f_FFT,TF070,frequency)));
iTF075 = 20*log10(abs(interp1(f_FFT,TF075,frequency)));
iTF080 = 20*log10(abs(interp1(f_FFT,TF080,frequency)));
iTF085 = 20*log10(abs(interp1(f_FFT,TF085,frequency)));
iTF090 = 20*log10(abs(interp1(f_FFT,TF090,frequency)));
iTF095 = 20*log10(abs(interp1(f_FFT,TF095,frequency)));
iTF100 = 20*log10(abs(interp1(f_FFT,TF100,frequency)));

% ORGANIZING FRONT DATA
D_matrix4 = [ iTF000' iTF005' iTF010' iTF015' iTF020' iTF025' iTF030' iTF035'
iTF040'  iTF045'  iTF050'  iTF055'  iTF060'  iTF065'  iTF070'  iTF075'  iTF080'
iTF085' iTF090' iTF095' iTF100' ];
d4         = [  0.000   0.005   0.010   0.015   0.020   0.025   0.030   0.035
0.040   0.045   0.050   0.055   0.060   0.065   0.070   0.075   0.080   0.085
0.090   0.095   0.100  ];

% IMPORTING AND ORGANIZING POWER TYPE DATA
p400       =       importdata('C:\Documents       and       Settings\map2082\My
Documents\Downloads\Head  Data\Head  Data\05  Left  Side  Power\ExH400test.txt','
',2);
d400 = p400.data(:,1); d400 = -(d400-85)/1e3;
p400 = p400.data(:,2); p400 = p400/max(p400);
index = length(find(d400<=0.1));
d400 = d400(end-index+1:end);
p400 = p400(end-index+1:end);

p900       =       importdata('C:\Documents       and       Settings\map2082\My
Documents\Downloads\Head  Data\Head  Data\05  Left  Side  Power\ExH900test.txt','
',2);
d900 = p900.data(:,1); d900 = -(d900-85)/1e3;
p900 = p900.data(:,2); p900 = p900/max(p900);
index = length(find(d900<=0.1));
d900 = d900(end-index+1:end);
p900 = p900(end-index+1:end);

p2400      =       importdata('C:\Documents      and      Settings\map2082\My
Documents\Downloads\Head Data\Head Data\05 Left Side Power\ExH2400test.txt','
',2);
d2400 = p2400.data(:,1); d2400 = -(d2400-85)/1e3;
p2400 = p2400.data(:,2); p2400 = p2400/max(p2400);
index = length(find(d2400<=0.1));
d2400 = d2400(end-index+1:end);
p2400 = p2400(end-index+1:end);

clear TF* iTF*
```

```
%% PLOTTING
[X1 Y1] = meshgrid(d1,frequency);
[X2 Y2] = meshgrid(d2,frequency);
[X3 Y3] = meshgrid(d3,frequency);
[X4 Y4] = meshgrid(d4,frequency);

figure;
hold on;
surf(X1,Y1,D_matrix1,'EdgeColor','k','EdgeAlpha',0.25,'FaceAlpha',Left);
surf(X2,Y2,D_matrix2,'EdgeColor','k','EdgeAlpha',0.25,'FaceAlpha',Back);
surf(X3,Y3,D_matrix3,'EdgeColor','k','EdgeAlpha',0.25,'FaceAlpha',Top);
surf(X4,Y4,D_matrix4,'EdgeColor','k','EdgeAlpha',0.25,'FaceAlpha',Front);
hold off;

hold on;
plot3(d400,      400e6*ones(size(d400)),         10*log10(abs(p400)),      'k--
','LineWidth',1.5*2);
plot3(d900,      900e6*ones(size(d900)),         10*log10(abs(p900)),      'k--
','LineWidth',1.5*2);
plot3(d2400,     2400e6*ones(size(d2400)),     10*log10(abs(p2400)),      'k--
','LineWidth',1.5*2);
hold off;

% MANIPULATING / ANNOTATING GRAPH
c=colormap('jet');
c=flipud(c);
colormap(c);
colorbar;
set(gca,'XDir','reverse');
set(gca,'YDir','reverse');
set(gca,'View',[-35 25]);
set(gca,'XLim',[0.00  0.10  ]);
set(gca,'YLim',[000e6 3000e6]);
grid on;



title({'Transfer Function Magnitude vs. Distance and Frequency';'Power Plots
vs. E-Field Plots';...
    'Into Brain from Left'},'FontWeight','bold','FontSize',16);
xlabel('Distance [m]','FontSize',16);
ylabel('Frequency [Hz]','FontSize',16);
zlabel('Magnitude [dB]','FontSize',16);
grid on;
set(gca,'View',[-46 15]);
set(gcf,'Position',[100 100 800 550]);
set(gcf,'Color',[1 1 1]);
```

```
% Michael Pecoraro
% December, 2009
%
%   This program uses the k n and m values as generated from the final MMSE
% estimation for all the data using the Modified Indoor Propagation Model
% fit to then estimate, for specific values of distance, what the transfer
```

```
% function would look like.

clc
clear
close all

frequency = (300e6:1e6:3000e6); % X axis points

d0 = 0.02;
f0 = 250e6;

k = -2.664869159255716;
n = +0.433320057976118;
m = +0.839099574010191;

d = 0.02:0.0005:0.20;
f1 = 400e6;

%% PLOTTING
figure;

plot(d*100,f_estimate(f1,d,k,n,m,d0,f0),'k','LineWidth',4);

set(gca,'XLim',[2 20]);
set(gca,'XTick',2:20);
set(gcf,'Position',[100 100 800 400]);
% set(gca,'YLim',[-50 0]);
title({'Estimated Transfer Function Magnitude vs. Distance, @ 400MHz';...
       'Predictions         for         Distance         and         Rotation
Simulations'},'FontWeight','bold','FontSize',12);
xlabel('Distance [cm]','FontSize',12);
ylabel('Magnitude [dB]','FontSize',12);
grid on;
legend('Prediction: 400MHz');
set(gca,'FontSize',12);
set(gcf,'Color',[1 1 1]);
```